Phase-Field Modeling of Liquids Splitting Between Separating Surfaces and its Application to High-Resolution Roll-Based Printing Technologies

by

Fahri Erinc HIZIR

B.S. Mechanical Engineering, Middle East Technical University, 2008
M.S. Mechanical Engineering, Pennsylvania State University, 2010
M.S. Mechanical Engineering, Massachusetts Institute of Technology, 2013

Submitted to the Department of Mechanical Engineering
in partial fulfillment of the requirements for the degree of

Doctor of Philosophy in Mechanical Engineering

at the

MASSACHUSETTS INSTITUTE OF TECHNOLOGY

June 2016

Signature of Author: Signature redacted

Department of Mechanical Engineering
May 24, 2016

Certified by: Signature redacted

David E. Hardt
Ralph E. and Eloise F. Cross Professor of Mechanical Engineering
Thesis Supervisor

Accepted by: Signature redacted

Rohan Abeyaratne
Chairman, Committee for Graduate Students

To *Lale Alev Bingöl*

Phase-Field Modeling of Liquids Splitting Between Separating Surfaces and its Application to High-Resolution Roll-Based Printing Technologies

By
Fahri Erinc HIZIR

Submitted to the Department of Mechanical Engineering
on May 24, 2016 in Partial Fulfillment of the Requirements for
the Degree of Doctor of Philosophy in
Mechanical Engineering

Abstract

In roll-based printing systems, controlled release of liquid ink to the substrate surface is achieved through the transport of the liquid ink through a series of ink transfer rollers in the form of splitting liquid bridges. An in-depth understanding of the liquid transport process through the ink transfer rollers is essential for advancing the roll-based printing technology and achieving the highest quality printing. In this study, the phase-field method is investigated to characterize the liquid bridges in roll-based printing systems.

Phase-field models of two-phase flow systems are being used increasingly often in a variety of applications ranging from microfluidics to turbulent flows. However, there are limited implementations of the phase-field method to simulate the liquid ink transport in roll-based printing systems. There are advantages of the phase-field method over other methods that are generally used for simulating the liquid transport in roll-based printing systems such as the volume of fluid method and the moving mesh methods. This study demonstrates that the phase-field method is an effective tool to simulate the liquid ink transport in roll-based printing systems that facilitates the treatment of certain characteristics of the ink flows such as moving and deforming interfaces, topology changes, and slipping contact lines.

In the phase-field simulations described in this study, the liquid ink transport between the rollers is approximated as the stretching and splitting of liquid bridges with pinned or moving contact lines between vertically separating surfaces. The interface separating the liquid and the surrounding air is represented as a diffuse interface with finite thickness across which the two phases mix. First, the simulation conditions that yield accurate results are determined by examining the effect of the phase-field parameters and the mesh characteristics on the simulation results. The simulation results show that a sharp interface limit is approached when the capillary width is decreased keeping the mobility proportional to the capillary width

squared. This limit best represents real interfaces having molecular thickness in the micron-scale flows investigated. Close to the sharp interface limit, the mobility changes over a specified range are observed to have no significant influence on the simulation results. The computational mesh is segmented into regions of varying mesh fineness or adaptive mesh refinement is implemented to reduce the computational cost of resolving thin interfaces in the simulations. The simulation results are validated against data reported in existing studies of liquid ink transport in roll-based printing systems for selected capillary width and mobility values.

Next, the liquid ink transport from the axisymmetric cells on the surface an ink-metering roller to the surface of stamp features is simulated. The function of the cells on an ink-metering roller is to control the amount of liquid ink delivered to the stamp surface. The resolution of printing is limited by the width of the cell openings, since uniform inking of the stamp requires the width of the cell openings to be smaller than the size of the stamp features. The cell geometries explored in the simulations are selected to enable printing with higher resolution than the current industry standards. Increasing the resolution of printing would improve the performance of printed products and expand their range of functionality.

The results of the simulations indicate that under negligible inertial effects and in the absence of gravity, the amount of liquid ink transferred from a cell with low surface wettability to a stamp with high surface wettability increases as the cell sidewall steepness and the cell surface wettability decrease, and the stamp surface wettability and the capillary number increase. The amount of liquid ink removed from the cell does not change significantly as the cell depth increases above a certain value. High-resolution printing strategies, which indicate how the printing parameters should be manipulated to more precisely control the printed layer thickness, to eliminate printing defects, and to minimize cell clogging, are derived by analyzing the simulation results. The cells with different sidewall inclination angles are used to represent the cells with irregular surface topography on novel materials and novel roller designs that could be used for stamp inking during high-resolution roll-based printing, such as the pores on porous materials and the cells fabricated with poor control over cell geometry due to manufacturing difficulties at small length scales. The variations in the printed layer thickness with the cell sidewall inclination angle is found to be significant (~10-100 nm for cells with 2-μm opening width) indicating that the variations in cell geometry should be minimized when designing advanced rollers for use in high-resolution roll-based printing.

Thesis Supervisor: David E. Hardt
Title: Ralph E. and Eloise F. Cross Professor of Mechanical Engineering

Table of Contents

List of Figures

List of Tables

Chapter 1. Introduction

1.1. Motivation, Objectives, and Scope of the Thesis

Roll-based printing systems are used for cost-effective manufacturing of printed products and functional surfaces in large volumes and over continuous webs. Electronic circuits, RFID tags, organic light-emitting diodes, photovoltaics, thin-film batteries and sensors are amongst the examples of products that have been manufactured using roll-based printing systems.

In roll-based printing systems, controlled release of liquid ink to the substrate surface is achieved through the transport of the liquid ink through a series of ink transfer rollers in the form of splitting liquid bridges. An in-depth understanding of the liquid transport process through the ink transfer rollers is needed to advance the roll-based printing technology and achieve the highest quality printing. In this study, the phase-field method is investigated to characterize the liquid bridges in roll-based printing systems.

Phase-field models of two-phase flow systems are gaining popularity in a variety of applications ranging from microfluidics to turbulent flows. However, there are limited implementations of the phase-field method to simulate the liquid transport in roll-based printing systems. This study demonstrates that phase-field modeling is an effective tool to investigate the liquid transport in roll-based printing systems that facilitates the treatment of the relevant characteristics of the ink flows such as moving and deforming interfaces, topology changes, slipping contact lines and complex rheology.

There are advantages of phase-field modeling over other methods that are generally used for simulating the liquid transport in roll-based printing systems such as the volume of fluid method and the moving mesh methods. Phase-field models are physically motivated, consistent with thermodynamics, and they contain the effects of short-range molecular forces that are involved in topology changes. In addition, phase-field models enable contact line slip to take place naturally, as a result of diffusive interfacial fluxes. Hence, a realistic description of the ink flows is obtained through phase-field modeling. Furthermore, the rheology of the ink flow and the microstructure in the ink are linked through the free energy, which provides flexibility in simulating new ink formulations. Being a fixed mesh method, the phase-field method eliminates issues due to deformation and entanglement of the mesh elements during the stretching and splitting of liquid bridges.

The objectives of this study are

- to implement the phase-field method to simulate the splitting of liquids with moving contact lines between separating roller surfaces;

- to determine simulation conditions and simulation parameters that yield accurate results in phase-field simulations of two-phase flows;
- to determine guidelines on cell design and selection of printing conditions to improve micron-scale roll-based printing;
- to obtain insights on the applicability of new materials and new roller designs that have cells with irregular surface topography to stamp inking in high-resolution roll-based printing.

The scope of this thesis consists of an in-depth study conducted to investigate the effect of the cell specifications and the printing conditions on the ink release characteristics of axisymmetric cells having 2-μm openings. The cell geometries studied would enable reaching higher printing resolutions than the current industry standards, i.e. ≈20 μm for flexographic and gravure printing. The results of the simulations confirm and broaden the results of the existing studies, and a set of printing guidelines that would improve the quality and resolution of roll-based printing are derived by analyzing them. Implementation of these printing guidelines during high-resolution roll-based printing would lead to an enhancement in the performance of the printed products, and an expansion in their range of functionality. For instance, improving the resolution of roll-based printing would enable printing of smaller thin film transistor that could be used to manufacture displays with higher image quality; and metamaterials that better control wave propagation (e.g. manufacturing of photonic crystals that enable light extraction enhancement from organic light-emitting diodes and broadband light capturing in photovoltaic cells). Better understanding the ink release characteristics of the cells would enable more precisely controlling the thickness of the printed layers, and elimination of printing defects (e.g. bridging of printed patterns due to excessive ink transfer to the stamp, and void areas in the printed regions resulting from insufficient ink transfer to the stamp). More precisely controlling the print thickness would enable manufacturing of solar cells that have higher performance. Elimination of the printing defects would enable manufacturing of circuits that are free of short and broken circuits, and manufacturing of printed circuit boards having conductive lines with smaller trace widths leading to more compact electronic devices.

The simulations' emphasis is on the evacuation of cells having different sidewall inclination angles. Understanding how the cell sidewall inclination angle affects the evacuation of the cells is important due to two reasons. First, the cell sidewall inclination angle is a cell design parameter that could be used to control the amount of the liquid ink removed from a cell and the printed layer thickness. Second, improving the resolution of printing would require reducing the size of the cells used for stamp inking. However, as the cell size is reduced, it gets more difficult to manufacture the same cell geometry on a roller surface consistently. Hence, there may be variations in the geometry of the cells manufactured at small size scales. In addition, the cells on new material alternatives that could be used for high-resolution printing, such as the pores on porous materials, could have irregular

surface topography. The cells with variable sidewall inclination angle that are used in the simulations represent such cells with uncontrolled and irregular surface topography. The effect of cell sidewall inclination angle on the ink release characteristics of axisymmetric cells has not been investigated in the existing studies. A better understanding of this effect is formed through the simulations presented in this thesis.

This study aims to open a path for future phase-field simulations that would enable establishment of improved ink-metering roller designs and advancement of the roll-based printing technology.

1.2. Thesis Outline

In Chapter 2, concepts used for characterizing liquid flows are described, and liquid transport in roll-based printing systems is reviewed.

In Chapter 3, the phase-field method is described, including its history, theory, advantages, challenges, and applications.

In Chapter 4, phase-field simulations of liquid splitting between separating flat plates are described. The effects of the mesh characteristics, and the thickness and the mobility of the interface on the simulation results are investigated. The simulation results are validated against the numerical solution presented in the literature.

In Chapter 5, the phase-field method is implemented to simulate the emptying of the cells on the surface of the ink transfer rollers. The effect of cell sidewall inclination angle, cell depth, cell surface wettability, stamp surface wettability, printing speed, and ink properties on the quantity of liquid ink removed from the cells is investigated. Based on the simulations, guidelines for improving the quality of micron-scale roll-based printing are presented.

In Chapter 6, the future work to extend the research on roll-based printing presented in this thesis is described.

In Chapter 7, this study, and its contributions to the fields of phase-field modeling and roll-based printing, are summarized.

Chapter 2. Overview of Liquid Transfer in Roll-Based Printing Systems

Achieving the highest quality in roll-based printing requires understanding the factors that affect how liquids behave and the conditions of the liquid ink transport at different stages of printing. This introductory chapter gives background information needed to analyze liquid transport in two widely used types of roll-based printing systems, flexography and gravure.

2.1. Basic Concepts

2.1.1. Surface Tension

Considering two phases separated by an interface, from a microscopic view, the molecules inside the bulk of the two fluids would be in a different state than the molecules located at the interface (Figure 2.1a). The attractive forces applied on an interior molecule by the surrounding molecules would balance each other because of symmetry. But the attractive forces acting on the interface molecules are not symmetric, since the interface molecules are pulled towards the two fluids with different strengths. Hence, the interface molecules would move in the direction of the net attractive force, until they reach equilibrium and the interface surface area is minimized. The pulling force acting on the interface molecules is termed surface tension (or coefficient of surface tension), σ. It is responsible for familiar daily phenomena such as beading of water drops on the leaves of plants and the supporting of a small object of larger density (such as a steel sewing needle) on the surface of water [1].

From a thermodynamic point of view, σ can be defined as

$$\sigma_{12} = \left(\frac{\partial G}{\partial A}\right)_{T,p=constant} \tag{1}$$

where G is the Gibbs free energy of the entire system (including the two phases and the interface) and A is the area of the interface. Thus surface tension is a measure of the additional energy associated with the interface, which results from the higher energy state of the interface molecules [2]. Surface tensions for several interfaces are listed in Table 2.1.

A curved interface indicates a pressure difference across the interface with pressure being higher on the concave side. For a curved interface at equilibrium, using relations indicating equilibrium of stresses at the interface, Young-Laplace equation giving the pressure drop across the interface can be derived as

$$p_1 - p_2 = \sigma_{12}\left(\frac{1}{R_1} + \frac{1}{R_2}\right) \tag{2}$$

where R_1 and R_2 are the radii of curvature of any point on the curved surface in two orthogonal directions (Figure 2.1b).

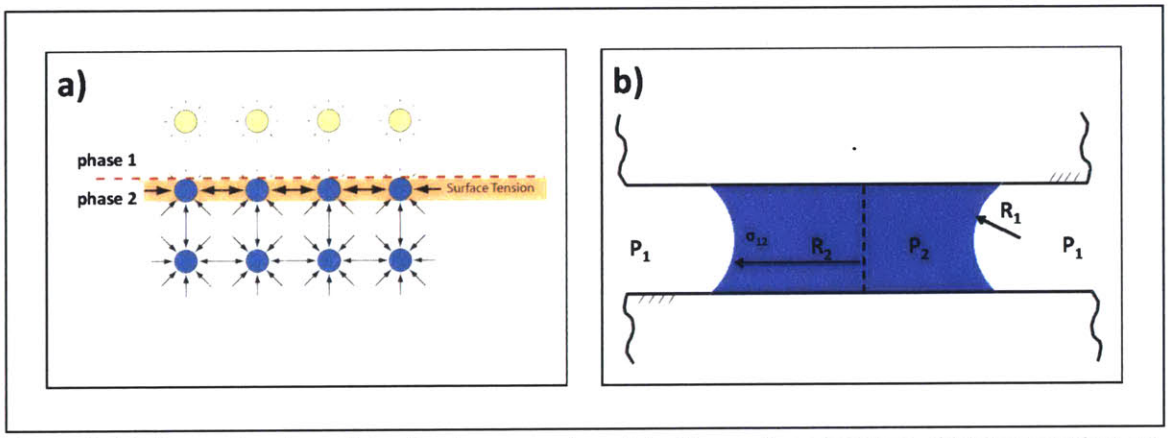

Figure 2.1 Schematics describing basic concepts related to surface tension. a) Forces acting on the molecules at the interface between two phases and on those in the bulk of the two phases. b) Schematic of a stationary liquid bridge between two flat surfaces representing a curved interface between two phases.

Mercury-air	484 mN/m
Water-air	73 mN/m
Ethanol-air	23 mN/m

Table 2.1 Surface tension coefficients for some liquids with air at 20°C [2].

2.1.2. Contact Angle and Work of Adhesion

For a liquid drop on a solid surface surrounded by a gas, the contact angle is the angle the interface makes with the solid surface at equilibrium, as measured through the dense medium. The equilibrium of forces acting at the triple point of a drop leads to Young's equation, which gives the contact angle (θ) of the drop as

$$\cos(\theta) = \frac{\sigma_{SG} - \sigma_{SL}}{\sigma_{LG}} \tag{3}$$

where σ_{SG}, σ_{SL} and σ_{LG} are the surface tensions between solid-gas, solid-liquid and liquid-gas, respectively (Figure 2.2).

Young-Dupre equation [3] gives the work of adhesion (W_a) between a solid surface and a liquid drop in terms of the equilibrium contact angle as

$$W_a = \sigma_{LG}[1 + \cos(\theta)] \tag{4}$$

A reduction in θ ($0 \leq \theta \leq \pi$) leads to a higher work of adhesion indicating that a liquid adheres more strongly to a surface with high surface energy, which it likes to wet.

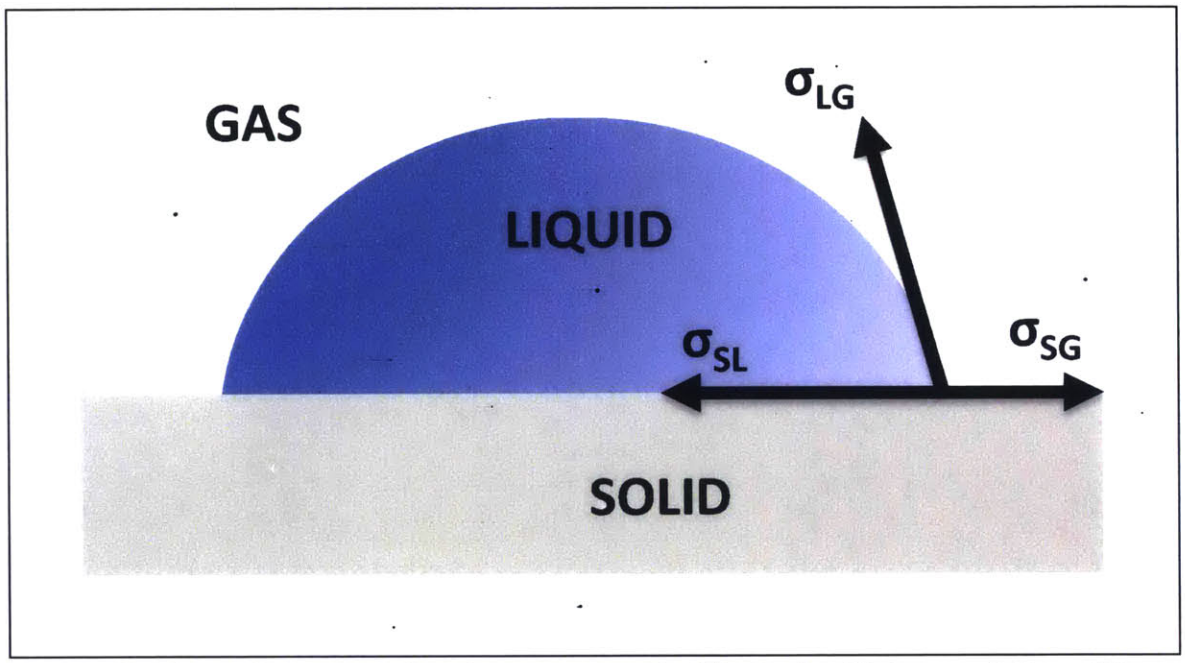

Figure 2.2 Schematic representing the contact angle (θ) of a liquid drop and the solid-gas (σ_{SG}), solid-liquid (σ_{SL}) and liquid-gas (σ_{LG}) surface tensions acting at the triple point.

2.1.3. Similarity and Non-Dimensional Parameters

In a general flow field, complete similarity between a model and prototype is achieved only when there is geometric, kinematic and dynamic similarity. Geometric similarity states that the model has the same shape as the prototype, but it is scaled. Kinematic similarity states that the velocity at any point in the model flow is proportional to the velocity at the corresponding point in the prototype flow. Dynamic similarity is achieved, when all forces in the model flow scale by a constant factor to corresponding forces in the prototype flow [1].

Complete similarity is also ensured, when the model and prototype are geometrically similar, and all independent non-dimensional parameters (π groups) match between the model and the prototype. Under these conditions, it is guaranteed that the dependent π group of the model is equal to the dependent π group of the prototype.

As an application to roll-based printing, liquid transport from a smooth roller to a smooth roller or from a smooth roller to a patterned roller can be described by 7 parameters: fraction of ink transferred from one roller to the other (Φ), roller velocity (V), liquid ink density (ρ), liquid ink dynamic viscosity (μ), surface tension coefficient (σ), length scale for the liquid drop being transported (L) and gravitational acceleration (g). Here, Φ is the independent variable and it can be expressed in terms of the dependent variables as

$$\Phi = f(\rho, \mu, \sigma, V, R, g) \quad (5)$$

The Buckingham Pi theorem [4] indicates that using 3 primary dimensions (time, length and mass) and 7 parameters, 7-3=4 primary groups can be constructed each having 3 repeating parameters. Selecting V, R and μ as the repeating parameters, combining them with the remaining parameters and forcing their product to be dimensionless, the π groups can be obtained as

$$\pi_1 = \Phi^1.\mu^0.V^0.L^0 \quad (6)$$
$$\pi_2 = \sigma^{-1}.\mu^1.V^1.L^0 \quad (7)$$
$$\pi_3 = \rho^1.\mu^{-1}.V^1.L^1 \quad (8)$$
$$\pi_4 = g^{-1}.\mu^0.V^2.L^{-1} \quad (9)$$

Here,

$$\pi_1 = \phi \quad (10)$$

$$\pi_2 = Ca = Capillary\ number = \frac{viscous\ forces}{surface\ tension\ forces} = \frac{\mu V}{\sigma} \quad (11)$$

$$\pi_3 = Re = Reynolds\ number = \frac{inertial\ forces}{viscous\ forces} = \frac{\rho V L}{\mu} \quad (12)$$

$$\pi_4 = Fr = Froude\ number = \frac{inertial\ forces}{gravity\ forces} = \frac{V^2}{gL} \quad (13)$$

Expressing the dependent π group in terms of the independent π groups, the following relation can be obtained

$$\Phi = f(Re, Fr, Ca) \quad (14)$$

Two different printing cases are completely similar, if all of their independent π groups are equal,

$$Re_1 = Re_2 \quad (15)$$

$$Fr_1 = Fr_2 \quad (16)$$

$$Ca_1 = Ca_2 \quad (17)$$

This guarantees the equality of the dependent π group,

$$\Phi_1 = \Phi_2 \quad (18)$$

Forces affecting the liquid transport in a roll-based printing system are surface tension forces, viscous forces, inertial forces and gravitational forces. Other dimensionless parameters representing the relative magnitudes of these forces can be formed such as

$$St = Stokes\ number = \frac{gravity\ forces}{viscous\ forces} = \frac{\rho g L^2}{\mu U} \quad (19)$$

$$Bo = Bond\ number = \frac{gravity\ forces}{surface\ tension\ forces} = \frac{\rho g L^2}{\sigma} \quad (20)$$

$$We = Weber\ number = \frac{inertial\ forces}{surface\ tension\ forces} = \frac{\rho L V^2}{\sigma} \quad (21)$$

For Re<1, Fr>1 and Ca<1, the relative magnitudes of the forces affecting the liquid transport are: gravitational forces < inertial forces < viscous forces < capillary forces. Reducing the length scale of liquid transfer would lead to a reduction in Re and an increase in Fr in equation (14). In terms of the relative magnitudes of the forces affecting the liquid transport, this would lead to a decrease in the magnitude of the gravitational and inertial forces, compared to the magnitude of the viscous and capillary forces. When the length scale is sufficiently small, the effect of gravitational and inertial forces on the liquid transfer would be negligible compared to the effect of viscous and capillary forces. This would cause Φ to be a function of Ca only, and make it independent of the length scale.

2.2. Liquid Transport in Roll-Based Printing Systems

2.2.1. Roll-Based Printing Systems: Flexography and Gravure

Flexography and gravure are roll-based mass printing processes used in the manufacture of printed products in large volumes and over continuous webs [5-7]. Examples of products printed using these techniques include organic light-emitting diodes, radio frequency identification tags, solar cells, sensors and batteries. Both printing techniques use a cylinder with cells on its surface (the engraved roller, also known as anilox roller in flexography) for ink transfer to the substrate from an ink supply (Figure 2.3). Subsequent steps of the flexographic printing process (Figure 2.3b) are:

1) Inking of the engraved roller
2) Blading of the engraved roller to meter an exact volume of ink into the roll cells
3) Ink transfer from the engraved roller to a patterned elastomer stamp surface
4) Ink transfer to the substrate surface

In gravure printing, the third step is excluded and ink is transferred directly from the engraved roller to the substrate without using a rubber stamp (Figure 2.3a). Hence, the pattern of cells on the engraved roller determines the shape of the layer printed on the substrate, instead of the rubber stamp [5]. In both printing techniques, the ink may pass through additional intermediate rollers for further processing before being transported to the substrate surface.

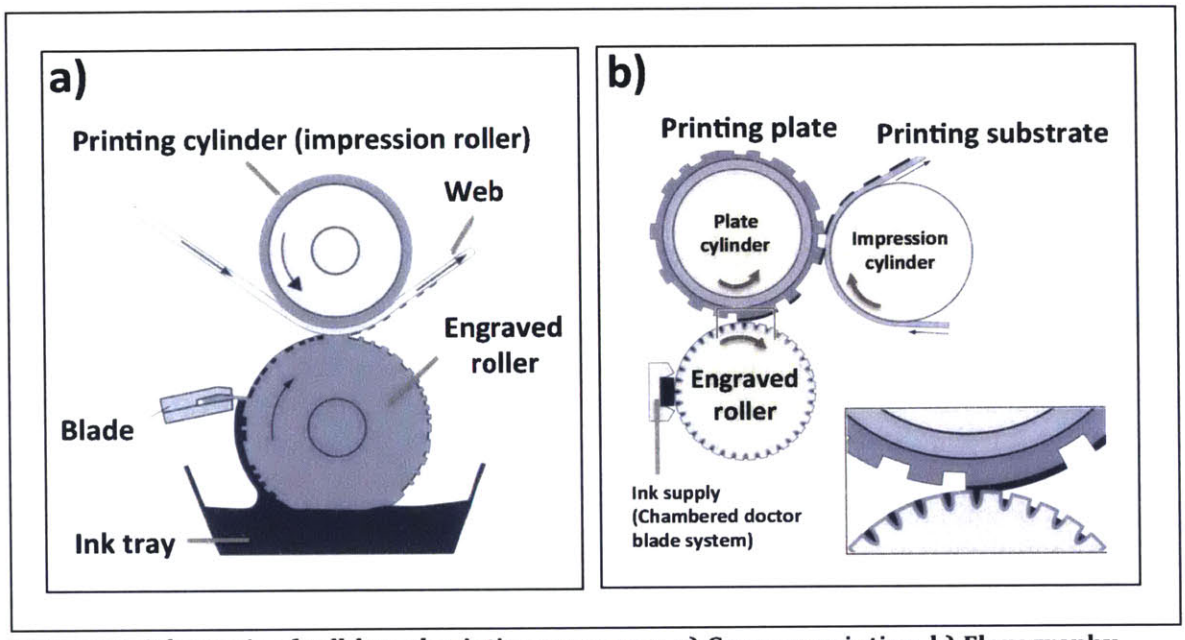

Figure 2.3 Schematic of roll-based printing processes. a) Gravure printing. b) Flexography.

Operation speeds (web speeds) of these printing techniques are on the order of 1 to 10 m/s. Thickness of printed layers prior to drying are on the order of 0.1 to 100 μm. For traditional applications, smallest size of printed features is approximately 20 μm to 100 μm [5, 6, 8, 9]. Printing with resolution below 10 μm has been demonstrated using novel engraved roller designs [10-12].

2.2.2. Liquid Transport Between Roller Surfaces

In roll-based printing systems, liquid ink is transported from one roller to the other in the form liquid bridges. As two neighboring rollers rotate, bridge contact lines on the two roller surfaces move away from each other. This leads to slipping of the contact lines, stretching of the bridge and eventually splitting of it into two. As a result of the splitting, a fraction of the liquid held by one roller is transported to the other one.

A common simplification while investigating the liquid transport in roll-based printing is to treat the roller surfaces as flat plates [13-26]. The "host plate" remains stationary and the "target plate" is in vertical, horizontal or rotational motion. Both plate surfaces may be smooth representing the liquid transport between two smooth roller surfaces or one plate may contain a cell representing the liquid flow out of cells on the engraved roller (Figure 2.4).

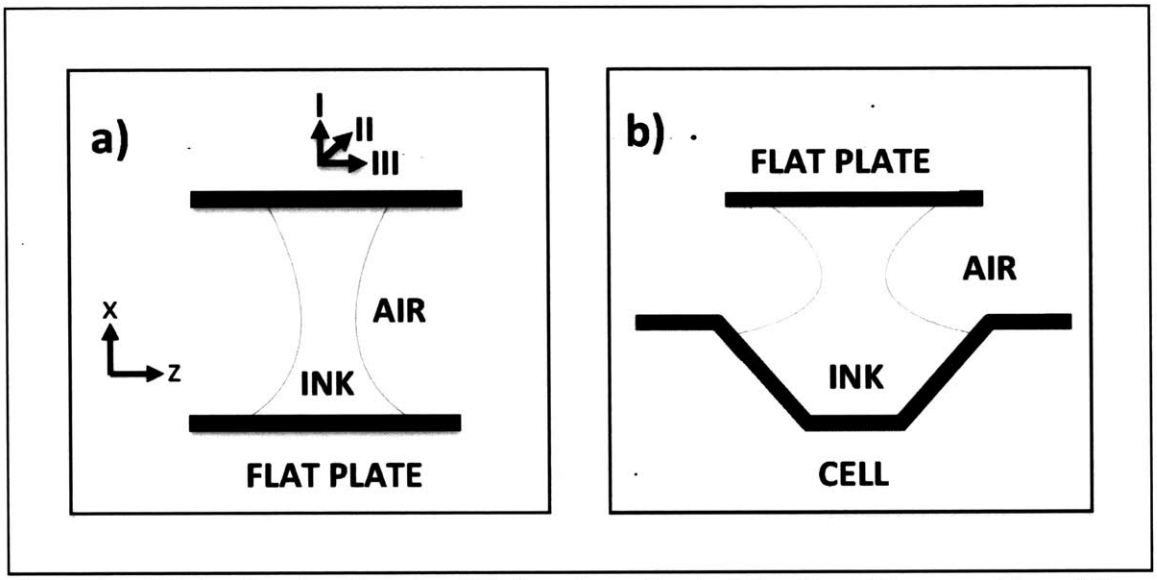

Figure 2.4 Schematics showing simplified systems for studying liquid transport in roll-based printing. a) Liquid bridge between two flat plates. b) Liquid bridge between a cell and a flat plate. The flat plate represents the surface of a smooth roller and the cell represents a single liquid-filled cell on the surface of an engraved roller. I represents extensional motion, II represents shear motion and III represents rotational motion of the separating surfaces.

The review article by Kumar indicates the ranges of printing parameters used in roll-based printing [9]: For roller surfaces represented as flat plates in extensional motion, typical separation velocities are on the order of 0.01 to 0.1 m/s. The range for liquid ink viscosities is on the order of 0.001 to 1 Pa.sec and the approximate range for interfacial tension is 0.02 N/m to 0.07 N/m. For an ink density of 1000 kg/m^3 and taking typical length scales for printed features to be on the order of 10μm to 100μm, dimensionless numbers characterizing the liquid ink transport process are in the range: $10^{-4} < Ca < 1$, $10^{-4} < Re < 10$, $10^{-5} < St < 10$.

2.2.3. Importance of Studying Liquid Transport in Roll-Based Printing

Understanding and controlling liquid transport in roll-based printing systems is essential for achieving the highest the quality printing and advancing the roll-based printing technologies. Taking flexography as an example, better understanding liquid transport from the stamp to the substrate would enable more precisely controlling the thickness of the patterns printed on the substrate. Precise control of thickness is crucial in printing of solar cells and batteries, which exhibit maximum performance for certain thickness ranges of their component layers. Investigating liquid transport from the stamp to the substrate would also make it possible to determine printing conditions required for elimination of printing defects such as dot gain and ink smearing or dirty prints resulting from satellite drops landing on the substrate surface. The printing strategies obtained would enable printing of electronic devices, which work flawlessly without broken or short circuits.

As a second example, improving the resolution of flexography requires the use of cells with smaller opening widths on the engraved roller. The reason for this is that

the size of stamp features need to be about three to four times larger than the opening width of the cells on the engraved roller for homogenous inking of the stamp features (Figure 2.5). This ensures that the ink is applied only on the tops of the stamp features and minimal dot gain is obtained [5, 27]. However, smaller-sized cells can lead to printing defects resulting from cell clogging. A better understanding of liquid transport out of smaller-sized cells is needed for the design of cells that show minimal clogging and that release the desired amount of ink enabling high-resolution printing of electrodes having higher capacitance, sensors having higher sensitivity and transistors with higher performance resulting from higher transition frequencies.

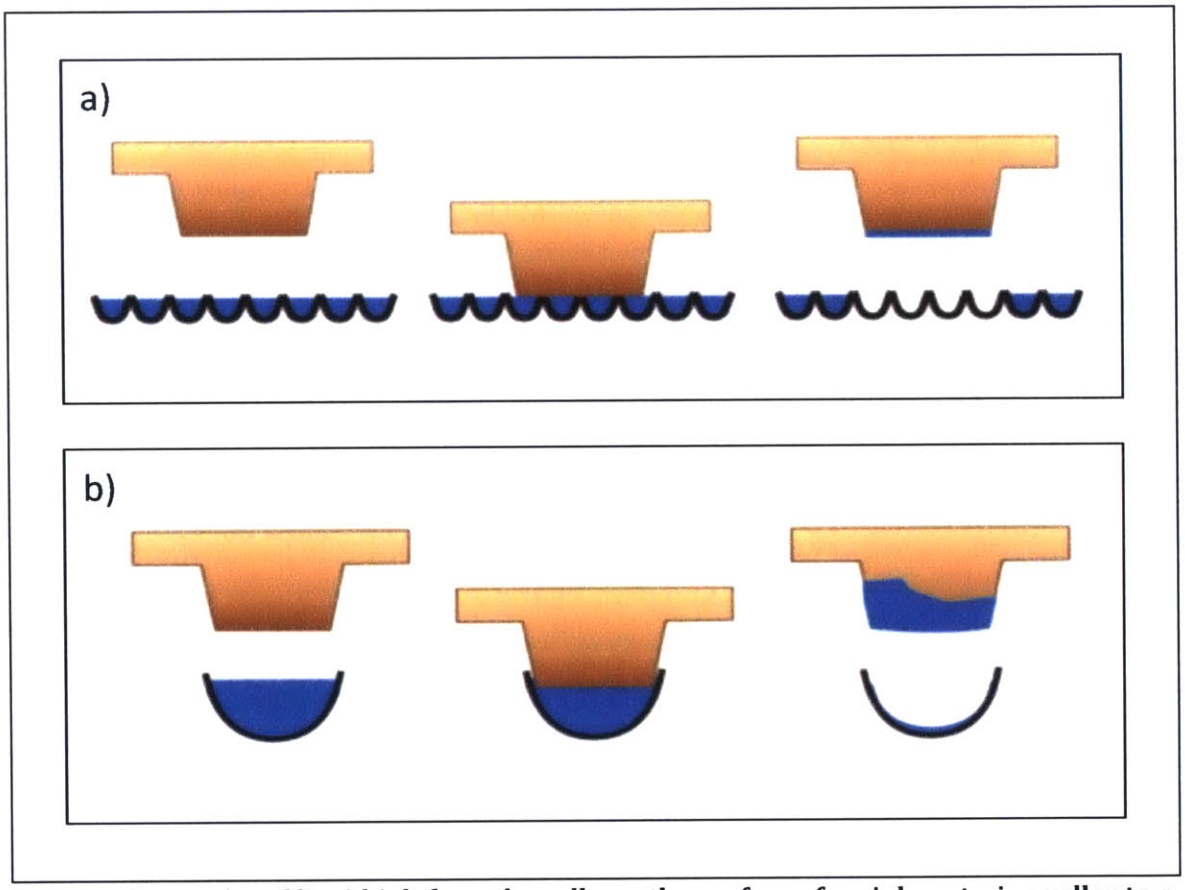

Figure 2.5 Transfer of liquid ink from the cells on the surface of an ink-metering roller to a stamp feature. a) The stamp feature is inked uniformly, since the opening widths of the cells are about three times smaller than the width of the stamp feature. b) The stamp feature dips into the cell and it is inked non-uniformly, since the opening width of the cell is larger than the width of the stamp feature (adapted from [29]).

Numerical modeling is a useful tool for studying liquid transport in roll-based printing systems, as it provides very detailed information, which may be costly, challenging or sometimes impossible to obtain through experiments. As an example, high roller speeds and small cell sizes make it difficult to visualize the cell evacuation process in an operating printing system. Hence, ex-situ experiments need to be performed using scaled-up cells under conditions imitating actual

printing conditions [28]. Numerical models can effectively describe liquid behavior in a simulation setting, which corresponds to real printing conditions involving small length and time scales.

The effect of major printing parameters on the liquid transport in roll-based printing systems has been examined through numerical models. The findings of these studies are summarized below.

- Dodds *et. al.* simulated the stretching of axisymmetric Newtonian liquid bridges with moving contact lines between two surfaces that vertically separated using a moving mesh to track the free surface [14]. In the simulations, inertial and gravitational effects were absent. The effect of the contact angles, the capillary number and the cell geometry on the liquid transfer process was investigated. For liquid stretching between two flat plates, the fraction of liquid transferred to the target plate increased, as the contact angle on the target plate decreased relative to that on the host plate. When the capillary number increased, the fraction of liquid transferred to the target plate increased if the host plate was more wettable than the target plate, but the opposite effect was observed if the host plate was less wettable than the target plate. When the contact lines on the target plate were pinned, an increase in capillary number increased the fraction of liquid transferred to the target plate, if the host plate had high wettability. For liquid stretching between a cell and a flat plate, the fraction of liquid removed from the cell increased, as the cell aspect ratio (width/depth) increased, the contact angle on the plate surface decreased, the contact angle on the cell surface increased and the capillary number increased. Since the liquid transfer process in a flexographic printer can be approximated as the stretching and splitting of an axisymmetric liquid bridge, the findings of this study are important for better understanding the liquid transport in roll-based printing systems. In Chapter 4, the results of phase-field simulations on the splitting of axisymmetric liquid bridges between separating flat plates are validated against the numerical solution presented by Dodds *et. al.* [14].

- Huang *et. al.* simulated the stretching and splitting of two-dimensional symmetric liquid bridges with moving contact lines between two surfaces that vertically separated using the volume of fluid method [15]. Inertial effects were small, and gravitational effects were small or absent in the simulations. For the splitting of a Newtonian liquid between two flat plates, the dependence of the fraction of liquid transferred to the target plate on the contact angles and the capillary number was in agreement in with the results of Dodds *et. al.* [14]. The breakup of the liquid was faster, when a shear-thinning liquid was used in the simulations. For the splitting of a Newtonian liquid between a cell and a flat plate, the amount of liquid transferred to the flat plate increased, as the cell sidewalls got steeper, but it did not change as the cell depth increased. Since the liquid transfer in a gravure printer can be approximated as the stretching and splitting of a two-dimensional symmetric liquid bridge, the findings of this study are important for better

understanding the liquid transport in roll-based printing systems. In Appendix C, the results of phase-field simulations on the splitting of two-dimensional symmetric liquid bridges between separating flat plates are validated against the numerical solution presented by Huang *et. al.* [15].

- Hoda and Kumar simulated the stretching of a liquid bridge between a stationary cell and a horizontally moving flat plate using the boundary integral technique [17]. The liquid bridge had one meniscus that was fixed to the flat plate at one end and that was free to move on the cell surface at the other end. The inertial and gravitational effects were neglected in the simulations. The fraction of liquid removed from the cells decreased, as the cell depth and the capillary number increased. For a liquid bridge having two free surfaces that were pinned on the flat plate and free to move on the cell surface, the rotational motion of the flat plate increased the fraction of the liquid removed from the cell. These results are in agreement with the findings of Powell *et. al.* who used a similar model to study the liquid behavior between a two-dimensional cell and a horizontally moving flat plate [20]. Powell *et. al.* further report the existence of recirculation regions inside the cells which become more squashed and asymmetric, as the liquid bridge gets closer to splitting.

- Dodds *et. al.* investigated the effect of inertia on the stretching of axisymmetric Newtonian liquid bridges with moving contact lines between a moving flat plate and either a stationary flat plate or a cell [23]. For the case of two flat plates, increasing inertial forces shifted the breakup point towards the more wettable surface, and hence reduced the fraction of liquid that remains on the more wettable surface after splitting. For the case of a stationary cell and a moving flat plate, increasing Reynolds number shifted the breakup point towards the cell, and hence increased the fraction of liquid transferred to the flat plate. However, as the flat plate was made more wettable, a second pinch-off point could form near the flat plate, which could lead to the formation of a satellite drop and the reduction of the fraction of liquid transferred to the plate.

- Ghadiri *et. al.* studied the two-dimensional symmetric bridges of a shear-thinning liquid that stretched and split between a stationary cell and a vertically moving flat plate [16]. Specifically, they studied the influence of the cell shape and the specifications of the separating surfaces on the liquid transfer. The Reynolds number characterizing the liquid flow was small and gravity was not present in their simulations. For a cell having a fixed volume and a flat bottom, increasing the contact angle at the cell surface, decreasing the contact angle at the flat plate, decreasing the cell depth and decreasing the cell sidewall steepness increased the fraction of liquid removed from the cell and the time it took for the liquid bridge to split.

- Ahmed *et. al.* simulated the stretching and breaking of two-dimensional symmetric bridges of shear-thinning liquids between a stationary flat plate and a flat plate

that vertically moved up [21]. For low contact angles at the upper plate, the minimum thickness of the liquid between the two plates showed oscillatory or unstable behavior. The fraction of liquid transferred to the upper plate first increased and then decreased with increasing contact angle on the upper plate. Increasing the velocity of the upper plate reduced the fraction of liquid transferred to the upper plate, while increasing the surface tension coefficient increased it. The number of satellite droplets formed and the time for liquid stretching were higher for the shear-thinning liquids compared to the Newtonian liquids. The number of satellite drops formed increased, as the velocity of the upper plate increased.

- Lee *et. al.* simulated axisymmetric bridges of viscoelastic FENE-P liquids that stretched between a stationary cell and a vertically moving flat plate [22]. Liquid contact lines were pinned on the flat plate and the cell corners in the simulations. For sufficiently high separation velocities, elastic stresses that were activated during the early times of bridge stretching caused the drainage of the liquid into the cell. When gravitational forces reinforced this elastic drainage (cell is located below the flat plate), the competition of gravitational and elastic effects with the viscous forces that promote liquid transfer to the flat plate resulted in an optimal disk velocity that maximized the fraction of liquid transferred to the flat plate.

- Dodds *et. al.* simulated the stretching of three-dimensional Newtonian liquid bridges between a stationary flat plate and a moving flat plate [24]. In the simulations, the liquid bridge was initially cylindrical, the contact lines on both plates were pinned, and inertial and gravitational effects were not present. When the bridge was stretched under extension and shear, the bridge broke at its mid-point, so the drops resting on either plate had the same shape and volume after breakup. When the bridge was stretched under extension and rotation, the amount of liquid resting on the stationary plate was higher, as the breakup was approached. For the extension of non-cylindrical bridges with moving contact lines, dynamic wetting, which is characterized through a contact line friction parameter, influenced the liquid transfer process significantly. The contact line velocity decreased with increasing contact line friction, leading to contact line pinning at high enough contact line friction. Hence, increasing the contact line friction on the substrate surface helped maintaining the fidelity of the initial bridge pattern.

- Dube *et. al.* investigated the stretching and splitting of two-dimensional liquid bridges between a stationary porous flat plate and an impermeable vertically moving flat plate using a two-dimensional phase-field model. The amount of liquid left on the porous flat plate increased with decreasing pore size [18].

- Darhuber *et. al.* simulated the splitting of three-dimensional liquid bridges between a stationary flat plate and a vertically moving flat plate in the absence of inertial and gravitational effects using the Surface Evolver software [25]. When the

contact lines were free to move on both plates, the fraction of liquid transferred to the moving plate increased, as the contact angle at the moving plate decreased, in agreement with the results of Dodds *et. al.* [14]. Placing a rectangular hydrophilic region on the stationary plate imposed a rectangular shape to the contact lines of the liquid bridge on both plates before the plate motion began. However, as the liquid bridge stretched, the contact lines moved inwards and attained a circular shape.

- Schwartz *et. al.* simulated the evolution of the liquid-air interface over an array of cells during printing [19]. The fraction of the Newtonian liquid that remained in the two-dimensional cells after printing increased, as the size of the cells got smaller. The fraction of the shear-thinning liquid that was removed due to gravity from a three-dimensional cell on a stationary vertical surface increased, as the cell orientation changed from square to diamond, and as the cell size increased.

These studies indicate that ink properties, specifications of the stamp, substrate and cell surfaces, size and geometry of the cells on the engraved roller, and printing speed are some of the parameters that influence the liquid transport in roll-based printing systems.

In this study, the phase-field method is used to simulate the transfer of Newtonian ink from an axisymmetric cell on the surface of an engraved roller to the surface of a stamp wrapped on a printing cylinder. The phase-field method is selected due to its effectiveness in simulating the liquid ink transport in roll-based printing systems, as described in Chapter 3. The inertial effects are small and the gravitational effects are neglected due to the small size of the cell; and the contact lines are free to move on both roller surfaces that are represented as vertically separating flat plates in the phase-field simulations. The phase-field simulations are used to investigate the effect of the cell specifications and the printing conditions on the cell evacuation.

When printing at specified conditions using small cells that enable high-resolution printing, corresponding to ink transfer at fixed capillary number and approximately zero Reynolds number, the shape of the cells on an ink-metering roller is the major determinant of the amount of liquid removed from them. In this study, the emphasis is given on analyzing the effects of the cell sidewall inclination angle on the amount of the ink removed from the cells. Cell sidewall inclination angle is a cell design parameter than can be used to control the printed layer thickness. In addition, cells with different sidewall inclination angles can be used to represent the cells with irregular surface topography on new materials and new roller designs that can be implemented for stamp inking during high-resolution roll-based printing (such as the pores on porous materials or cells fabricated with poor control over cell geometry due to manufacturing difficulties at small length scales). The cell sidewall inclination angle is an important geometric parameter whose effects on the axisymmetric cell evacuation need to be thoroughly understood; yet, this effect in the presence of contact line slip has not been the focus of the existing numerical models.

The effect of the cell sidewall inclination angle on the flow of Newtonian ink out of axisymmetric cells in the presence of contact line slip under negligible inertial effects and in the absence of gravity is examined for the first time in this study. Furthermore, axisymmetric cells with different sidewall inclination angles are used to represent the cells with irregular surface topography on new materials and new roller designs that could be used for stamp inking during high-resolution roll-based printing, and in this way, the effect of the irregular cell surface topography on the evacuation of the cells is investigated also for the first time in this study.

This study will be a pioneer in spreading and widening the implementation of the phase-field method to simulate the liquid transport in roll-based printing systems, as the scientific and industrial need for high quality printing increases.

References

[1] B. R. Munson, D. F. Young and T. H. Okiishi, "Fundamentals of Fluid Mechanics", John Wiley & Sons, 1900.

[2] B. J. Kirby, "Micro- and Nanoscale Fluid Mechanics. Transport in Microfluidic Devices", Cambridge University Press, 2010.

[3] N. K. Adam, "Use of the term "Young's Equation" for contact angles", Nature, 1957.

[4] E. Buckingham, "On physically similar systems, illustrations of the use of dimensional equations", Physical Review Letters, 1914.

[5] H. Kipphan, "Handbook of Printing Media", Springer, 2001.

[6] European Comission, "Final Vision Document in Roll-to-Roll Printed Electronics Manufacturing Equipment, Production Lines and Systems", Deliverable Report.

[7] R. Bollstrom, "Roll-to-roll fabrication of low-cost paper-based electronic devices and sensors", FunMat Annual Seminar, 2013.

[8] R. C. Kattumenu, "Flexography Printing of Silver Based Conductive Inks on Packaging Substrates", PhD Thesis, Western Michigan University, 2008.

[9] S. Kumar, "Liquid Transfer in Printing Processes: Liquid Bridges with Moving Contact Lines", Annual Review of Fluid Mechanics, 2015.

[10] R. Kitsomboonloha *et. al.,* "Femtoliter-Scale Patterning by High-Speed, Highly Scaled Inverse Gravure Printing", Langmuir, 2012.

[11] A. Vornbrock, "Roll Printed Electronics: Development and Scaling of Gravure Printing Techniques", PhD Thesis, University of California Berkeley, 2009.

[12] Kang *et. al.,* "High-Performance Printed Transistors Realized Using Femtoliter Gravure-Printed Sub-10 Micron Metallic Nanoparticle Patterns and Highly Uniform Polymer Dielectric and Semiconductor Layers", Advanced Materials, 2012.

[13] H. W. Kang *et. al.*, "Liquid transfer between two separating plates for micro-gravure-offset printing", Journal of Micromechanics and Micorengineering, 2009.

[14] S. Dodds *et. al.,* "Stretching and Slipping of Liquid Bridges Near Plates and Cavities", Physics of Fluids, 2009.

[15] W. -X. Huang *et. al.,* "Simulation of Liquid Transfer Between Separating Walls for Modeling Micro-Gravure-Offset Printing", International Journal of Heat and Fluid Flow, 2008.

[16] F. Ghadiri *et. al.,* "Non-Newtonian Ink Transfer in Gravure-Offset Printing", International Journal of Heat and Fluid Flow, 2011.

[17] N. Hoda and S. Kumar, "Boundary Integral Simulations of Liquid Emptying From a Model Gravure Cell", Physics of Fluids, 2008.

[18] M. Dube *et. al.,* "Hydrodynamics of Ink Transfer".

[19] L. W. Schwartz *et. al.,* "Numerical Modeling of Liquid Withdrawal from Gravure Cavities in Coating Operations", Trans IChemE, 1998.

[20] C. A. Powell *et. al.,* "Modelling the Meniscus Evacuation Problem in Direct Gravure Coating", Trans IChemE, 2000.

[21] D. H. Ahmed *et. al.*, "Simulation of non-Newtonian ink transfer between two separating plates for gravure-offset printing", International Journal of Heat and Fluid Flow, 2011.
[22] J. A. Lee and M. Pasquali, "Computational study of viscoelastic effects on liquid transfer during gravure printing", Journal of Non-Newtonian Fluid Mechanics, 2013.
[23] S. Dodds *et. al.*, "Stretching liquid bridges with moving contact lines: the role of intertia", Physics of Fluids, 2011.
[24] S. Dodds *et. al.*, "The dynamics of three-dimensional liquid bridges with pinned and moving contact lines", Journal of Fluid Mechanics, 2012.
[25] A. A. Darhuber *et. al.*, "Physical mechanisms governing pattern fidelity in microscale offset printing", Journal of Applied Physics, 2001.
[26] A. K. Sankaran *et. al.*, "Effect of viscoelasticity on liquid transfer during gravure printing", Journal of Non-Newtonian Fluid Mechanics, 2012.
[27] J. P. Trungale, "The Anilox Roll: Heart of the Flexo Process", Jelmar Publishing Company, 1997.
[28] X. Yin and S. Kumar, "Flow visualization of the liquid-emptying process in scaled-up gravure grooves and cells", Chemical Engineering Science, 2006.
[29] www.flexoconsultant.com

Chapter 3. Phase-field Method

Different methods are used for two-phase flow simulations such as the marker and cell method, the volume of fluid method, the continuum surface force method and the level-set method. In this thesis, the phase-field method is implemented to simulate the two-phase flow in roll-based printing systems, since the phase-field method enables simulating flows with topology changes, moving and deforming interfaces, slipping contact lines and complex rheology easily, and provides a realistic representation of the liquid behavior consistent with thermodynamics. The remaining of this chapter is an explanation and expansion of the phase-field method.

3.1. Introduction

Incompressible and immiscible multiphase flows can be simulated following two approaches: using a moving mesh, which deforms with the flow, or using a fixed mesh, which remains stationary relative to the flow [1].

In the moving mesh approach, the interface is tracked by the nodal points of a moving mesh, which deforms with the flow on both sides of it. For large interface deformations and topological changes, these methods are confronted with difficulties due to distortion and entanglement of the mesh elements. In contrast, in the fixed mesh methods, the mesh elements remain stationary, as the two phases move relative to them. Additional agents such as markers or indicator functions are used to follow the interface motion, instead of the nodal points of the mesh, which simplifies dealing with large deformations and topological changes.

The volume of fluid method [2], the level set method [3] and the phase-field method [4] are all interface capturing methods based on the fixed mesh approach. Their indicator functions (Ω) are the volume fraction indicating the fraction of a mesh element filled with a fluid, a distance function indicating the distance to the interface and a phase-field variable indicating mass concentration, respectively. Use of an indicator function for following the interface requires the solution of a transport equation,

$$\frac{\partial \Omega}{\partial t} + \nabla \cdot (\Omega \boldsymbol{u}) = -\nabla \cdot \boldsymbol{J}(\Omega) \tag{1}$$

in addition to the Navier-Stokes equations and the continuity equation in all three methods. In equation (1), the first term represents the change of Ω with time, the second term represents the convective transport of Ω and the third term represents the diffusive transport of Ω. $\mathbf{J}(\Omega)$ is the interfacial diffusion flux, and it is non-zero only in the phase-field method.

Another common property of the three interface capturing methods is that the interface separating the two phases is not sharp [1]. Interface thickness is distributed over the height of a mesh element in the volume of fluid method, and it

is defined by a parameter controlling the interface thickness in the level set and phase-field methods. Surface tension effects are represented as forces acting over the finite interface thickness in the Navier-Stokes equations.

While the use of the finite interface thickness is a numerical requirement in the volume of fluid and level set methods, this is physically motivated in the phase-field method. In the phase-field approach, the indicator function has the physical meaning of concentration, and the diffuse interface is the region, where the two phases mix, as in reality.

In this study, the phase-field method is explored to study the fluid transport in roll-based printing technologies. The history of the phase-field method is given below.

The theory describing multiphase systems was developed by Young, Laplace and Gauss in the early 19th century based on the assumption that the interfaces separating the different phases are sharp with zero thickness. In this sharp interface approach, physical quantities such as density are discontinuous across the interface and boundary conditions at the interface can be used to determine the magnitudes of the jumps.

A different approach, which is based on the assumption that the interfaces are diffuse with finite thickness, was proposed by Rayleigh [5] and van der Waals [6] at the end of the 19th century. Actually, the concept of a diffuse interface was not new and went back to Maxwell and Gibss [7], Poisson [8] and von Leibnitz [9]. Concretely, van der Walls predicted the thickness of the interface and showed that it becomes infinite as the critical point is approached in 1893 [6]. Later, Korteweg proposed an expression for capillary stresses and showed that they reduce to the surface tension when the diffuse interface approaches to a sharp interface [10].

In the first half of 20th century, Ginzburg and Landau generalized van der Waals' theory of critical phenomena to a general theory of second-order phase transition to describe phenomena such as ferromagnetism, superfluidity and superconductivity [11]. Then Cahn and Hilliard applied van der Waals' diffuse interface approach to binary mixtures and used it to describe nucleation and spinodial decomposition [12, 18]. Later this method was generalized to model phase separation of alloys and polymer blends [13]. Finally, in the mid 1970s, the diffuse interface approach was coupled to hydrodynamics, developing a set of conservation equations [14-16]. The approach was initially referred to as "model H" [16] and later the name "diffuse interface model" was introduced.

3.2. Theory of the Phase-Field Method

The general theory described below can be applied to any complex fluid with a properly defined free energy [17]. Thermal energy is not considered in this model.

3.2.1. Phase-field Variable

In a phase-field model for the incompressible flow of two immiscible fluids, the interface position is tracked by the phase-field variable (Φ), which is also known as the order parameter. Volume fractions of the two phases can be expressed in terms of Φ as,

$$V_{f1} = \frac{(1-\phi)}{2} \tag{1}$$

$$V_{f2} = 1 - V_{f1} = \frac{(1+\phi)}{2} \tag{2}$$

Hence, Φ has a value of -1 in fluid 1, +1 in fluid 2 and it varies in between across the diffuse interface, where the two fluids mix (Figure 3.1).

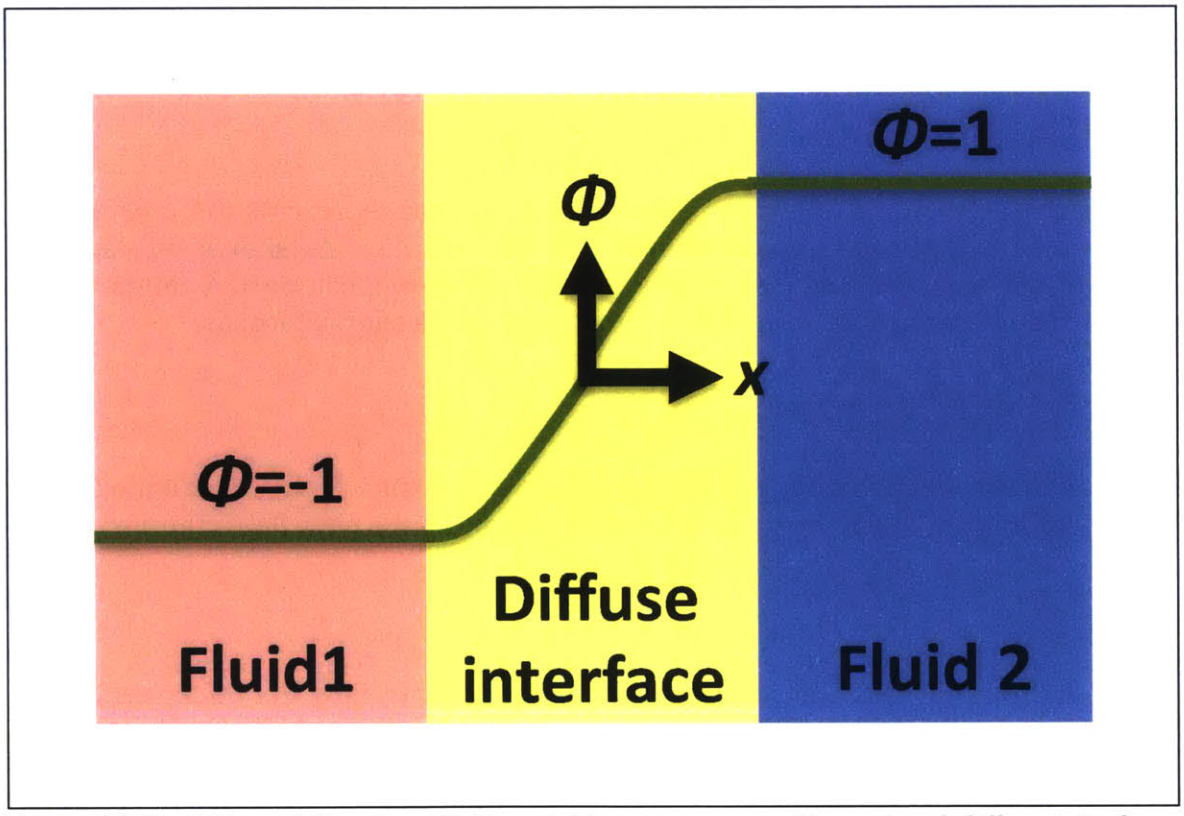

Figure 3.1 Variation of the phase-field variable across a one-dimensional diffuse interface, which separates fluid 1 and fluid 2.

3.2.2. Cahn-Hilliard Equation and Free Energy of the System

The governing equation for the phase-field variable is the advective Cahn-Hilliard equation,

$$\frac{\partial \phi}{\partial t} + \nabla \cdot (\phi \boldsymbol{u}) = \nabla \cdot (M \nabla G) \tag{3a}$$

$$G = \frac{\delta F}{\delta \phi} = f_0'(\phi) - \lambda \nabla^2 \phi \tag{3b}$$

Here, M is the mobility, λ is the mixing energy density parameter, f_0 is the bulk free energy density, F is the total free energy of the system and G is the chemical potential.

Cahn-Hilliard equation is a convection-diffusion equation representing the conservation of Φ. This equation can be obtained by expressing the interfacial diffusion flux in equation (1) to be proportional to the gradient of chemical potential, as $\mathbf{J}=-M\boldsymbol{\nabla}G$. It is consistent with the second law of thermodynamics, and hence minimizes the total free energy of the two-phase flow system [38, 40].

As indicated in equation 3b, chemical potential is the variational derivative of the total free energy of the system with respect to Φ. For a domain with volume Ω, total free energy of the system is,

$$F = \int_\Omega f_{mix}(\phi, \nabla\phi)\, d\Omega \tag{4}$$

In this expression, f_{mix} is the mixing energy density that represents the mixing and interactions of the two fluid components at the interface. As shown by van der Waals [6] and Cahn-Hilliard [19], f_{mix} depends on both composition and composition gradients, and it can be written in Ginzburg-Landau free energy form as,

$$f_{mix}(\phi, \nabla\phi) = \frac{1}{2}\lambda|\boldsymbol{\nabla}\phi|^2 + f_0(\phi) \tag{5a}$$

Based on mean field theory, the bulk free energy density, f_0, can be defined as a double-well potential having roots (ϕ=±1) representing the pure fluid components.

$$f_0(\phi) = \frac{\lambda}{4\varepsilon^2}(\phi^2 - 1)^2 \tag{5b}$$

Here, ε is the capillary width, which is a parameter controlling the thickness of the interface, as described below.

In equation 5a, the gradient term favors the complete mixing of the two phases and represents an attractive tendency between them, while the bulk free energy term favors the separation of the two phases into domains of pure components and represents a repulsive tendency between them. The competition between the two effects determines the profile of ϕ [17].

When the definition of bulk free energy given by equation (5b) is used, chemical potential becomes,

$$G = \lambda\left(-\nabla^2\phi + \frac{\phi(\phi^2-1)}{\varepsilon^2}\right) \tag{6}$$

For incompressible fluids, constant mobility, and the descriptions of bulk free energy density and chemical potential given by equations (5b) and (6), the Cahn-Hilliard equation becomes,

$$\frac{\partial\phi}{\partial t} + \boldsymbol{u}\cdot\boldsymbol{\nabla}\phi = \lambda M\nabla^2\left[-\nabla^2\phi + \frac{\phi(\phi^2-1)}{\varepsilon^2}\right] \tag{7}$$

For two-phase flows of Newtonian fluids, mixing energy is the only form of free energy representing the two-phase flow system. Additional energy terms need to be included in equation (5) to represent complex rheology.

3.2.3. Interfacial Tension and Capillary Width

For a one-dimensional planar interface at equilibrium, the profile of ϕ across the diffuse interface can be shown to be,

$$\phi(x) = \tanh\left(\frac{x}{\sqrt{2}\varepsilon}\right) \tag{8}$$

This expression can be obtained by setting the chemical potential given by equation (6) to zero to minimize the total free energy of the system, which represents equilibrium. Furthermore, conditions in the bulk of the two fluids are represented using $f_0(x=\pm\infty)=0$ and $d\phi/dx|_{x=\pm\infty}=0$. As the boundary condition, ϕ is set to be 0 at the mid-plane of the interface, which is the x=0 axis [17]. The resulting ϕ distribution corresponds to an interface thickness of 4.1641ε, across which 90% of the variation in ϕ takes place.

Equating the traditional surface energy in the sharp-interface approach to the mixing energy across a diffuse interface in equilibrium, interfacial tension (σ) can be expressed as,

$$\sigma = \frac{2\sqrt{2}}{3}\frac{\lambda}{\varepsilon} \tag{9}$$

3.2.4. Coupling of the Cahn-Hilliard Equation with the Navier-Stokes Equations

In phase-field simulations of two-phase flows, the Cahn-Hilliard equation is solved together with the continuity equation,

$$\boldsymbol{\nabla}\cdot\boldsymbol{u} = 0 \tag{10}$$

and the Navier Stokes equations,

$$\rho\left(\frac{\partial\boldsymbol{u}}{\partial t} + \boldsymbol{u}\cdot\nabla\boldsymbol{u}\right) = \boldsymbol{\nabla}\cdot[-p\boldsymbol{I} + \mu(\boldsymbol{\nabla u} + \boldsymbol{\nabla u}^T)] + \boldsymbol{F_g} + \boldsymbol{F_{st}} \tag{11}$$

Density and viscosity are linear functions of the phase-field variable. Defining ρ_1, ρ_2, μ_1 and μ_2 to be the density and dynamic viscosity in fluid 1 and fluid 2, total density (ρ) and total viscosity (μ) can be written in terms of ϕ as,

$$\rho = \rho_1\left(\frac{1-\phi}{2}\right) + \rho_2\left(\frac{1+\phi}{2}\right) \tag{12}$$

$$\mu = \mu_1\left(\frac{1-\phi}{2}\right) + \mu_2\left(\frac{1+\phi}{2}\right) \tag{13}$$

Gravity force (F_g) and surface tension force (F_{st}) can be written as [21]

$$\boldsymbol{F_g} = \rho \boldsymbol{g} \tag{14}$$

$$\boldsymbol{F_{st}} = G\boldsymbol{\nabla}\phi \tag{15}$$

Alternative ways of representing surface tension effects in the Navier-Stokes equations are possible such as expressing them in the stress term [4, 17, 22].

3.2.5. Simulation Parameters

The phase field method can be viewed as a tool to represent the microscopic physics of the interface. In applications, such as solidification [37] and near critical systems [4, 16], where the interface profile is of direct interest, it is crucial to ensure that the Cahn-Hilliard equation captures the interface dynamics. For instance, crystal growth during the solidification of a binary alloy takes place through solute transport across the solid/liquid interface. To accurately model the transport process, phase-field model parameters need to be connected to the physical parameters describing solidification [38]. On the other hand, for two-phase flows of immiscible fluids, the Φ profile has little direct effect on the macroscopic properties of the flow, other than determining the position and movement of the interface. This creates some flexibility in choosing the parameters of the phase-field model [22]. Some criteria for selection of ε, γ and λ are indicated below.

Capillary width (ε)

As indicated by equation (8), ε determines the thickness of the diffuse interface between the two fluids in the phase-field models. Interface thickness is on the order of the molecular size, that is Angstroms for simple fluids and nanometers for polymer mixtures [23]. Furthermore, as $\varepsilon \rightarrow 0$, the phase-field model converges to its sharp interface limit [4]. Mathematically, this limit relates the diffuse interface picture to the classical Navier-Stokes description of interfaces having zero thickness.

In phase-field simulations of two-phase flows, use of realistic interface thickness values may not be needed or may not be feasible due to the high computational cost of resolving large gradients across thin interfaces with small mesh elements. Hence, ε can be picked to be inside one's computational reach, and to produce

approximately the correct macroscopic behavior [22]. When there is a disparity between the interface thickness and the global length scale of the two-phase flow, use of adaptive mesh refinement to obtain a locally refined grid inside the interface region would be beneficial.

In simulations with drastic topology changes, variations in ε can lead to changes in simulation results. For instance, for the head on collusion of two drops, when the two drops have large interface thickness, overlap of the interfaces takes place earlier and more readily, and no liquid is trapped during coalescence. For smaller interface thickness, coalescence is prolonged and the dimple shape obtained by the drops leads to liquid trapping [24].

Mobility (M)

Mobility is the diffusivity of chemical potential. This parameter resembles the local mass diffusivity between the fluids, which takes place at the interface level on a molecular scale, but a conceptually amenable direct measurement of it is not obvious [25]. As an example, the mobility can be obtained from measurements of diffusivity (D) by expressing the chemical potential gradient (∇G) in terms of concentration gradient (∇c) to correlate the mobility and diffusivity ($\mathbf{J}=-M\nabla G=-D\nabla c$) for mass transport in a single-component alloy at a fixed uniform temperature in the dilute limit [38].

The mobility tuning parameter (χ), which is defined as M/ε^2, is used to determine the value of M for a specified ε. As ε is reduced to reach the sharp interface limit, it is recommended to reduce the mobility in proportion to the square of the interface thickness to maintain the effective interface force consistent with the required surface tension based on matched asymptotic analysis [25]. This condition is satisfied if χ is taken to be a constant.

The effect of mobility on the evolution of interfaces is investigated in [26]. For large values of mobility, evolution of the interface does not fully occur because of too much diffusion. On the other hand, for small values of mobility, non-smooth concentration profiles are observed. Hence, the suitable mobility value should be chosen in between the two limits. In the free energy Lattice Boltzmann simulations of [27], mobility is interpreted as the responsivity of the interface to local changes, and two drops are reported to coalesce more easily for high values of mobility.

Mixing energy density parameter (λ)

Based on equation (9), the mixing energy density parameter is chosen to yield the desired surface tension for a specified interface thickness.

3.3. Advantages and Challenges

Some advantages of phase-field modeling are listed below.

1. The thermodynamic description of an interface depends on its free energy density [6], and hence the Cahn-Hilliard theory is consistent with the physical description of an interface. As a result of this, phase-field models contain the short-range molecular forces, which are involved in rupture and merging of interfaces, and they make a realistic representation of topology changes. To illustrate, phase-field models can exhibit disjoining pressures, which build up when two interfaces come very close due to short-range molecular interactions [24, 39].

2. Moving interfaces and topological changes can be easily simulated using the phase-field method. Since the phase-field method uses a fixed mesh, problems due to deformation and entanglement of the mesh are eliminated, and no special treatments (such as artificial removal of a thinning neck) are needed to model topological changes.

3. Complex rheology can be easily included in phase-field models through the addition of extra free energy terms that represent the microstructure dynamics into the total free energy term of the Cahn-Hilliard equation. As an example, [17] uses bulk distortion energy and anchoring energy terms to represent the orientational distortion of rod-like molecules in nematic drops.

The major challenge of the phase-field method is the computational cost of resolving thin interfaces with small mesh elements.

3.4. Phase-field Simulations of Fluid Flows with Topological Changes

Phase-field models of fluid flows are used in many areas such as non-Newtonian flows [17, 24], microtube flows [28], droplet impact on a solid surface [29], drop spreading on a partially wetting substrate [20], marangoni convection [30], and spinodial decomposition under gravity and shear flow [31]. In this section, four topology change examples are given, as they relate to the splitting liquid bridges encountered in roll-based printing.

Breakup of Liquid Threads

In [32], Rayleigh capillary instabilities leading to breaking up of a liquid thread into droplets are simulated using the phase-field methods. Initially, a high-pressure field in the center of the liquid thread forces the liquid to move symmetrically off the center and creates a necking region at the center of the thread. Then, high-pressure fields formed at two off-center positions move the central necking region symmetrically off the center and result in satellite drop formation. In this model, a level set type continuum surface force formulation [36] is used in the Navier-Stokes

equations to be able to calculate the pressure field directly from the governing equations.

Pinch-off of Liquid-Liquid Jets

In [33], flow of a liquid jet from a nozzle into a liquid reservoir is investigated using a phase-field model. As the liquid jet is stretched by gravity, it forms necks that elongate, get thinner, and eventually breakup the jet into droplets. In [35], the breakup of simple and compound jets in coflowing conditions (specifically, the process of drop formation in flow-focusing devices) is investigated using a phase-field model. The flow regimes that prevail in different parameter ranges and effects of viscoelasticity on drop formation are explored.

Microdroplet Deposition Based on Liquid Flow Control

In [34], deposition of a droplet from the end of a capillary onto a cylindrical substrate is simulated using the phase-field method. In the deposition process, initially a liquid drop is trapped between the tip of the capillary and the substrate surface. As the drop flows back into the capillary due to pressure changes, part of it is left on the substrate. It is shown that the deposited volume mainly depends on the capillary-substrate distance and the substrate wettability.

Head-on Collusion of Two Drops

In [17, 24], the head-on collusion between two drops is studied using the phase-field method. The drops are initially stationary and separated by a specified distance. A body force is applied on the drops until the drop velocity attains a prescribed value. After the body force is turned off, the drops keep moving due to inertia, and they eventually collide and coalesce. A filament of surrounding liquid can be trapped between the coalescing drops.

The slip of the contact lines on a solid wall is incompatible with the no-slip condition and results in a stress singularity at the contact lines. As can be seen in some of the studies mentioned above, the phase-field method removes the stress singularity and enables the contact lines to slip on a solid wall naturally, as a result of Cahn-Hilliard diffusion, resulting in a realistic description of the contact line slip [41].

3.5. Summary

The phase-field method enables simulating immiscible multiphase flows on a fixed mesh using a phase-field variable to determine the position of the interface. The evolution of the phase-field variable is governed by the Cahn-Hilliard equation, which is an advection-diffusion equation representing the conservation of the phase-field variable. The Cahn-Hilliard equation minimizes the free energy of the two-phase flow system through diffusive interfacial fluxes, which are proportional to chemical potential gradients. The interface has a finite thickness across which the

two phases mix, and the free energy of the two-phase flow system consists of the mixing energy of the two phases. In this energy-based description, the structure of the interface is rooted in molecular forces and the behavior of the two-phase system is consistent with thermodynamics.

The capillary width, the mobility and the mixing energy density parameter are the input parameters to the phase-field models that should be chosen carefully to obtain accurate simulation results. The capillary width controls the thickness of the diffuse interface. As the interface thickness is reduced, the phase-field model approaches to its sharp interface limit. This limit represents a real interface having thickness on the Angstrom level the best in a micron-scale flow problem. Since it is computationally expensive to simulate thin interfaces, the capillary width can be chosen within one's computational reach in the phase-field simulations. The mobility represents the diffusivity of the chemical potential and it should be reduced in proportion to the square of the interface thickness, as the sharp interface limit is reached. The mixing energy density parameter should be chosen to yield the desired surface tension coefficient.

Liquid transfer in roll-based printing systems takes place through the stretching and splitting of liquid bridges. The phase-field method is an effective tool to investigate the liquid transfer in roll-based printing systems due to the following reasons.

- Since the phase-field method is a fixed mesh method, it can easily simulate moving and deforming interfaces and topology changes, which are characteristics of the liquid bridges formed between the separating roller surfaces. This is an advantage of the phase-field method over moving mesh methods, which use the nodes of the computational mesh to track the interface position.

- The phase-field method can easily simulate the flows of fluids having complex rheology, such as inks used in roll-based printing that contain pigments and conductive particles, through the incorporation of energy terms that represent the particles in the flow into the free energy of the two-phase flow system. The energy-based link between microstructure and rheology would enable design of the particles in the ink for a specific printing application, and simultaneously the prediction of the flow characteristics of the ink, when developing new ink formulations. This is an advantage of phase-field modeling over other techniques used for simulating liquid transport in roll-based printing systems.

- The phase-field method provides a realistic description of the liquid transfer, since the energy-based description of the flow is consistent with thermodynamics and contains the effects of short-range molecular forces. This enables phase-field models to provide additional information (e.g. disjoining pressures that are effective during topology changes). Furthermore, the concept of the diffuse interface used in the phase-field models is realistic. These are advantages of the

phase-field method over other techniques used for modeling liquid transport, which are not physically motivated.

- Phase-field models describe the slip of the contact lines of the liquid bridges on the separating roller surfaces in a natural and realistic way. This makes phase-field modeling superior to other techniques used for modeling liquid transport in roll-based printing systems.

References

[1] A. Jafari and N. Ashgriz, "Numerical techniques for free surface flows: interface capturing and interface tracking", Encyclopedia of Microfluidics and Nanofluidics, 2014.

[2] C. W. Hirt and B. D. Nichols, "Volume of fluid (VOF) method for the dynamics of free boundaries", Journal of Computational Physics, 1981.

[3] S. Osher and R. P. Fedkiw, "Levet set methods: an overview and some recent results", Journal of Computational Physics, 2001.

[4] D. M. Anderson *et. al.*, "Diffuse interface methods in fluid mechanics", Annual Review of Fluid Mechanics, 1998.

[5] L. Rayleigh, "On the theory of surface forces. II. Compressible fluids", Philosophical Magazine, 1892.

[6] J. D. van der Waals, "The thermodynamic theory of capillarity under the hypothesis of a continuous variation of density", 1893. Reprinted in Journal of Statistical Physics, 1979.

[7] J. W. Gibbs, "On the equilibrium of heterogenous substances", Transactions of the Connecticut Academy of Arts and Sciences, 1876.

[8] S. D. Poisson, "Nouvelle Theorie de l'Action Capillaire. Bachelier", 1831.

[9] G. F. W. von Leibnitz, "Nouveaux Essais sur l'Entendement Humain", 1765.

[10] D.J. Korteweg, "Sur la forme que prennent les´equations du mouvements des fluides si l'on tient compte des forces capillaires caus´ees par des variations de densit´e consid´erables mais continues et sur la th´eorie de la capillarit´e dans l'hypoth`ese d'une variation continue de la densit´e", Archives N´eerlandaises des Sciences Exactes et Naturelles, 1901.

[11] L. D. Landau and E. M. Lifshitz, "Statistical Physics, Part I", Pergamon Press, 1980.

[12] J. W. Cahn and J. E. Hilliard, "Free energy of a non-uniform system. III. Nucleation in a two-component incompressible fluid", Journal of Chemical Physics, 1959.

[13] P. G. de Gennes, "Dynamics of fluctuations and spinodal decomposition in polymer blends", Journal of Chemical Physics, 1980.

[14] K. Kawasaki, "Kinetic equations and time correlation functions of critical fluctuations", Annals of Physics, 1970.

[15] E. D. Siggia, "Late stages of spinodial decomposition in binary mixtures", Physical Review A, 1979.

[16] P. C. Hohenberg and B. I. Halperin, "Theory of dynamic critical phenomena", Reviews of Modern Physics, 1977.

[17] P. Yue *et. al.*, "A diffuse-interface method for simulating two-phase flows of complex fluids", Journal of Fluid Mechanics, 2004.

[18] J. W. Cahn, "On spinodial decomposition", Acta Metallurgica, 1961.

[19] J. W. Cahn and J. E. Hilliard, "Free energy of a non-uniform system. I. Interfacial free energy", Journal of Chemical Physics, 1958.

[20] C. Zhou *et. al.*, "3D phase-field simulations of interfacial dynamics in Newtonian and viscoelastic fluids", Journal of Computational Physics, 2010.

[21] R. Acar, "Simulation of interface dynamics: a diffuse-interface model", The Visual Computer, 2008.
[22] J. J. Feng *et. al.*, "An energetic variational formulation with phase field methods for interfacial dynamics of complex fluids: advantages and challenges", Modeling Soft Matter, The IMA Volumes in Mathematics and its Applications, 2005.
[23] "Multiphase Microfluidics: The Diffuse Interface Model", editor: Roberto Mauri, in CISM International Centre for Mechanical Sciences: Courses and Lectures, 2012.
[24] P. Yue *et. al.*, "Diffuse interface simulations of drop coalescence and retraction in viscoelastic fluids", Journal of Non-Newtonian Fluid Mechanics, 2005.
[25] F. Magaletti *et. al.*, "The sharp-interface limit of the Cahn-Hilliard/Navier-Stokes model for binary fluids", Journal of Fluid Mechanics, 2013.
[26] H. G. Lee *et. al.*, "On the long time simulation of the Rayleigh-Taylor instability", International Journal for Numerical Methods in Engineering, 2010.
[27] O. Shardt *et. al.*, "Simulations of drop coalescence in simple shear flow", Langmuir, 2013.
[28] Q. He and N. Kasagi, "Phase-field simulations of small capillary number two-phase flows in a microtube", Fluid Dynamics Resarch, 2008.
[29] V. V. Khatavkar *et. al.*, "Diffuse interface modeling of drop impact", Journal of Fluid Mechanics, 2007.
[30] R. Borcia and M. Besterhorn, "Phase-field for marangoni convection in liquid-gas systems with a deformable interface", Physical Review E, 2003.
[31] V. E. Badalassi and S. Banerjee, "Nano-structure computation with coupled momentum phase ordering kinetics models", Nuclear Engineering and Design, 2005.
[32] J. Kim, "A continuous surface tension force formulation for diffuse-interface models", Journal of Computational Physics, 2005.
[33] C. –H. Kim and S. –H. Shin, "Phase-field model for the pinchoff of liquid-liquid jets", Journal of the Korean Physical Society, 2009.
[34] W. Villanueva *et. al.*, "Microdroplet deposition under a liquid medium", Langmuir, 2007.
[35] C. Zhou *et. al.*, "Formation of simple and compound drops in microfluidic devices", Physics of Fluids, 2006.
[36] J. U. Brackbill *et. al.*, "A continuum method for modeling surface tension", Journal of Computational Physics, 1992.
[37] W. J. Boettinger *et. al.*, "Phase-field simulations of solidification", Annual Review of Materials Research, 2002.
[38] Nikolas Provatas and Ken Elder, "Phase-Field Methods in Material Science and Engineering", Wiley, 2010.
[39] D. Jacqmin, "Calculation of two-phase Navier-Stokes flows using phase-field modeling", Journal of Computational Physics, 1999.
[40] C. M. Elliot, "The Cahn-Hilliard model for the kinetics of phase separation", Mathematical Models for Phase Change Problems, 1989.
[41] D. Jacqmin, "Contact-line dynamics of a diffuse fluid interface", Journal of Fluid Mechanics, 2000.

Chapter 4. Phase-Field Simulations of Liquid Splitting Between Separating Flat Plates

As demonstrated in Chapter 3, the phase-field method is an effective tool to investigate the two-phase fluid transport in roll-based printing systems. Phase-field modeling should be performed using suitable simulation parameters to accurately describe the transport process. In this chapter, the influence of the simulation parameters on the results of the phase-field simulations of axisymmetric liquid bridge splitting between separating flat plates is investigated.

4.1. Problem Description

The axisymmetric system shown in its initial configuration in Figure 4.1a is modeled using the phase-field method to investigate the effect of the simulation parameters on the simulation results. The modeled system consists of a cylindrical liquid ink drop trapped between two flat plates with an initially straight interface between the drop and the air surrounding it. After the two-phase system reaches its equilibrium state with a curved liquid-air interface, the upper plate is set into motion in the z-direction, so the liquid ink stretches and splits into two (Figure 4.1b). During the entire process, the contact lines are free to move on the lower stationary plate and pinned on the upper plate.

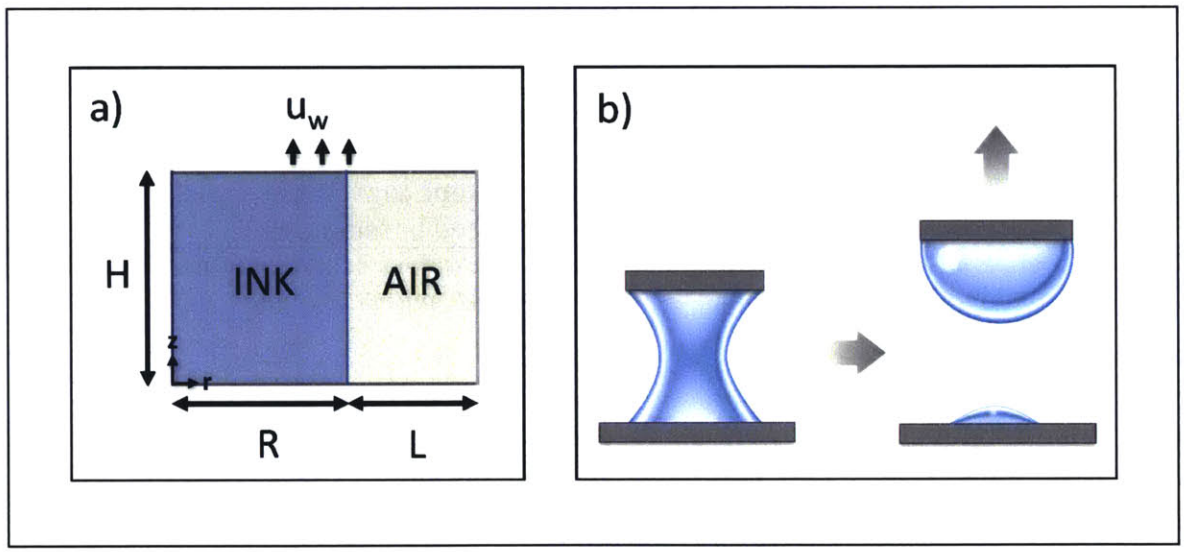

Figure 4.1 Schematics describing the simulation domain and the liquid transfer process. a) Schematic of the simulation domain in its initial configuration. Simulation domain is axisymmetric along the z-axis. b) A liquid bridge between two flat plates in its equilibrium state before the upper plate starts moving, and the two drops formed after splitting (adapted from [2]).

Simulation details are shown in Table 4.1. The values of the printing parameters used in the simulations are in the range used in roll-based printing. Gravitational and inertial effects are neglected in the simulations, since they are dominated by

viscous and surface tension effects due to the small size of the liquid ink drop (for $Ca=\mu_{ink}.u_w/\sigma=0.01$, $Re=\rho_{ink}.u_w.R/\mu_{ink}=0.02$, $Bo=\rho_{ink}.g.R^2/\sigma=8x10^{-5}$, the relative magnitudes of the forces affecting the liquid ink flow are: gravitational force<<inertial force<<viscous force<<surface tension force). Both the liquid ink and the air are modeled as incompressible Newtonian fluids. The modeled system with an initial contact line diameter (2R) equal to the initial distance between the two plates (H) corresponds to the system modeled in [1]. This system enables validation of the phase-field models against [1], and also represents the liquid ink transport from the stamp features to the substrate surface in roll-based printing systems.

Initial contact line radius (R)	25 μm
Initial distance between flat plates (H)	50 μm
Radius of the simulation domain (R+L)	60 μm
Velocity of the upper plate (u_w)	0.09 m/s (for $t_{simulation}$>500 μsec)
Material properties	ρ_{ink}=1000 kg/m^3, μ_{ink}=0.0078 Pa.sec, ρ_{air}=1.16 kg/m^3, μ_{air}=1.81x10^{-5} Pa.sec σ=0.07 N/m
Contact angles	. Contact lines are pinned on top plate . $\theta_{bottom}=70^o$
Dimensionless numbers characterizing liquid ink flow	Re=0 (inertial effects neglected) Bo=0 (gravitational effects neglected) Ca=0.01
Capillary width (ε)	. 0.25 μm ≤ ε ≤ 3 μm . ε is reduced to approach the sharp interface limit
Mobility tuning parameter (χ)	. 0.1 m.s/kg ≤ χ ≤ 10 m.s/kg . χ is kept constant at 1 m.s/kg, as ε is reduced based on [6]

Table 4.1 Details of the liquid splitting simulations. The values of the printing parameters used in the simulations are in the range used in roll-based printing.

4.2. Formulation

The fluid dynamics are described by the Navier-Stokes equations with the convective and gravity terms neglected, and the continuity equation in the phase-field simulation.

$$\rho\left(\frac{\partial \boldsymbol{u}}{\partial t}\right) = \boldsymbol{\nabla}\cdot[-p\boldsymbol{I} + \mu(\boldsymbol{\nabla u} + \boldsymbol{\nabla u}^T)] + G\boldsymbol{\nabla}\phi \quad (1)$$

$$\boldsymbol{\nabla}\cdot\boldsymbol{u} = 0 \quad (2)$$

In equation (1), density (ρ) and dynamic viscosity (μ) of the two-phase system linearly depend on the phase-field variable (ϕ).

$$\rho = \rho_{liq}\left(\frac{1-\phi}{2}\right) + \rho_{air}\left(\frac{1+\phi}{2}\right) \tag{3}$$

$$\mu = \mu_{liq}\left(\frac{1-\phi}{2}\right) + \mu_{air}\left(\frac{1+\phi}{2}\right) \tag{4}$$

Evolution of the liquid-air interface is modeled using the convective Cahn-Hilliard equation.

$$\frac{\partial \phi}{\partial t} + \boldsymbol{u}\cdot\boldsymbol{\nabla}\phi = \lambda M \nabla^2\left[-\nabla^2\phi + \frac{\phi(\phi^2-1)}{\varepsilon^2}\right] \tag{5}$$

Since the higher (4^{th}) order of the Cahn-Hilliard equation causes numerical complications, it can be split into two second-order partial differential equations [3].

$$\frac{\partial \phi}{\partial t} + \boldsymbol{u}\cdot\boldsymbol{\nabla}\phi = \boldsymbol{\nabla}\cdot\frac{\lambda M}{\varepsilon^2}\boldsymbol{\nabla}\psi \tag{6a}$$

$$\psi = -\boldsymbol{\nabla}\cdot\varepsilon^2\boldsymbol{\nabla}\phi + (\phi^2-1)\phi \tag{6b}$$

For the boundary conditions, an axisymmetric condition is used on the left simulation domain boundary. On the right simulation domain boundary, total stress in the tangential direction is zero, normal stress is specified as 1 atm, and the phase-field variable is set to 1 indicating the existence of pure air. At the top and bottom walls, the wall velocity ($\mathbf{u_w}$) is set equal to the fluid velocity ($\mathbf{u}$), and the contact angle (θ) is specified,

$$\boldsymbol{u} = \boldsymbol{u}_w \tag{7}$$

$$\boldsymbol{n}\cdot\varepsilon^2\boldsymbol{\nabla}\phi = -\varepsilon^2\cos(\theta)\,|\boldsymbol{\nabla}\phi| \tag{8}$$

The no-slip condition imposed by equation (7) implies that the motion of the contact lines on the top and bottom walls is entirely due to Cahn-Hilliard diffusion. Furthermore, a no penetration condition is satisfied at both walls by imposing conditions on a phase-field help variable (ψ).

$$n\cdot\frac{\lambda M}{\varepsilon^2}\boldsymbol{\nabla}\psi = 0 \tag{9}$$

Since $G=(\lambda/\varepsilon^2)\psi$, equation (9) indicates that flux of phase-field variable ($\mathbf{J}=-M\boldsymbol{\nabla}G$) normal to the walls is zero.

As the initial condition, pressure (p) is set to be 1 atm, and u and ψ are set to be zero in the entire simulation domain. For Φ, the tangent hyperbolic variation obtained for a flat interface in equilibrium is used.

$$\phi_0 = \begin{cases} -\tanh\left(\frac{D_{wi}}{\sqrt{2}\varepsilon}\right) & in\ ink \\ \tanh\left(\frac{D_{wi}}{\sqrt{2}\varepsilon}\right) & in\ air \end{cases} \quad (10)$$

In equation (10), D_{wi} indicates the distance to the initial interface.

The commercial finite element package COMSOL Multiphysics is utilized for the solution. First, D_{wi} is solved in an initialization step. Then it is used in equation (10) to form the initial condition for Φ for use in the transient solution. In the transient solution, equations (1), (2), (6a) and (6b) are solved for u, p, ϕ and ψ subject to the boundary and initial conditions.

4.3. Computational Mesh

The simulation domain shown in Figure 4.1a is discretized by two-dimensional triangular mesh elements with linear elements for pressure and quadratic elements for velocity. The mesh is free to deform with the motion of the upper plate. Mesh deformation is achieved by restricting the displacement or velocity of the mesh elements in specified directions at the simulation domain boundaries. At the top boundary of the simulation domain, corresponding to the moving plate, mesh velocity is set equal to the plate velocity. At the left and right boundaries of the simulation domain, the mesh elements are free to move along the z-direction and not allowed to move in the r-direction. At the bottom boundary, corresponding to the stationary plate, no mesh motion is allowed. Simulations are performed using either a segmented uniform mesh or adaptive mesh refinement.

In the segmented uniform mesh approach, first, preliminary simulations are performed to identify the sections of the simulation domain that are swept by the interface. Next, the simulation domain is divided into two: the region swept by the interface (liquid region) and the region not swept by the interface (air region). The maximum mesh element sizes in these two regions are referred to as Δh_{liq} and Δh_{air}, respectively. Δh_{liq} is set to be small enough to resolve the interface and independent of Δh_{air} to reduce the simulation time (Figure 4.2).

In the adaptive mesh refinement approach, the liquid-air interface is tracked with refined mesh elements having sizes smaller than those in the rest of the simulation domain. As in the uniform mesh approach, the simulation domain is divided into two segments. The interface stays in the liquid region during the simulations, and the mesh elements that track the interface are refined relative to the mesh elements in the liquid region (Figure 4.3).

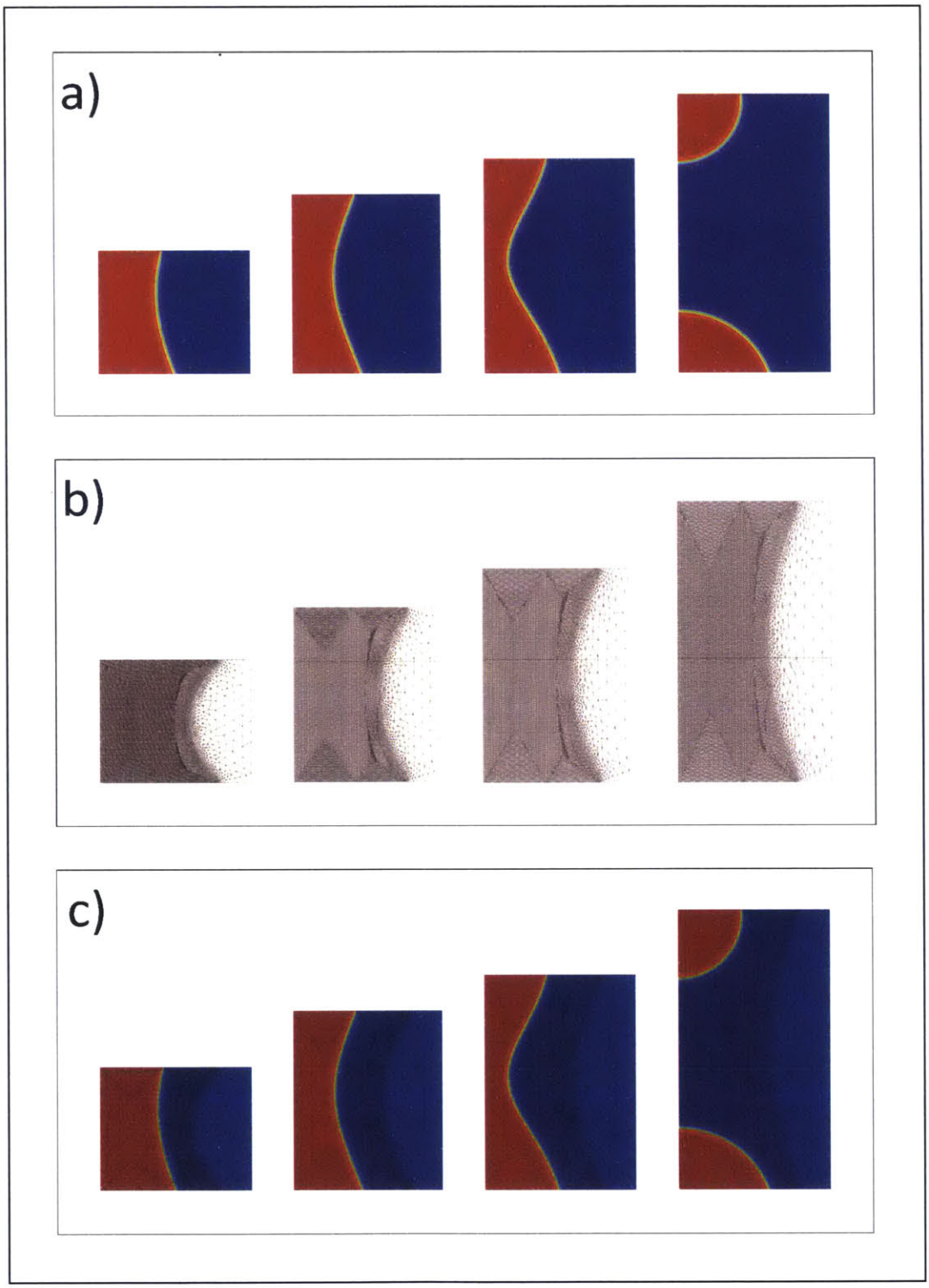

Figure 4.2 Phase-field simulation results for liquid splitting between separating flat plates obtained using a segmented uniform mesh. a) Volume fractions of liquid (shown by red color) and air (shown by blue color). b) Computational mesh. c) Plots of volume fraction and computational mesh placed on top of each other. The first frame shows the liquid in its equilibrium configuration at the beginning of the stretching process. Time intervals between the frames are 250μsec, 160μsec and 290μsec from left to right. Parameters of Test 1 in Table 4.4 are used in the simulation.

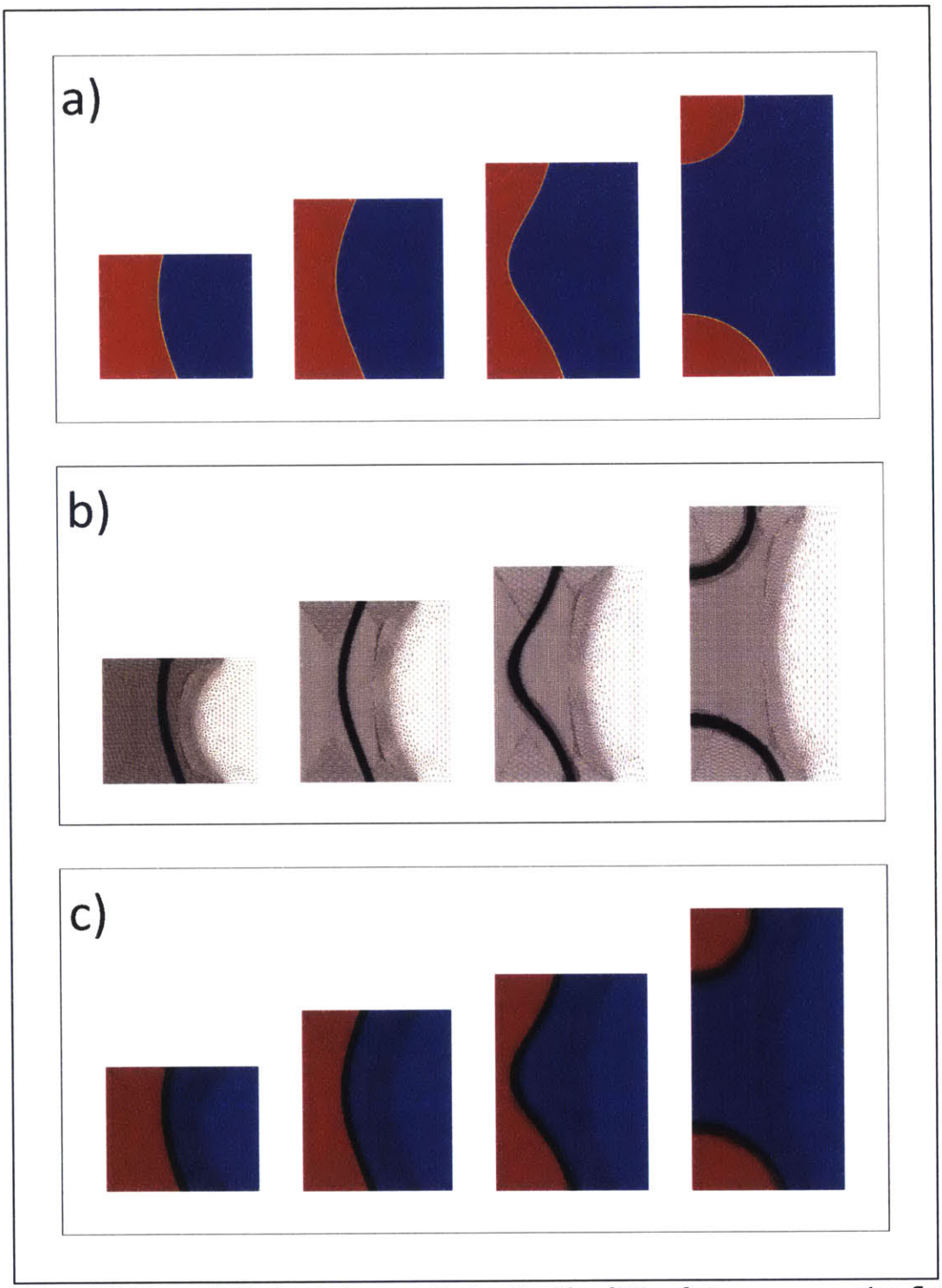

Figure 4.3 Phase-field simulation results for liquid splitting between separating flat plates obtained using adaptive mesh refinement. a) Volume fractions of liquid (shown by red color) and air (shown by blue color). b) Computational mesh. c) Plots of volume fraction and computational mesh placed on top of each other. The first frame shows the liquid in its equilibrium configuration at the beginning of the stretching process. Time intervals between the frames are 250μsec, 160μsec and 290μsec from left to right. Parameters of Test 1 in Table 4.3 are used in the simulation.

An adapted mesh for use in $[t_n, t_{n+1}]$ is obtained by mapping the solution at $t=t_n$ to the base mesh, computing the solution at $t_s>t_n$ on the base mesh, evaluating an error indicator using the solution at t_s, and refining a fraction of the mesh elements that have the highest error indicator in COMSOL software. Defining the error indicator as $|\nabla\Phi|$ enables refining of the mesh elements that coincide with the interface. The solution at t_n is then mapped to the new adapted mesh for $[t_n, t_{n+1}]$ and time integration continues until the next mesh adaptation takes place at t_{n+1}.

Interval length (IL), maximum element refinements (MER) and element growth rate (EGR) are the main parameters that are used to control adaptive mesh refinement. The simulation time between two subsequent mesh refinements $(t_{n+1}-t_n)$ is defined as IL. As a result of mesh refinement, the total number of mesh elements increases roughly by 100x(EGR-1)%. MER specifies the maximum number of refinements of the mesh elements, and hence determines the minimum size of the refined mesh elements. Mesh elements are refined along their longest edge.

4.4. Effect of Simulation Parameters on the Simulation Results

Phase-field simulations are performed using different values of mesh element size, capillary width (ε) and mobility (M), and key simulation outputs (fraction of liquid transferred to the moving plate and time for liquid splitting (t_{split})) are compared. Simulation conditions tested and the simulation outputs are summarized in Tables 4.2, 4.3 and 4.4.

4.4.1. Effect of Mesh Element Size

Adaptive mesh refinement is used to set the mesh element size at the interface independent of the mesh element size at the rest of the simulation domain. Simulation results do not change, when IL is reduced below 20μsec for an EGR of 8.5, indicating that the interface is tracked sufficiently well by the refined mesh elements (Table 4.2). IL and EGR are set to be 10μsec and 8.5, respectively, in the rest of the simulations, unless otherwise is stated.

4.4.1.1. Effect of Mesh Element Size of the Liquid Region

Simulations are performed for values of Δh_{liq} between 0.5 μm and 3 μm, while the remaining simulation parameters are kept constant. In each simulation, MER is set to be sufficiently high to ensure that the interface is well-resolved. When Δh_{liq} is 0.5 μm, the computationally feasible maximum value of MER is 4. For higher values of Δh_{liq}, MER is set to be 20. EGR is 20 in the simulation having 3 μm for Δh_{liq}.

Simulation results do not change significantly, as Δh_{liq} is varied in the specified range (Tests 1-4 in Table 4.3) indicating that all the mesh element sizes tested suffice in resolving the liquid region.

4.4.1.2. Effect of Mesh Element Size of the Air Region

When Δh_{air} is varied between 2 μm and 10 μm, while the remaining simulation parameters are kept constant, no significant change is observed in the simulation results. This indicates that all values of Δh_{air} tested resolve the air region sufficiently well, and hence are suitable for use in the simulations (Tests 1, 5-6 in Table 4.3).

4.4.1.3. Effect of Interface Resolution

The effect of interface resolution on the simulation results is investigated by varying the value of MER to change the size of mesh elements tracking the interface in the phase-field simulations. When Δh_{liq} is set to be 1 μm and MER is increased above 5, no significant change in simulation results is observed, indicating that the interface is resolved sufficiently well (Tests 2, 7-8 in Table 4.3). However, for smaller values of MER, simulation results differ significantly (Tests 9, 10 in Table 4.3) and the interface has an unphysical appearance with sharp corners due to low interface resolution.

In summary, it is crucial that the interface is well-resolved to obtain accurate results in phase-field simulations of liquid splitting. Mesh element size in the liquid and air regions can be larger than that at the interface, since the largest gradients are across the interface in the simulations. Use of higher Δh_{liq} and Δh_{air} from the specified ranges would be beneficial to reduce the simulation time.

4.4.2. Effect of Interface Thickness

Simulations are performed using a segmented uniform mesh to investigate the effect of interface thickness on the simulation results. Δh_{liq} is fixed at 0.5 μm, and ε is varied between 1 μm and 3 μm in the simulations. Since $\Delta h_{liq} \leq \varepsilon/2$, the interface is well-resolved in all the simulations.

As the magnitude of ε is reduced, the phase-field simulations move closer to their sharp interface limit, transfer ratio decreases and t_{split} slightly increases (Tests 1-3 in Table 4.4, and Figure 4.4). Keeping the mobility tuning parameter ($\chi=M/\varepsilon^2$) constant at 1 m.s/kg ensures that M is reduced in proportion to ε^2, as recommended. It is not computationally feasible to perform simulations for values of ε below about 1 μm using the segmented uniform mesh. Hence, the simulations are closest to the sharp interface limit when adaptive mesh refinement is used with ε=0.25 μm (corresponding to the results shown in Table 4.3). There is less than 1% difference between the transfer ratio value obtained at ε=0.25 μm and that obtained by extrapolating the transfer ratio versus capillary width plot in Figure 4.4 to ε=0 μm. Since a real ink-air interface would have thickness on the order of Angstroms, the sharp interface limit describes the micron-scale liquid splitting process the best.

Test	Mesh characteristics					Results	
	Δh_{liq} (μm)	Δh_{air} (μm)	MER	IL (μsec)	EGR	Transfer ratio	t_{split} (μsec)
1	1	4.35	7	10	8.5	38.4%	950
2	1	4.35	7	20	8.5	38.4%	950
3	1	4.35	7	30	8.5	37.4%	980
4	1	4.35	7	50	8.5	36.0%	1030
5	1	4.35	7	100	8.5	40.8%	1340

Table 4.2 Results of simulations using adaptive mesh refinement for different values of IL. Simulation results do not change when IL is reduced below 20 μsec indicating that the interface is tracked sufficiently well by the refined mesh elements.

Test	Mesh characteristics			PF parameters		Results	
	Δh_{liq} (μm)	Δh_{air} (μm)	MER	ε (μm)	χ (m.s/kg)	Transfer ratio	t_{split} (μsec)
Results of simulations using adaptive mesh refinement							
Δh_{liq} changes							
1	0.5	4.35	4	0.25	1	38.6%	940
2	1	4.35	20	0.25	1	38.4%	950
3	2	4.35	20	0.25	1	38.5%	950
4	3	4.35	20	0.25	1	38.4%	950
Δh_{air} changes							
5	0.5	2	4	0.25	1	38.7%	940
1	0.5	4.35	4	0.25	1	38.6%	940
6	0.5	10	4	0.25	1	38.6%	940
Interface resolution changes							
2	1	4.35	20	0.25	1	38.4%	950
7	1	4.35	7	0.25	1	38.4%	950
8	1	4.35	5	0.25	1	38.3%	950
9	1	4.35	3	0.25	1	41.7%	980
10	1	4.35	2	0.25	1	57.8%	1340
χ changes							
11	2	4.35	7	0.25	10	35.3%	1020
12	2	4.35	7	0.25	1	38.5%	950
13	2	4.35	7	0.25	0.1	37.7%	1070

Table 4.3 Effect of simulation parameters on the results of phase-field simulations of liquid splitting between separating flat plates. Adaptive mesh refinement is used in the simulations. EGR is 20 in Test 4 and 8.5 in all other simulations. IL is 10μsec. Test 12 gives the best simulation results and its parameters are used for validating the simulation results against the literature.

Test	Mesh characteristics			PF parameters		Results	
	Δh_{liq} (μm)	Δh_{air} (μm)	MER	ε (μm)	χ (m.s/kg)	Transfer ratio	t_{split} (μsec)
Results of simulations using a segmented uniform mesh							
ε changes							
1	0.5	4.35	-	1	1	40.3%	950
2	0.5	4.35	-	2	1	43.8%	950
3	0.5	4.35	-	3	1	47.6%	940

Table 4.4 Effect of ε on the results of phase-field simulations of liquid splitting between separating flat plates. A segmented uniform mesh is used in the simulations.

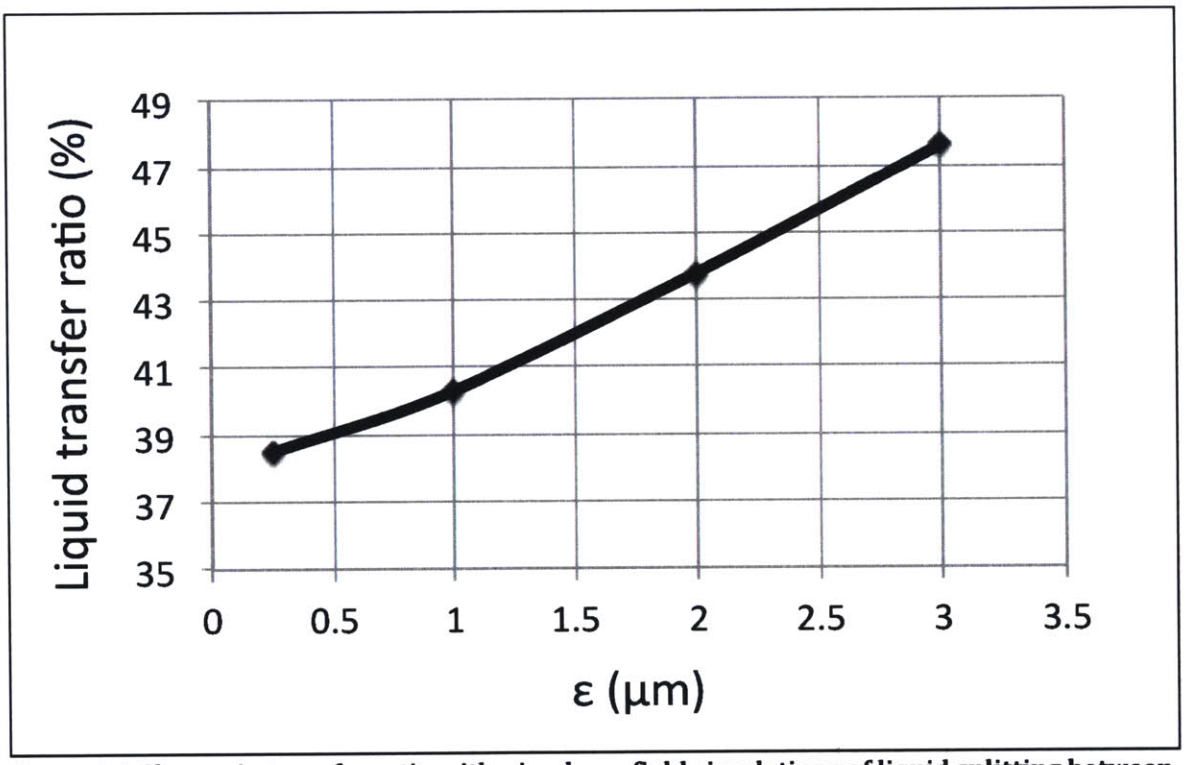

Figure 4.4 Change in transfer ratio with ε in phase-field simulations of liquid splitting between separating flat plates. The data point corresponding to the smallest ε is obtained using adaptive mesh refinement (Test 1 in Table 4.3). Other three data points are obtained using a segmented uniform mesh (Tests 1-3 in Table 4.4).

4.4.3. Effect of Interface Mobility

As χ is changed by two orders of magnitude between 0.1 m.s/kg and 10 m.s/kg with ε being fixed at 0.25 μm (the simulation is close to the sharp interface limit and the corresponding variation in the mobility is between 6.25×10^{-15} m^3.s/kg and 6.25×10^{-13} m^3.s/kg), the change in the magnitude of the liquid transfer ratio is not significant (Tests 11-13 in Table 4.3). In the rest of the simulations, χ is set to be 1 m.s/kg.

4.5. Validation of the Simulation Results

Phase-field simulations are validated against the numerical solution presented in [1]. Specifically, the liquid fractions transferred to the upper plate are compared between [1] and the phase-field model for different capillary numbers and contact angles on the bottom plate. As explained in Chapter 2, the stretching of axisymmetric liquid bridges with pinned and moving contact lines between vertically separating flat plates is simulated in [1]. This study has been the subject of a recent review [2] on liquid transfer in printing processes and it is amongst the limited number of studies that examine the stretching of axisymmetric liquid bridges with moving contact lines.

In the validation simulations, the simulation setting described in Figure 4.1a and Table 4.1, and the simulation parameters of Test 12 in Table 4.3 (ε=0.25 μm, χ=1 m.s/kg, Δh_{liq}=2 μm, Δh_{air}=4.35 μm, MER=7), which give the best simulation results, are used. For the selected phase-field parameters, the simulation results are close to the sharp interface limit and they are not significantly affected by the variations in the mobility. To simulate flows characterized by different capillary numbers, different values of surface tension are used. The computational mesh used in the simulations provides the required spatial resolution as shown in section 4.4.1. As the time steps used in the simulations are reduced, the liquid transfer ratio values change insignificantly (by about 1%) indicating that the required temporal resolution is achieved. Change in liquid mass is less than 0.3% during the simulations. Since non-conservative forms of the equations are used, mass is not conserved in the simulations. Backward difference formulation (BDF) with maximum order of 2 is used for time stepping and a direct solver is used to obtain the solution. Further details of the numerical implementation can be found in [4].

There is a close match between the transfer ratio values obtained from phase-field simulations and those presented in [1] as shown in Table 4.5. The relatively larger mismatch in the results at smaller capillary numbers is due to the higher sensitivity of liquid transfer ratio to variations in contact angle for smaller capillary number. When the contact line behavior on the two plates is reversed, the fraction of liquid remaining on the two plates is also reversed (Tests 3 and 5 in Table 4.5). This result is expected, since inertial effects are neglected in the simulations, and it confirms that simulations accurately predict the contact line motion on both a stationary plate and a moving plate.

After the liquid bridge splits, the drops on the lower and upper plates can exchange mass through diffusion to bring the system to its minimum energy configuration. Examples of similar situations are available in the literature [5]. Two-dimensional symmetric liquid splitting simulations, and an analysis on the effect of phase-field parameters on the mass exchange between the drops after splitting is presented in Appendix C.

Test	Descriptors of the flow			Results	
	θ_{top}	θ_{bottom}	Ca	Transfer ratio (phase-field)	Transfer ratio (Dodds *et. al.* [1])
Validation of simulation results against Dodds *et. al.* [1]					
1	pinned	50°	0.01	23%	24%
2	pinned	60°	0.01	28%	28%
3	pinned	70°	0.01	38%	36%
4	pinned	80°	0.01	82%	92%
5	70°	pinned	0.01	62% (=1-38%)	
6	pinned	60°	1	50%	49%
7	pinned	70°	1	51%	50%
8	pinned	90°	1	54%	53%

Table 4.5 Comparison of liquid transfer ratio values reported in [1] and obtained from the phase-field model. In Tests 1-4 and 6-8, contact lines are pinned on the upper moving plate and free to slip on the lower stationary plate with a specified contact angle. In Test 5, contact lines are pinned on the lower stationary plate and free to slip on the upper moving plate with specified contact angle. Parameters of Test 12 in Table 4.3 (Δh_{liq}=2 μm, Δh_{air}=4.35 μm, EGR=8.5, MER=7, IL=10 μsec, ε=0.25 μm, χ=1 m.s/kg) are used in the simulations.

References

[1] S. Dodds *et. al.*, "Stretching and slipping of liquid bridges near plates and cavities", Physics of Fluids, 2009.

[2] S. Kumar, "Liquid transfer in printing processes: liquid bridges with moving contact lines", Annual Review of Fluid Mechanics, 2015.

[3] J. J. Feng *et. al.*, "An energetic variational formulation with phase field methods for interfacial dynamics of complex fluids: advantages and challenges", Modeling of Soft Matter, inside: The IMA Volumes in Mathematics and its Applications, Springer, 2008.

[4] Reference Manual, COMSOL version 4.4.

[5] C. Liu and J. Shen, "A phase field model for the mixture of two incompressible fluids and its approximation by a Fourier-spectral method", Physica D, 2003.

[6] F. Magaletti et. al:, "The sharp-interface limit of the Cahn-Hilliard/Navier-Stokes model for binary fluids", Journal of Fluid Mechanics, 2013.

Chapter 5. Phase-Field Simulations of Cell Evacuation in Roll-Based Printing Technologies

The function of the cells on an ink transfer roller is to deliver a precise amount of ink to the stamp surface in a uniform way. Application of too much or too little ink to the stamp can lead to printing defects such as dot gain (printed pattern larger than desired) or pinholing (voids in printed area), and prevent the printing of patterns having thickness within a desired range. In this chapter, the effect of cell specifications and printing conditions on the ink release characteristics of axisymmetric cells having 2 μm opening width is investigated using the phase-field method. Specifically, the effect of the ink dynamic viscosity, the ink surface tension coefficient, the printing speed, the cell depth, the cell sidewall inclination angle, and the contact angles of the cell and stamp surfaces on the fraction of the liquid removed from the cells is investigated. A set of printing guidelines that aim to improve the quality of high-resolution roll-based printing is derived from the analysis of the simulation results. Furthermore, the cells with different sidewall inclination angles are used to represent the cells with irregular surface topography on new materials and new roller designs that can be implemented for inking stamp features. In this way, the effect of variable cell surface topography on the thickness of the printed patterns is investigated.

5.1. Description of the Simulated System

Transport of liquid ink from the axisymmetric cells on the surface of an ink transfer roller to the surface of stamp features is simulated using the phase-field method. The transport process is approximated as the stretching and splitting of a liquid bridge between a stationary cell and a vertically moving flat plate. A schematic of the simulation domain before the flat plate is set into motion is shown in Figure 5.1. Simulation details are shown in Table 5.1.

The cells used in all the simulations have an opening width of 2 μm enabling printing with higher resolution than the current industry standards. In the evacuation simulations of cells having different sidewall inclination angles, the volume of the liquid ink is chosen to yield a spacing of 0.07 μm between the free surface of the liquid ink and the upper surface of the cell, when all the ink rests in the cell forming a flat interface. This condition represents the state of the cells after blading, and leads to cells initially more than 85% full for the range of sidewall inclination angles investigated (60^o-90^o).

Formulation and numerical implementation are the same as in the validation simulations described in Chapter 4. The simulation domain is discretized using triangular mesh elements that are uniformly distributed across the simulation domain with linear elements for pressure and quadratic elements for velocity.

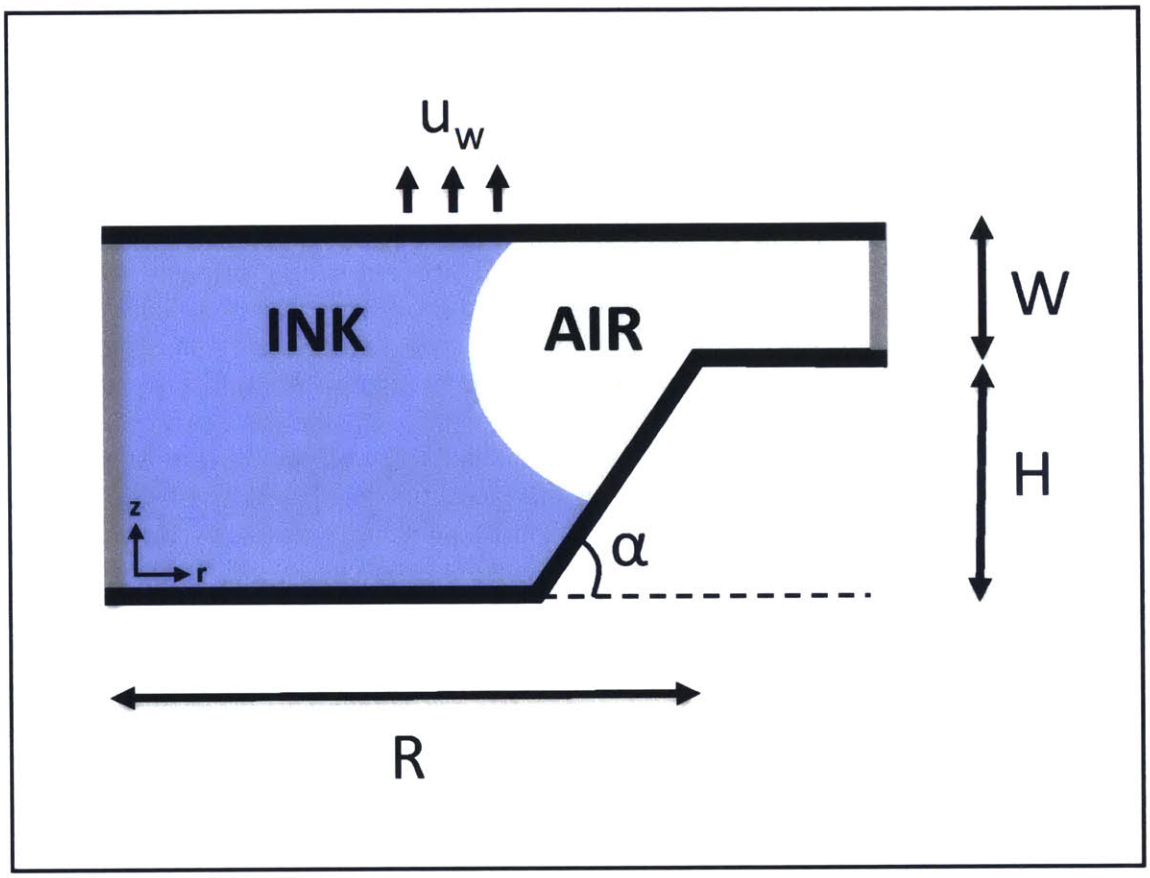

Figure 5.1 Schematic of the simulation domain before the flat plate is set into motion. The simulation domain is axisymmetric about the z-axis. Cell radius (R) is equal to 1 μm in all the simulations.

Cell radius (R)	1 μm
Cell height (H)	1-5 μm
Initial cell-plate spacing (W)	0.1 μm
Cell sidewall inclination angle (α)	60°-90°
Plate velocity (u_w)	0.02-0.09 m/sec (plate motion begins after the liquid ink reaches its equilibrium shape)
Contact lines	Free to move on both the flat plate and the cell with specified contact angles (θ_{plate} and θ_{cell})
Liquid ink volume	Results in a liquid height of about 0.93 μm, if all the liquid ink rests in the cell with a flat liquid-air interface
Material properties	ρ_{ink}=1000 kg/m^3, μ_{ink}=0.002-0.08 Pa.sec, ρ_{air}=1.16 kg/m^3, μ_{air}=1.81x10^{-5} Pa.sec σ=0.07 N/m
Dimensionless numbers characterizing the liquid ink flow	Ca=0.001-0.01 Re=0.001-0.011 (inertial effects are small) Bo=0 (gravitational effects are neglected)

Table 5.1 Details of the cell evacuation simulations.

5.2. Effect of Capillary Width and Mesh Element Size on the Simulation Results

The change in the fraction of liquid ink transferred to the flat plate with capillary width (ε) is investigated in a sample simulation ($\alpha=60^o$, $\theta_{plate}=50^o$, $\theta_{cell}=100^o$, $H=1\mu m$, $\mu_{ink}=0.0078$ Pa.sec, $u_w=0.09$ m/sec, $Ca=\mu_{ink}.u_w/\sigma=0.01$, $Re=\rho_{ink}.u_w.R/\mu_{ink}=0.01$). Mesh element size ($\Delta h$) is taken to be $\varepsilon/2$ to ensure that the interface is well-resolved. χ is taken to be 1 m.s/kg, as in the simulations described in Chapter 4. As $\varepsilon\rightarrow 0$, the fraction of liquid ink transferred to the flat plate approaches to about 17.3% (Figure 5.2). For ε being 0.04 μm, this fraction is about 1% higher in magnitude than that at the sharp interface limit. The rest of the simulations described in this chapter are performed using $\varepsilon=0.04$ μm, $\chi=1$ m.s/kg and $\Delta h=0.02$ μm. The change in the total liquid mass is less than 1% in all the simulations performed. Refinements of mesh element size and time steps ensure that adequate spatial and temporal resolution is achieved. When remeshing is performed on the computational mesh to minimize distortion of the mesh elements, the simulation results do not change.

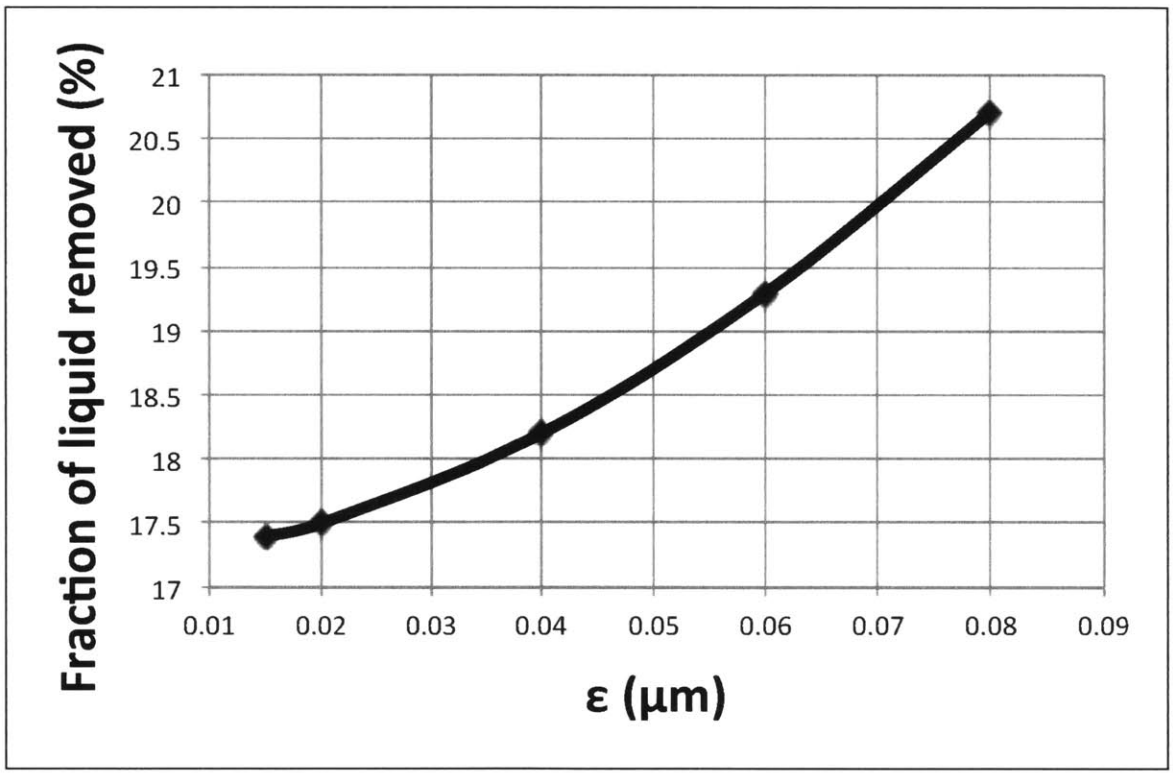

Figure 5.2 Change in the fraction of liquid ink removed from a cell with capillary width in phase-field simulations of cell evacuation. Mesh element size is taken to be $\varepsilon/2$. Details of the simulations are as described in Table 5.1 with $\alpha=60^o$, $\theta_{plate}=50^o$, $\theta_{cell}=100^o$, $H=1\mu m$, $\mu_{ink}=0.0078$ Pa.sec, $u_w=0.09$ m/sec. Liquid ink flow is characterized by Ca=0.01 and Re=0.01.

5.3. Effect of Cell Sidewall Inclination Angle on the Evacuation of Cells

Results of phase-field simulations for the evacuation of cells having 60°, 75° and 90° sidewall inclination angle are shown in Table 5.2 and Figure 5.3. In the simulations, $\theta_{plate}=50°$, $\theta_{cell}=100°$, $H=1\mu m$, $\mu_{ink}=0.0078$ Pa.sec, $u_w=0.09$ m/sec. Liquid ink flow is characterized by Ca=0.01 and Re=0.01.

For the cell having 60° sidewall inclination angle, the contact line radius on the flat plate is reduced by 20% until splitting. However, the contact line position on the cell surface is the same before the flat plate moves and at the moment of splitting. This result is in agreement with the simulation results of Dodds *et. al.* [1] which indicate that the contact line on the cell surface may get pinned during the evacuation of cells. Gradients in liquid ink pressure, which drive the ink away from the upper contact line and towards the bottom contact line, are responsible for the different contact line behavior on the flat plate and cell surfaces.

As the cell sidewall inclination angle increases from 60° to 90°, the upper contact line slips closer to the axis of symmetry of the system, and the contact line on the cell wall moves to a higher vertical position than its initial position, until splitting. This results from strengthening of the pressure gradients that drive the ink away from the upper contact line, and reduces the amount of ink removed from the cell. Since the total ink mass increases and the amount of ink removed from the cell decreases with increasing cell sidewall inclination angle, the fraction of ink removed from the cell decreases as the cell sidewalls are made steeper (Table 5.2).

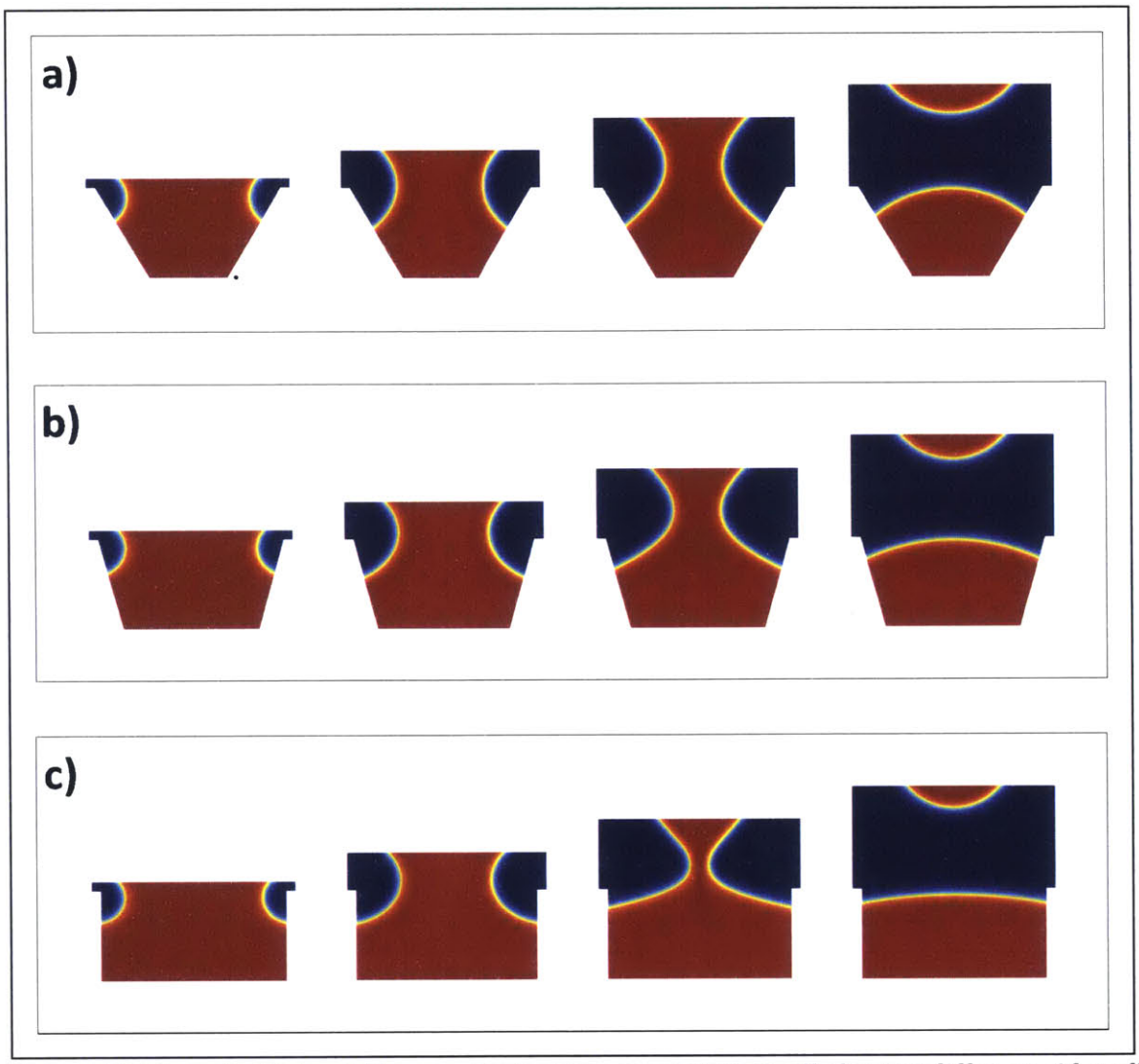

Figure 5.3 Phase-field simulation results for the evacuation of cells having different sidewall inclination angles. The cells used in the simulations have sidewall inclination angles of: a) 60°, b) 75°, and c) 90°. Details of the simulations are as described in Table 5.1 with θ_{plate}=50°, θ_{cell}=100°, H=1μm, μ_{ink}=0.0078 Pa.sec, u_w=0.09 m/sec. Liquid ink flow is characterized by Ca=0.01 and Re=0.01. The first frame shows the liquid ink in its equilibrium state at the beginning of plate motion. Time interval between the frames is 4 μsec. Red indicates liquid ink and blue indicates air.

α	Total ink volume	Ink volume removed	Ink fraction removed
60°	1.46μm^3	0.266 μm^3	18.2%
75°	2.15μm^3	0.168 μm^3	7.8%
90°	2.92μm^3	0.126 μm^3	4.3%

Table 5.2 Total ink volume, volume of ink removed from the cells and fraction of ink removed from the cells in phase-field simulations of cell evacuation. Cells have sidewall inclination angles of 60°, 75° and 90°. Details of the simulations are as described in Table 5.1 with θ_{plate}=50°, θ_{cell}=100°, H=1μm, μ_{ink}=0.0078 Pa.sec, u_w=0.09 m/sec. Liquid ink flow is characterized by Ca=0.01 and Re=0.01.

5.4. Effect of Contact Angles on the Evacuation of Cells Having Different Sidewall Inclination Angles

Figure 5.4 shows the change in the fraction and the mass of liquid ink removed from cells having 75° and 90° sidewall inclination angle for different contact angles on the flat plate and cell surfaces. In the simulations, H=1μm, $\theta_{plate} \leq 60°$, $\theta_{cell} \geq 100°$, μ_{ink}=0.0078 Pa.sec, u_w=0.09 m/sec. The ink flow is characterized by Ca=0.01 and Re=0.01.

As the plate surface is made less wettable and the cell surface is made more wettable (the difference between the contact angles of the two surfaces is reduced), the mass of ink removed from cells having both 75° and 90° sidewall inclination angle is reduced. Since the total ink mass remains constant as the difference between the contact angles is reduced, the fraction of ink removed from the cells is also reduced. This result is in agreement with Young-Dupre equation, which states that a liquid adheres more strongly to a more wettable surface. In terms of contact line behavior, this result can be explained by the higher tendency of the contact lines to spread over a more wettable surface.

The cell with 75° sidewall inclination angle releases more ink than the cell with 90° sidewall inclination angle for all the contact angle combinations tested. When the difference between the contact angles of the plate and the cell surfaces increases, the difference between the mass of ink removed from cells having 75° and 90° sidewall inclination angle increases.

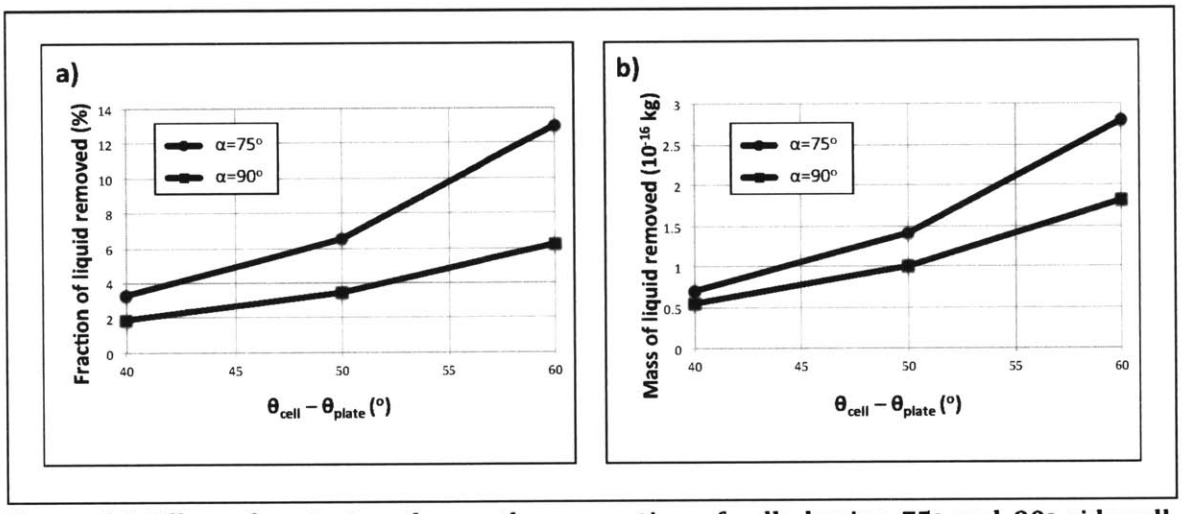

Figure 5.4 Effect of contact angles on the evacuation of cells having 75° and 90° sidewall inclination angle in the phase-field simulations. a) Change in the fraction of liquid ink removed from the cells, and b) change in the mass of liquid ink removed from the cells, as the difference between the contact angles (Δθ) on the flat plate (θ_{plate}) and the cell surfaces (θ_{cell}) is varied. In the simulations with Δθ=40°, θ_{plate}=60° and θ_{cell}=100°. In the simulations with Δθ=50°, θ_{plate}=55° and θ_{cell}=105°. In the simulations with Δθ=60°, θ_{plate}=50° and θ_{cell}=110°. Other details of the simulations are as described in Table 5.1 with H=1 μm, μ_{ink}=0.0078 Pa.sec, u_w=0.09 m/sec. Liquid ink flow is characterized by Ca=0.01 and Re=0.01.

5.5. Effect of Capillary Number on the Evacuation of Cells Having Different Sidewall Inclination Angles

The fraction and the mass of liquid ink removed from cells having 75° and 90° sidewall inclination angle decrease, as the capillary number decreases from 0.01 to 0.001 for Re being small (0.01-0.001) (Figure 5.5). This result is in agreement with the results of existing simulations [1, 2] and experiments [3]. In the simulations, $\theta_{plate}=50^{o}$, $\theta_{cell}=110^{o}$, H=1μm. Ink flows characterized by Ca=0.001, 0.005 and 0.01 have $\mu_{ink}=0.0026$ Pa.sec, 0.013 Pa.sec and 0.0078 Pa.sec, and $u_w=0.027$ m/sec, 0.027 m/sec and 0.09 m/sec, respectively. The effect of the variation of Re on the simulation results is negligible, since the inertial effects have no significant influence on the ink flow for Re ≤ 0.01.

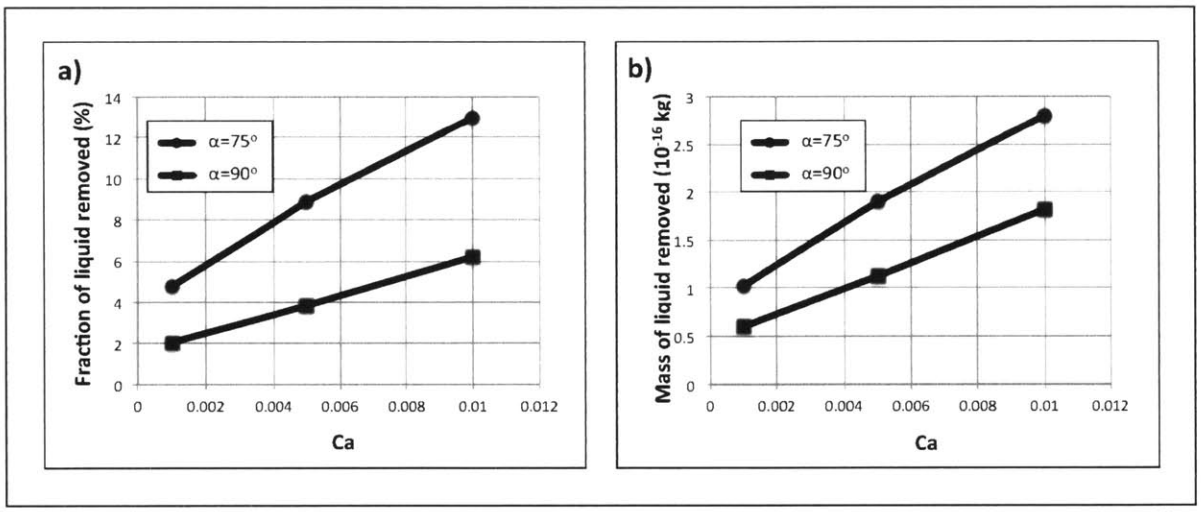

Figure 5.5 Effect of capillary number on the evacuation of cells having 75° and 90° sidewall inclination angle in the phase-field simulations. a) Change in the fraction of liquid ink removed from the cells, and b) change in the mass of liquid ink removed from the cells with capillary number. Simulation details are as described in Table 5.1 with $\theta_{plate}=50^{o}$, $\theta_{cell}=110^{o}$, H=1μm. The ink flow is characterized by Ca=0.001-0.01 and Re=0.001-0.01. Ink flows characterized by Ca=0.001, 0.005 and 0.01 have $\mu_{ink}=0.0026$ Pa.sec, 0.013 Pa.sec and 0.0078 Pa.sec, and $u_w=0.027$ m/sec, 0.027 m/sec and 0.09 m/sec, respectively.

The change in the amount of ink removed from the cells with Ca is related to the changes in contact line mobility. For lower Ca, the interface has less ability to deform, so the contact lines have to slip more to keep the contact angle constant on the cell and plate surfaces, as the liquid ink bridge stretches. Hence, the decrease in Ca leads to faster slip of the contact lines on the flat plate and cell surfaces. As a result, the upper contact line moves closer to the axis of symmetry of the system and the lower contact line moves to a higher vertical position on the cell wall than its initial position, until splitting. This reduces the amount of ink removed from the cells.

In the phase-field simulations, dynamic viscosity of the liquid ink and the velocity of the flat plate are varied to change the value of Ca. Liquid ink flows characterized by

different Ca can also be obtained by using inks having different surface tension coefficient.

5.6. Effect of Cell Depth on the Evacuation of Cells Having Different Sidewall Inclination Angles

Results of phase-field simulations for the evacuation of cells having 75° and 90° sidewall inclination angle and variable depth are shown in Figure 5.6 and Figure 5.7. In the simulations, θ_{plate}=50°, θ_{cell}=110°, μ_{ink}=0.0078 Pa.sec, u_w=0.09 m/sec, and the ink flow is characterized by Ca=0.01 and Re=0.01. Maximum cell depth is 2μm and 5μm for the cells with 75° and 90° sidewall inclination angle, respectively.

Increase of the cell depth above 1μm influences the stretching of the liquid bridge insignificantly (Figure 5.7). Hence, the amount of ink removed from cells having 75° and 90° sidewall inclination angle remains almost unchanged, as the cell depth increases (Figure 5.6b). However, the total ink mass increases with cell depth, and this reduces the fraction of ink removed from the cells (Figure 5.6a).

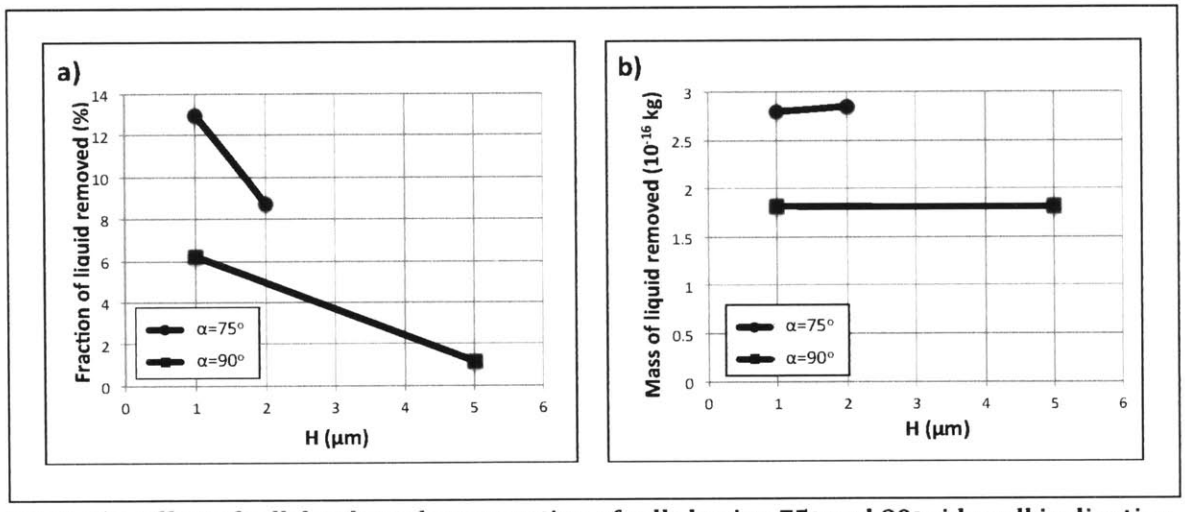

Figure 5.6 Effect of cell depth on the evacuation of cells having 75° and 90° sidewall inclination angle in the phase-field simulations. a) Change in the fraction of liquid ink removed from the cells, and b) change in the mass of liquid ink removed from the cells with cell depth. The simulation details are as described in Table 5.1 with θ_{plate}=50°, θ_{cell}=110°, μ_{ink}=0.0078 Pa.sec, u_w=0.09 m/sec. The liquid ink flow is characterized by Ca=0.01 and Re=0.01.

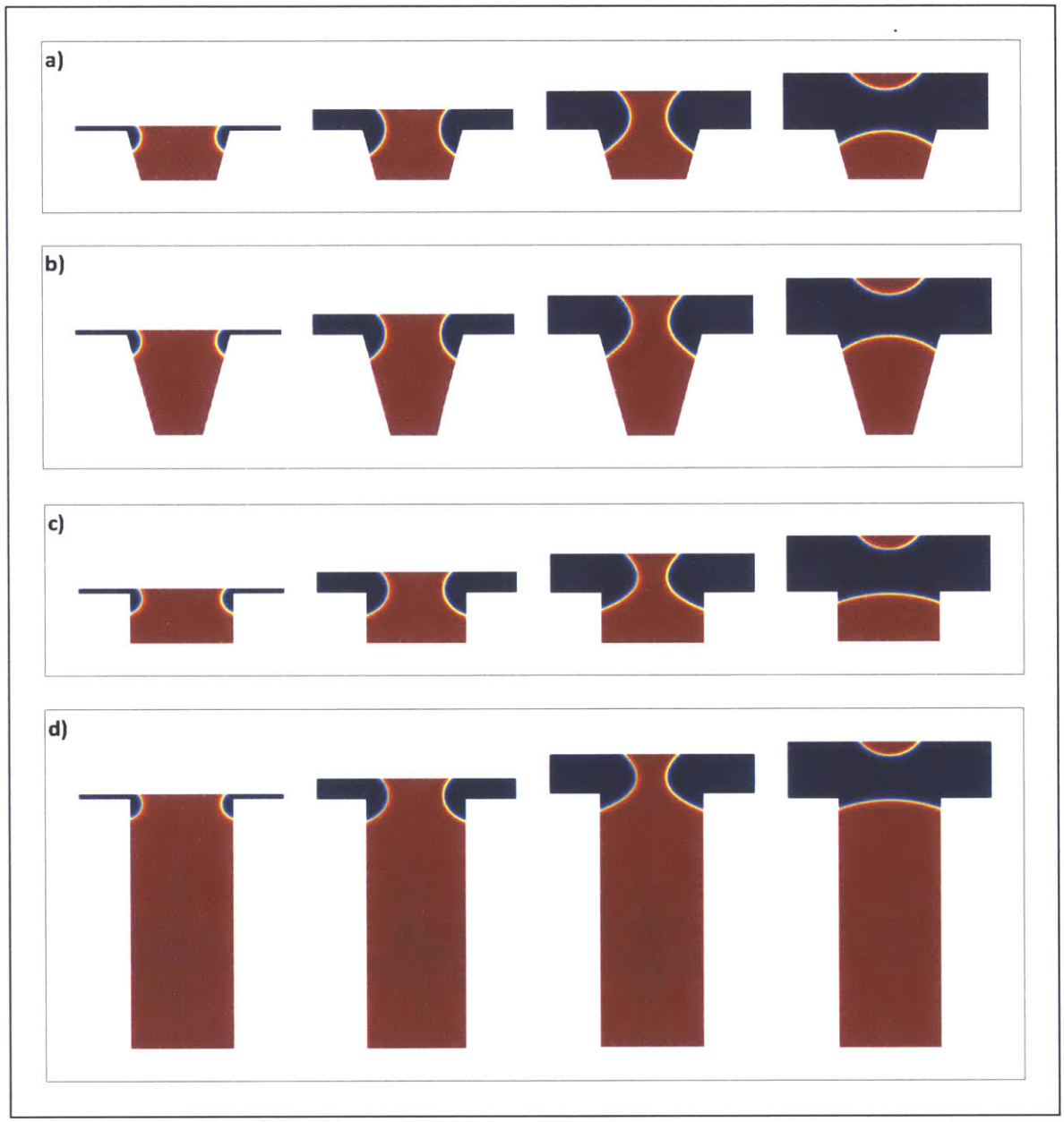

Figure 5.7 Phase-field simulation results for the evacuation of cells having variable sidewall inclination angle and depth. The cells used in the simulations have: a) 75° sidewall inclination angle and 1μm depth, b) 75° sidewall inclination angle and 2μm depth, c) 90° sidewall inclination angle and 1μm depth, d) 90° sidewall inclination angle and 5μm depth. Details of the simulations are as described in Table 5.1 with θ_{plate}=50°, θ_{cell}=110°, μ_{ink}=0.0078 Pa.sec, u_w=0.09 m/sec. The ink flow is characterized by Ca=0.01 and Re=0.01. The first frame shows the liquid in its equilibrium state at the beginning of plate motion. Time interval between the frames is 4μsec. Red indicates liquid ink and blue indicates air.

5.7. Guidelines for High-Resolution Roll-Based Printing

The simulation results indicate that as the cell sidewall inclination angle increases, the amount of ink removed from the cells decreases in the range of printing parameters investigated (plate with high wettability, cell with low wettability, Re=0.001-0.01, Ca=0.001-0.01). The amount of ink removed from cells having different sidewall inclination angles increases, as the wettability of plate surface increases, wettability of cell surface decreases and the capillary number characterizing the ink flow increases. To obtain ink flows characterized by higher capillary numbers, printing speed can be increased, and inks having higher dynamic viscosity and lower surface tension coefficient can be used.

These results can be implemented in roll-based printing applications, as follows.

- If excessive ink transfer leads to printing defects and printed patterns thicker than required, the ink should be transferred from the cells to the stamp at lower capillary number and the cell surface wettability should be increased. The opposite action needs to be taken, if too little ink is transferred to the substrate.

- The cells with lower sidewall inclination angle will print thicker patterns than the cells with steeper sidewalls under the same printing conditions. Hence, if patterns having equal thickness will be printed using two cell types with different sidewall inclination angles, then the cells with steeper walls should be used at higher capillary numbers with lower cell surface wettability.

The simulation results presented in this chapter also provide cell design guidelines to minimize cell clogging. The cells on the surface of ink transfer rollers do not fully evacuate during printing. When the cells return to the ink reservoir, part of the ink remaining in the cells may stick to the cell walls and it may not be replaced by fresh ink. As printing proceeds, a thin layer of ink (originating from the accumulation of the old ink) may start solidifying on the cell surface and eventually lead to cell clogging. This situation is more prominent, if the viscosity of the ink left in the cells increases due to evaporation. Plugging impairs the ability of the cells to deliver predictable amounts of ink consistently, and damages the cell surface. Furthermore, plugged cells may lead to printing defects such as striations (lines of weak ink or no ink in the direction of print run) and screening (smalls voids in the printed area having regular shape consistent with the cell pattern on the roll).

Phase-field simulation results show that increasing cell depth above 1 μm does not affect the quantity of ink removed from the cells, but it leads to more residual ink remaining in them (meaning it reduces the fraction of liquid removed from the cells). Since this higher amount of residual ink may cause clogging issues, it is beneficial to use cells having depth values as small as possible. Similarly, the cells with smaller sidewall inclination angle have less residual ink after printing than the cells with steeper sidewalls. Hence, use of cells with smaller sidewall inclination

angle is expected to minimize plugging. In general, printing of thicker layers with high resolution would require utilizing the residual ink at the bottom of the deep cells. This can be accomplished by using magnetic or charged inks with the deep cells, and applying electric and magnetic fields to the ink to help cell evacuation during printing.

5.8. Prediction of Printed Layer Thickness During High-Resolution Roll-Based Printing

Placing the cells having 2 μm opening width on the surface of an ink transfer roller with 0.5 μm spacing would result in a roller line screen (L_s) of 4000 cells per cm, which is equivalent to 10,160 cells per inch. Table 5.3 shows how the specifications of this ink transfer roller and the maximum thickness of the ink film that can be formed on the stamp surface ($t_{max,stamp}$) would change, as the sidewall inclination angle of the cells on the roller surface vary in the range used in the simulations for a cell depth of 1 μm. In this table, the ink carrying capacity of the ink transfer roller is expressed in units of BCM/inch^2, where BCM indicates billion cubic microns. The below expression is used to calculate $t_{max,stamp}$.

$$t_{max,stamp}[\mu m] = \frac{\left(L_s[\frac{cell}{cm}]\right)^2 (V_{cell}[\mu m])}{10^8} \quad (1)$$

Here, V_{cell} is the volume of a single cell, which is assumed to be the maximum volume of the ink that can be held by the cell. The thickness of the liquid film on the stamp surface is maximized, when all the ink in the cells is released. Table 5.3 indicates that $t_{max,stamp}$ varies between about 0.27 μm and 0.50 μm for the cell geometries investigated.

Cell Specifications			Roller Specifications		
Sidewall Angle	**Depth**	**Volume**	**Line screen**	**Ink Capacity**	**$t_{max,stamp}$**
60°	1 μm	1.68 μm^3	10,160 cells/inch	0.17 BCM/inch^2	0.27 μm
75°	1 μm	2.38 μm^3	10,160 cells/inch	0.25 BCM/inch^2	0.38 μm
90°	1 μm	3.14 μm^3	10,160 cells/inch	0.32 BCM/inch^2	0.50 μm

Table 5.3 Change in the roller specifications and the maximum thickness of the liquid film that can be formed on the stamp ($t_{max,stamp}$) with cell specifications. The opening width of the cells on the roller surface is 2 μm and the spacing between them is 0.5 μm. $t_{max,stamp}$ is calculated using equation (1).

Table 5.4 shows the change in the thickness of the liquid film formed on the stamp surface (t_{stamp}), as the sidewall inclination angle of the cells on the roller with a line screen of 10,160 cells/inch vary for the printing conditions described in Section 5.3 (θ_{plate}=50°, θ_{cell}=100°, H=1μm, Ca=0.01, the initial height of the liquid in the cells is 0.93 μm). In this case, since the cells do not fully evacuate during printing, t_{stamp} is calculated using the volume of the ink released from a single cell in place of V_{cell} in equation 1. As the cell sidewall angle varies between 60° and 90°, t_{stamp} varies between about 0.02 μm and 0.04 μm.

Cell Specifications		Specifications of the Liquid on Stamp	
Sidewall Angle	**Depth**	**Volume of a single drop on the stamp**	**t_{stamp}**
60°	1 μm	0.266 μm³	0.04 μm
75°	1 μm	0.168 μm³	0.03 μm
90°	1 μm	0.126 μm³	0.02 μm

Table 5.4 Change in the volume of a single drop transferred to the stamp and the thickness of the liquid film formed on the stamp (t_{stamp}) with the cell specifications, when a roller having a line screen of 10,160 cells/inch is used for ink transfer to the stamp under the conditions described in Section 5.3 (θ_{stamp}=50°, θ_{cell}=100°, H=1μm, Ca=0.01, the initial height of the liquid in the cells is 0.93 μm). The opening width of the cells on the roller surface is 2 μm and the spacing between them is 0.5 μm. t_{stamp} is calculated using equation (1) with V_{cell} replaced by the volume of the ink released from a single cell.

The liquid ink drops transferred from the cells on the ink transfer roller to the stamp surface would connect to form a film, if

$$D_{drop} \geq D_{cell} + d \tag{2a}$$

where,

$$D_{drop} = 2\left[\frac{3V_{drop}\sin^3\theta_{stamp}}{\pi(2-3\cos\theta_{stamp}+\cos^3\theta_{stamp})}\right]^{1/3} \tag{2b}$$

In equation (2), D_{drop} and V_{drop} are the diameter and the volume of a single drop released to the stamp surface from a single cell, θ_{stamp} is the contact angle on the stamp surface, D_{cell} is the cell opening width and d is the spacing between the cells. The expression for D_{drop} is obtained assuming that the drop is a spherical cap, and D_{cell} + d is equal to 2.5 μm. Based on equation 2, the drops having volumes indicated in Table 5.4 would connect on the stamp surface, when θ_{stamp} <10°. Since θ_{stamp}=50° for the results in Table 5.4, the drops on the stamp would coalesce to form a film, as the plate cylinder rotates against the impression cylinder.

During liquid transfer to the substrate, splitting of the liquid between the stamp and the substrate would reduce the thickness of the patterns printed on the substrate ($t_{substrate}$) below t_{stamp}. As an example, if the liquid on the stamp gets pinned to the edges of the stamp features during liquid transfer to the substrate, and if the substrate has a contact angle of 50°, based on the results of Test 1 in Table 4.5 of Chapter 4, about 75% of the liquid on the stamp would be transferred to the substrate at Ca=0.01. This would cause $t_{substrate}$ to vary between about 0.03 μm and 0.02 μm, as the cell sidewall inclination angle changes between 60° and 90° for printing with cells having 1 μm depth under the conditions described in Section 5.3.

When all the ink in the cells of the ink transfer roller is released to the stamp, 50° substrate contact angle and pinning of the liquid on the stamp would result in $t_{substrate}$ values between about 0.2 μm and 0.38 μm, as the cell sidewall inclination

angle changes between 60° and 90° for printing with cells having 1 μm depth at Ca=0.01.

Ink-metering rollers may not be present in certain printing systems. When these systems are used for printing, understanding the effect of the printing parameters on the behavior of the ink delivered to the substrate is important for achieving the desired print quality. For instance, Hale [4] developed an empirical process model to predict the thickness and the coverage of the patterns printed on a flat substrate using a stamp that is applied on a roller and that is inked using an ink pad. Hale showed that reducing the ink dynamic viscosity and increasing the ink surface tension coefficient increased the thickness of the printed patterns.

5.9. Advanced Rollers for Use in High-Resolution Roll-Based Printing

Novel ink-metering rollers for use in high-resolution printing can be obtained by laminating a smooth roller with materials that contain small cells on their surface. The cells may be naturally present on the surface of the laminated material as in porous materials [5, 6] and carbon nanotube arrays [7] or they may be fabricated using techniques such as electron beam drilling [8], laser beam drilling [9], focused ion beam milling [10], electrochemical and metal-assisted etching [11], and lithographic techniques [12]. Some examples of textured surfaces that could be used for stamp inking are shown in Figure 5.8.

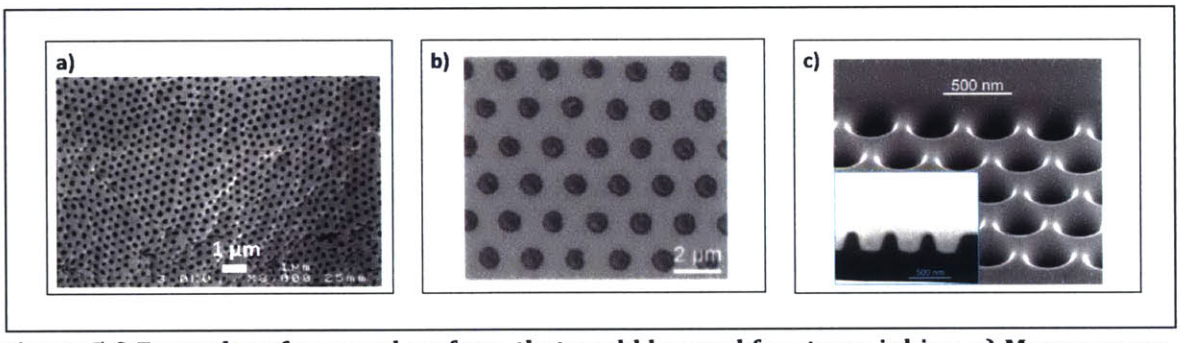

Figure 5.8 Examples of textured surfaces that could be used for stamp inking. a) Macroporous titania obtained by emulsion templating [13], b) gold nanohole array fabricated on a flexible polyethylene terephthalate (PET) substrate using wet-etching assisted colloidal lithography [14], c) hole array fabricated on a silicon substrate using focused ion beam milling (inset shows the cross section) [15].

The pores with irregular shapes on the surface of a porous material are similar to the axisymmetric cells with different sidewall inclination angles used in the simulations. As indicated by the simulation results, the cells with different sidewall inclination angles have different ink release characteristics, which affect the thickness of the printed patterns. As explained in Section 5.8, the change in the printed pattern thickness with the cell sidewall inclination angle is on the order of 10 nm for cells having 1 μm depth and 2 μm opening width under the printing conditions described in Section 5.3. If the cells are fully evacuated during printing, the variation in the printed pattern thickness with the cell sidewall inclination angle

is on the order of 100 nm. This means that materials with well-controlled surface topography should be used for inking the stamp to more precisely control the printed the layer thickness. For instance, an array of carbon nanotubes would be more preferable for inking the stamp features than porous materials containing pores with irregular shapes, especially if the printing of thick layers is desired. Moreover, the simulation results indicate that certain techniques that cannot produce the same cell geometry consistently on the roller surface, such as chemical etching to fabricate cells on a glass roller, should not be preferred during roller manufacturing. The rollers manufactured using such techniques may lead to unpredictable and variable printed pattern thickness, when implemented in high-resolution printing applications.

References

[1] S. Dodds *et. al.*, "Stretching and slipping of liquid bridges near plates and cavities", Physics of Fluids, 2009.

[2] J. A. Lee *et. al.*, "Computational study of viscoelastic effects on liquid transfer during gravure printing", Journal of Non-Newtonian Fluid Mechanics, 2013.

[3] A. K. Sankaran *et. al.*, "Effect of viscoelasticity on liquid transfer during gravure printing", Journal of Non-Newtonian Fluid Mechanics, 2012.

[4] M. Hale, "Manufacturing conductive patterns on polymeric substrates: development of a microcontact printing process", PhD Thesis, Massachusetts Institute of Technology, 2013.

[5] A. R. Studart *et. al.*, "Processing routes to macroporous ceramics: a review", Journal of the American Ceramic Society, 2006.

[6] M. E. Davis, "Ordered porous materials for emerging applications", Nature, 2002.

[7] M. Terrones, "Science and technology of the twenty-first century: synthesis, properties and applications of carbon nanotubes" Annual Review of Materials Research, 2003.

[8] A. Okada, "Electron beam machining", CIRP Encyclopedia of Production Engineering, 2016.

[9] S. Dhar *et. al.*, "A review on laser drilling and its techniques", International Conference on Advances in Mechanical Engineering, 2006.

[10] C. -S. Kim *et. al.*, "Review: developments in micro/nanoscale fabrication by focused ion beams", Vacuum, 2012.

[11] A. Santos and T. Kumeria, "Electrochemical etching methods for producing porous silicon", inside: Electrochemically Engineered Nanoporous Materials, Springer Series in Material Science, 2015.

[12] "Lithography: Principles, Processes and Materials", editor: Theodore C. Hennessey, Nova Science Publishers Inc., 2011.

[13] A. Imhof and D. J. Pine, "Ordered macroporous materials by emulsion templating", Nature, 1997.

[14] J. Wang *et. al.*, "Wet etching-assisted colloidal lithography: a general strategy toward nanohole and nanodisk arrays on arbitrary substrates", American Chemical Society Applied Materials and Interfaces, 2014.

[15] W. C. L. Hopman *et. al.*, "Focused ion beam scan routine, dwell time and dose optimizations for submicrometer period planar photonic crystal components and stamps in silicon", Nanotechnology, 2007.

Chapter 6. Summary, Conclusions and Recommendations for Future Work

6.1. Summary

In roll-based printing systems, the liquid ink passes through a series of ink transfer rollers until it reaches to the surface of a substrate from an ink reservoir. Each roller has specific functions such as metering the volume of the ink that will be printed and releasing the ink to the substrate surface in the form of specific patterns. In this study, the phase-field method is implemented to simulate the liquid ink transfer during roll-based printing.

Liquid Transfer Process

In the simulations, the transfer of liquid ink from one roller to the other is approximated as the stretching and splitting of a liquid bridge between two flat plates that separate vertically. A smooth flat plate and a flat plate containing a single cell are used to represent smooth and patterned roller surfaces, respectively. The simulations are performed in the range of dimensionless numbers that characterize the liquid ink flows in roll-based printing systems.

Development of the Phase-field Models

In the phase-field models, the interface separating the two phases is treated as physically diffuse. The position of the interface is determined by a phase-field variable whose evolution is governed by a mixing energy. In this energy-based description, the structure of the interface is rooted in molecular forces, and the tendencies for mixing and unmixing are balanced through the mixing energy. The phase-field method provides a realistic description of the liquid transfer process that is consistent with thermodynamics. Furthermore, it enables simulating flows of microstructured complex fluids easily through the treatment of the microstructural free energy together with the mixing energy.

The size and the distribution of the mesh elements inside the simulation domain, and the thickness and the mobility of the diffuse interface are identified as the main parameters of the phase-field simulations that should be chosen carefully to obtain accurate simulation results. Simulations are performed for various values and configurations of these parameters to determine the simulation conditions that yield accurate simulation results. Under selected simulation conditions, the phase-field simulation results are validated against the numerical solution presented in the literature.

Application to Roll-based Printing

The phase-field method is implemented to simulate the cell evacuation process, which enables transport of liquid ink from a patterned roll to a smooth roll, for a range of cell specifications and printing conditions. The cells used in the simulations have an opening width of 2 μm enabling printing with resolutions higher than the current industry standards. Printing guidelines that aim to improve the quality of micron-scale roll-based printing are derived from the analysis of the simulation results. Evacuation simulations of cells having variable sidewall inclination angle are used to predict how the thickness of the printed patterns would change, when cells having irregular surface topography are used for stamp inking.

Topological changes, moving and deforming interfaces, and slipping contact lines are easily handled in the simulations proving the phase-field method to be an effective tool for modeling of the liquid transport in roll-based printing systems.

6.2. Conclusions

The contributions of this study to the fields of phase-field modeling and roll-based printing are listed below.

Contributions to the Field of Phase-field Modeling

- The phase-field method is implemented to simulate the transport of liquid ink from the cells on the surface of an ink-metering roller to the surface of stamp features under various printing conditions encountered in roll-based printing.
- Phase-field modeling is shown to be an effective tool to simulate the liquid transport in roll-based printing systems that enables simulating flows with topology changes, moving and deforming interfaces, slipping contact lines and complex rheology easily, and that provides a realistic representation of the liquid behavior consistent with thermodynamics.
- Application of adaptive mesh refinement on a dynamic mesh that deforms with the motion of the simulation domain boundaries is shown to be effective to resolve the interface with reduced computational cost in phase-field simulations of two-phase flow.
- Identification of the sections of the simulation domain that are swept by the interface, and the use of finer mesh elements in these sections is shown to be effective to resolve the interface with reduced computational cost in phase-field simulations of two-phase flow.
- Simulation results are shown to yield accurate results over a range of mobility tuning parameter values.
- Simulation results are shown to reach their sharp interface limit, as the thickness of the interface is reduced keeping the mobility tuning parameter constant.

Contributions to the Field of Roll-based Printing

For the cell specifications and printing conditions investigated:

- The quantity of ink removed from the cells on the surface of the ink transfer rollers is reduced, as the cell sidewalls are made steeper.
- The quantity of ink removed from the cells on the surface of the ink transfer rollers does not change, as the cell depth is increased above a certain value.
- The quantity of ink removed from the cells on the surface of the ink transfer rollers increases, as the cell surface wettability is reduced, plate surface wettability is increased, printing speed is increased and inks with higher dynamic viscosity and lower surface tension coefficient are used.
- Cells having smaller depth and smaller sidewall inclination angle should be used during high-resolution roll-based printing to minimize cell clogging.
- The adjustment of the cell specifications and the printing conditions based on the above criteria would enable releasing the desired quantity of ink during high-resolution roll-based printing and improve the quality of the prints obtained.
- Variations in the geometry of the cells having dimensions on the order of 1 μm can lead to changes in the printed layer thickness on the order of 100 nm. Hence, variations in the cell geometry should be minimized, while developing new materials or new roller designs for use in stamp inking, especially for printing of thick layers.

6.3. Recommendations for Future Work

The liquid transfer simulations based on the phase-field method presented in this study can be further developed by taking into consideration the below points.

Motion of the separating surfaces: The roller surfaces are approximated as flat plates that move vertically with constant velocity in the phase-field simulations presented in this thesis. Sinusoidal velocity and acceleration profiles can be assigned to the flat plates in both the horizontal and vertical directions to better represent the rotational motion of the roller surfaces. This would require three dimensional liquid transfer simulations, instead of axisymmetric.

Ink rheology: The inks used in roll-based printing may contain pigments, conductive particles, surfactants and stabilizing agents that could result in non-Newtonian ink behavior. The non-Newtonian ink rheology can be taken into account in the future simulations.

Permeability of the separating surfaces: Stamp and substrate materials used in roll-based printing may have permeable surfaces. Porous media flows into the separating surfaces can be included in the future simulations.

Electric and magnetic forces: Electric and magnetic forces can be used to aid cell evacuation. Effect of these forces on the amount of ink removed from the cells can be investigated in the future simulations.

Three-dimensional simulations: These would enable simulating liquid transport through non-circular liquid bridges. The results obtained would be useful to determine the suitable printing conditions for non-circular device components.

Deformation of the stamp and the substrate: The roller surfaces are modeled as rigid flat plates that are initially separated by a specified distance in the phase-field simulations. The deformation of the stamp as the ink-metering roller rotates against the plate cylinder, and the deformation of the substrate as it moves from one roll to the other can also be simulated. Then the deformation simulations can be coupled with the ink transfer simulations. Preliminary simulation results are presented in Appendix A.

Initial volume of the ink inside the cells: The initial ink volume inside the cells having different geometries yields the same ink height, when all the ink rests in the cells with a flat free-surface in the phase-field simulations presented in this study. In reality, the ink level in the cells after blading would depend on the positioning and the properties of the blade, the specifications of the cells and the properties of the ink, as described in Appendix F. Additional simulations can be performed to determine the volume of the ink remaining inside the cells after blading.

Calculation of the fraction of the ink transferred from one roller surface to the other using different methods: Young-Laplace equation can be solved or analytical expressions can be developed to calculate the fraction of the ink transferred from one roller surface to the other. The results obtained can be compared with the phase-field simulation results.

Pore-network modeling of liquid transport: In next-generation roll-based printing systems with high-resolution printing capabilities, porous materials may be used for stamp inking. Since the pores on such materials are connected to each other, the pores would refill, as they release ink to the stamp surface. Instead of modeling the ink transport from individual cells to stamp features, pore network models that take into account the ink flow between the pores can be developed to assess the applicability of porous materials to stamp inking.

6.4. Broader Perspectives

This study intends to open a path for future phase-field simulations for the advancement of the roll-based printing technologies. Some of the future application areas of the phase-field simulations in the roll-based printing field are design of cells that can print patterns having desired thickness with sub-micron resolution; investigation of printing with new ink formulations; exploration of ink behavior over substrates having various surface topographies; and development of novel

stamp designs that eliminate printing defects. The resulting improvements in roll-based printing systems are expected to enable the printing of devices that have higher performance.

Appendix

A. Deformation of Stamp Features with Slanted Walls during Microcontact Printing

A.1. Introduction

Microcontact printing (μCP) is a subset of soft lithography. μCP uses an elastic polydimethylsiloxane (PDMS) stamp to form patterns of monolayers or thin liquid films on the surface of a substrate through selective mechanical contact (Figure A.1). Its applications are wide ranging including formation of etch resists at the scales of about 100 nm to be used for surface micromachining, and patterning of proteins, cells and DNA for use in cell biology and tissue engineering research.

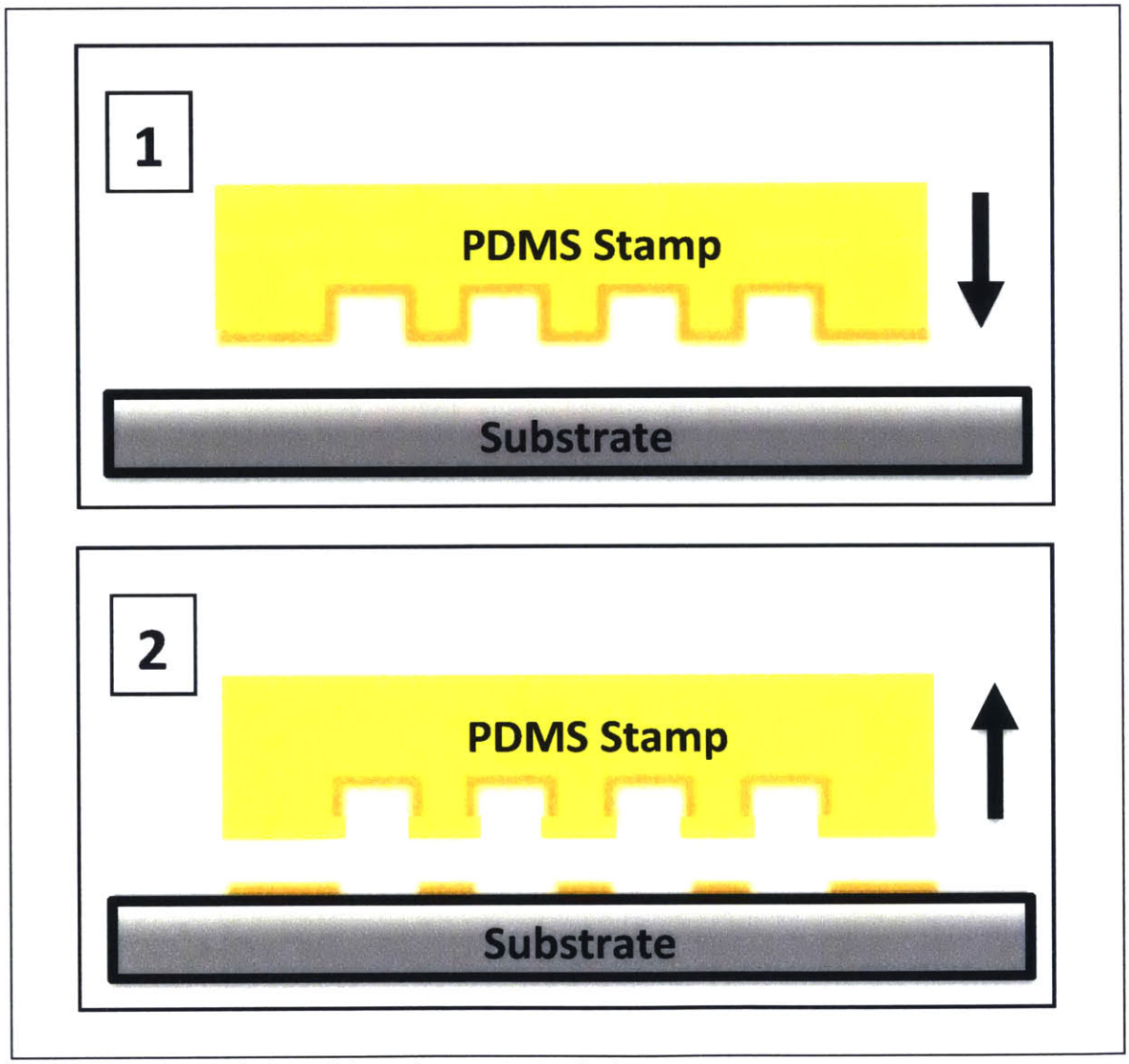

Figure A.1 Schematic describing microcontact printing.

Although the low shear modulus of the PDMS stamps allow conformal contact of its features to the substrate, it also leads to undesired stamp deformations resulting in erroneous prints at modest application pressures (Figure A.2).

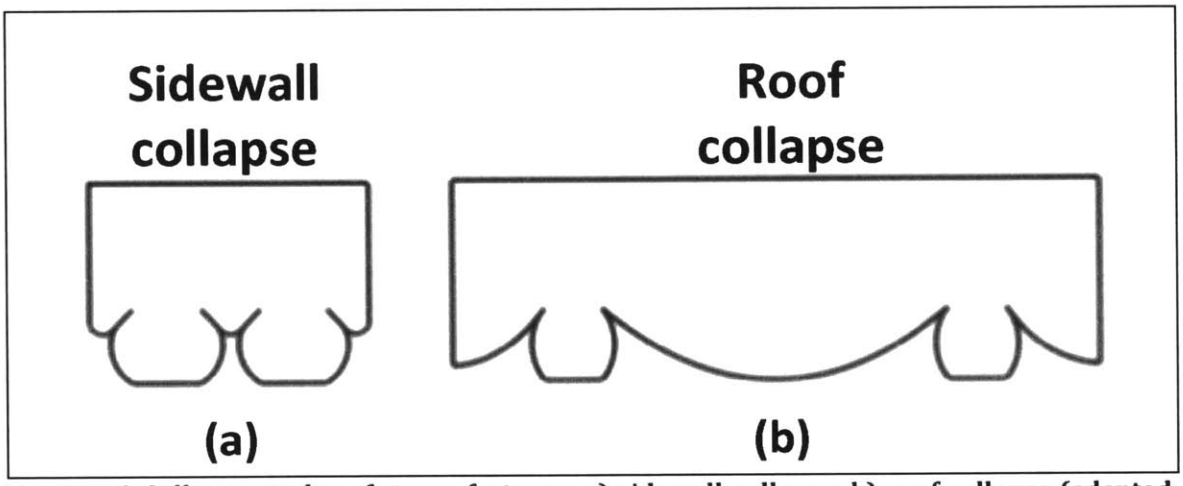

Figure A.2 Collapse modes of stamp features: a) sidewall collapse, b) roof collapse (adapted from [1]).

Hence, studies are conducted to investigate load-displacement-stiffness behavior of the stamp features, identify collapse modes of the stamp and determine critical pressures leading to them. All these existing studies are limited to stamp features with straight walls [1-7].

However, recent work by Nietner [8] has shown the ability to create stamp features with controllable sidewall angles (Figure A.3). The process used in this work involves centrifugal-casting a photoresist inside a rotating drum, patterning of the photoresist layer with a laser beam to obtain a mold, and casting PDMS into the mold to produce the stamp. Variations in width and sidewall angle of the stamp features could be obtained by varying the laser exposure time during patterning of the photoresist layer.

The objective of this work is to investigate how stamps containing features with slanted walls behave under loading. Pressure values leading to roof collapse are determined for various sidewall slant angle and spacing values of the stamp features.

Simulation results predict that stamps with slanted-walled features show greater resistance to roof collapse compared to those with straight-walled features. Collapse pressure is found to increase with increasing sidewall slant angle and decreasing feature spacing.

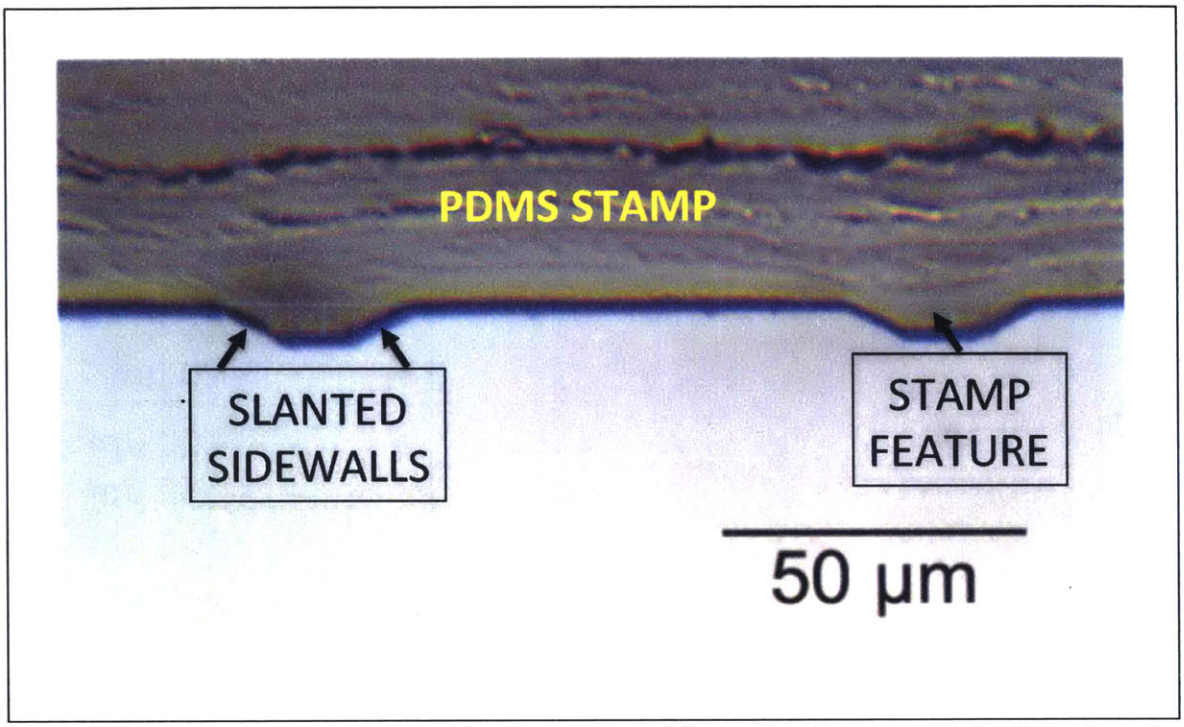

Figure A.3 Cross section of a PDMS stamp containing microfeatures with slanted walls (adapted from [8]).

A.2. Method of Approach

Roof collapse occurs when the center of the stamp roof (point C in Figure A.4) touches the rigid support under loading (Figure A.2b). Simulations are performed to predict roof collapse pressure for stamps having dimensions inside the range of experimentally achievable values.

Stamp dimensions used in the simulations are shown in Figure A.4. Spacing and sidewall slant angle of the stamp features are varied from 100 μm to 400 μm, and from 90° to 150°, respectively. Default thickness value of 1 m is used in all the simulations. A fillet with a radius of 3 μm is used at the corner of the stamp feature where it touches the rigid support.

The structural mechanics module of COMSOL software is used for the simulations, which are setup with the boundary and initial conditions shown in Figure A.5. The displacement is prescribed at the top stamp boundary (labeled with "5" in Figure A.5) and is increased in increments of 1 μm, until the center of the stamp roof (point C in Figure A.4) is displaced by 10 μm in the negative y direction (moment of roof collapse).

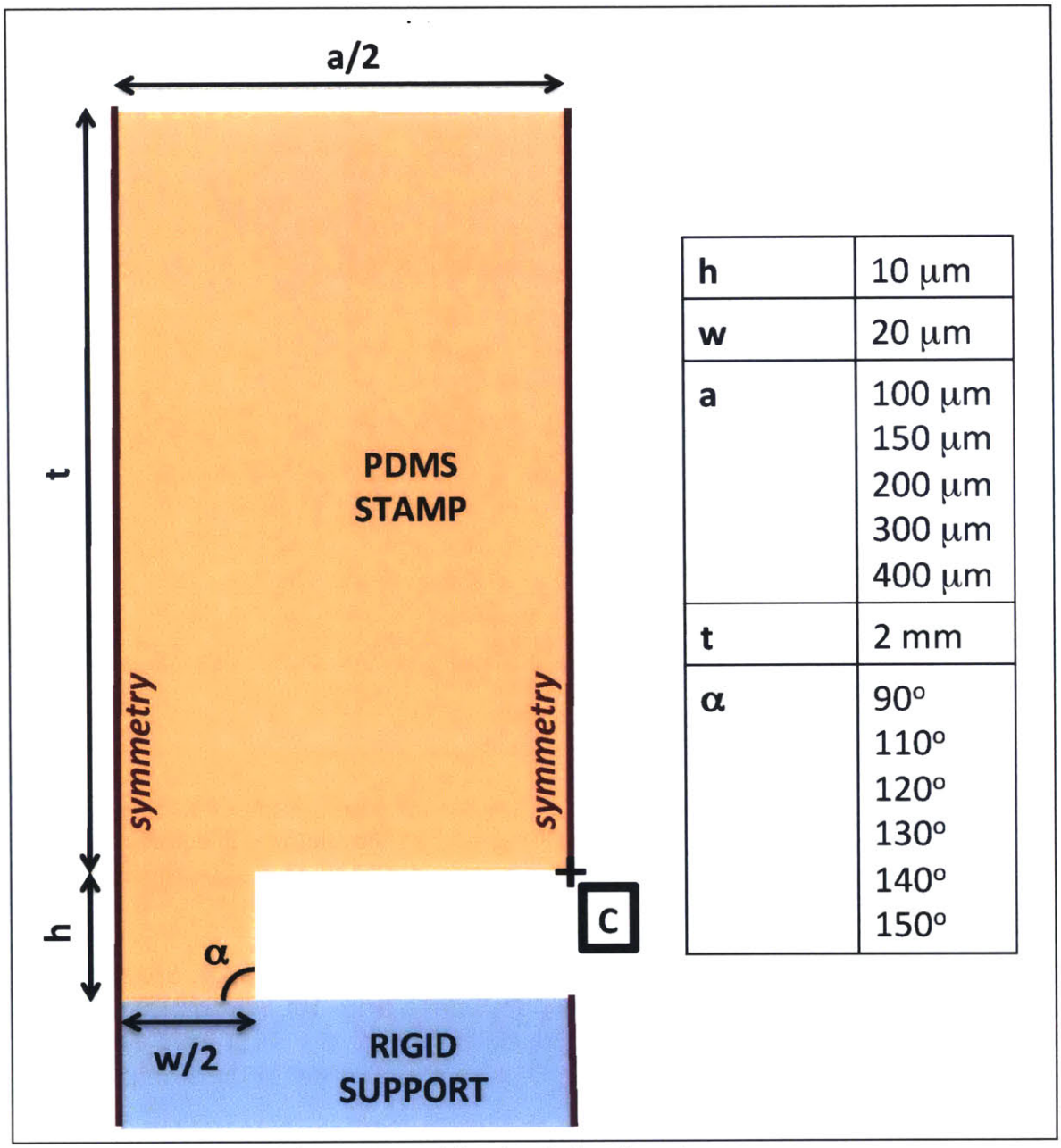

h	10 μm
w	20 μm
a	100 μm 150 μm 200 μm 300 μm 400 μm
t	2 mm
α	90° 110° 120° 130° 140° 150°

Figure A.4 Geometry and dimensions of the simulation domain.

Displacement of the top stamp boundary is expressed as a boundary load by calculating the traction on this boundary. Plain strain is chosen as the 2D approximation. PDMS is defined as a hyperelastic material using the Neo-Hookean material model in the nonlinear structural materials module of COMSOL software with the parameters given in Table A.1.

A free triangular mesh is used for the simulations and element size is chosen to be extremely fine for all the simulations, except two of them. For stamp features with 40° sidewall slant angle and 100 μm spacing, an extra fine mesh is used. For stamp features with 60° sidewall slant angle and 100 μm spacing a custom mesh was

necessary with maximum element size of 7 μm, minimum element size of 0.01 μm, maximum element growth rate of 1.01, curvature factor of 0.15, and resolution of narrow regions being 1. A mesh refinement study is performed to ensure that mesh element size is sufficiently small in the simulations.

Domain, Boundary, Point	Condition
1	Hyperelastic material - Initial displacement=0 - Initial velocity=0
2	Fixed constraint - Initial displacement=0 - Initial velocity=0
(10):(6, 7, 8, 9)	Contact couple 1 (zero friction coefficient)
(8):(9,7)	Contact couple 2 (zero friction coefficient)
3, 4	Symmetry
5	Prescribed displacement (displaced in negative y direction with 1 micron increments till roof collapse occurs)
6, 7, 8, 9, 10, 11	Free
B	Fixed constraint
A	Prescribed displacement - x-displacement=0 - y-displacement=unspecified

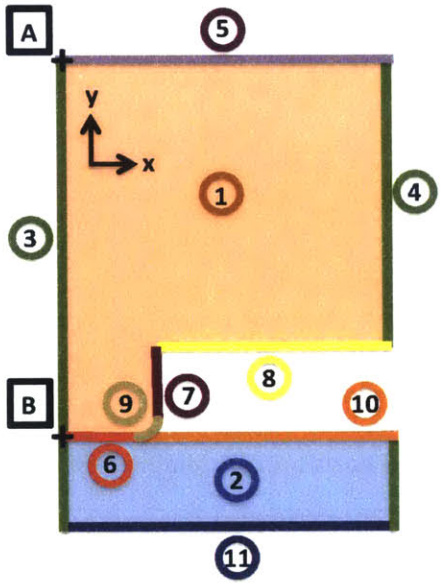

Figure A.5 Simulation setup with boundary and initial conditions.

Density	**970 kg/m³**
Lame parameter λ	**6.93 GPa**
Lame parameter m	**0.77 GPa**
Poisson's ratio	**0.43**

Table A.1 Material properties of PDMS used in the simulations.

A.3. Results and Discussion

Simulation results indicate that as the sidewall slant angle of the stamp features is increased, the critical pressure required for roof collapse increases for all feature spacing values (Figure A.6). As expected, as feature spacing is increased, the critical pressure required for roof collapse decreases (Figure A.7). However, it is observed that even at large spacings the angled side continues to increase collapse pressure threshold. The results also indicate that pressure required for roof collapse is not affected by feature spacing for spacing values above about 300 μm.

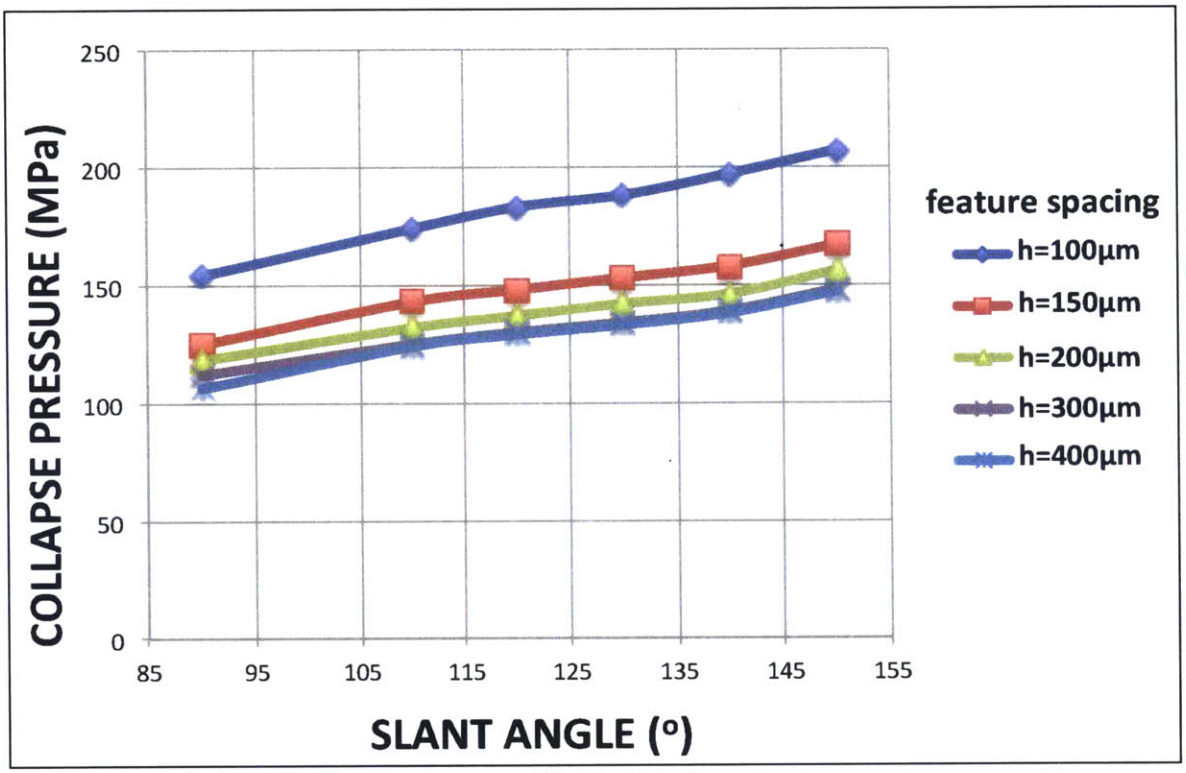

Figure A.6 Variation of collapse pressure with slant angle.

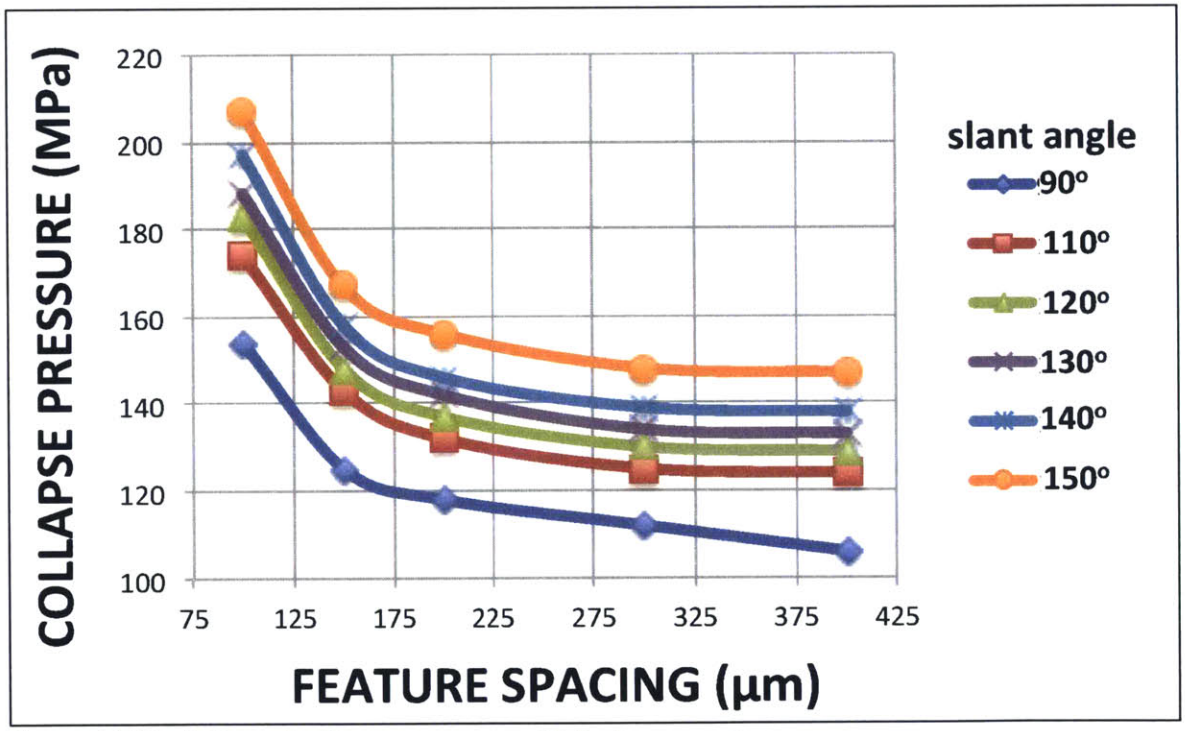

Figure A.7 Variation of collapse pressure with feature spacing.

Since the angled sidewalls increase the collapse pressure, stamps with these features should be more tolerant of pressure variations over their area. In this way, we can conclude that angled walls improve the process robustness for microcontact

printing. However, the effect of these angles on quality of ink transfer has yet to be assessed.

References

1. J. E. Petrzelka and D. E. Hardt, "Static load-displacement behavior of PDMS microfeatures for soft lithography", Journal of Micromechanics and Microengineering, 2012.
2. A. Bietsch and B. Michel, "Conformal contact and pattern stability of stamps used for soft lithography", Journal of Applied Physics, 2000.
3. C. Y. Hui *et. al.*, "Constraints on microcontact printing imposed by stamp deformation", Langmuir, 2002.
4. K. G. Sharp *et. al.*, "Effect of stamp deformation on the quality of microcontact printing: theory and experiment", Langmuir, 2004.
5. N. J. Glassmaker *et. al.*, "Design of biomimetic fibrillar interfaces: 1. Making contact", Journal of the Royal Society Interface, 2004.
6. C. Y. Hui *et. al.*, "Design of biomimetic fibrillar interfaces: 2. Mechanics of enhanced adhesion", Journal of the Royal Society Interface, 2004.
7. P. Roca-Cusachs *et. al.*, "Stability of microfabricated high aspect ratio structures in poly(dimethylsiloxane), Langmuir, 2005.
8. L. Nietner, "A Direct-Write Thick-Film Lithography Process for Multi-Parameter Control of Tooling in Continuous Roll-to-Roll Microcontact Printing", MS Thesis, Massachusetts Institute of Technology, 2014.

B. Phase-field Simulations of Liquid Splitting Between a Rotating Cylinder and an Inclined Slide

B.1. Description of the Simulation Setting

Splitting of a liquid drop resting on a flat inclined slide, as an initially stationary cylinder placed on it starts rolling due to gravity, is simulated. The cylinder rolls over spacers placed along the two edges of the inclined slide. This creates a gap between the cylinder surface and the inclined slide surface with height equal to the thickness of the spacers. Trajectory of the point on the surface of the rotating cylinder, which is initially in contact with the drop, is a cycloid described by

$$x = R \cdot (\theta - \sin\theta) \quad (1)$$
$$y = R \cdot (1 - \cos\theta) \quad (2)$$

In equations (1) and (2), θ represents the angle of rotation of the cylinder, R is the cylinder radius and the center of the cylinder is located at (x=R.θ, y=R). Velocity of the cycloid can be calculated in terms of the initial angle of rotation (θ_0), initial angular velocity (ω_0) and angular acceleration (α) of the cylinder as,

$$V_x = \frac{dx}{dt} = R_{roller} \cdot (\omega_0 + \alpha \cdot t) \cdot \left[1 - \cos\left(\theta_0 + \omega_0 \cdot t + \frac{1}{2} \cdot \alpha \cdot t^2\right)\right] \quad (3)$$
$$V_y = \frac{dy}{dt} = R_{roller} \cdot (\omega_0 + \alpha \cdot t) \cdot \sin\left(\theta_0 + \omega_0 \cdot t + \frac{1}{2} \cdot \alpha \cdot t^2\right) \quad (4)$$

For a cylinder rolling down an inclined plane with an angle of inclination of β,

$$\alpha = \frac{2}{3} \cdot \frac{g}{R} \cdot \sin(\beta) \quad (5)$$

For R=0.02 m, β=1.5°, θ_0=0 rad, ω_0=0 rad/sec, equations 3, 4 and 5 yield

$$\alpha = 8.559\ rad/sec^2 \quad (6)$$
$$v_x = 0.171 \cdot t \cdot [1 - \cos(4.279 \cdot t^2)]\ m/sec \quad (7)$$
$$v_y = 0.171 \cdot t \cdot \sin(4.279 \cdot t^2)\ m/sec \quad (8)$$

Splitting of the liquid drop between the rotating cylinder and the inclined slide is simulated as the splitting of a liquid drop trapped between two flat plates, as the flat plates separate (the simulations are similar to those described in Chapter 4, but the contact lines are allowed to move on both plates). The liquid drop is allowed to reach its equilibrium shape, before the upper plate is set into motion at t=0 sec. Since $v_y >> v_x$ for the first 0.3 sec of roller motion (~ 20° of rotation), v_x is ignored in the simulations. Vertical component of the velocity of the point on the cylinder surface, which is in touch with the drop (given by equation 8), is used as the upper plate velocity. The simulations are axisymmetric with details as shown in Table B.1.

Liquid contact angles on the upper and lower plates	$\theta_{upper\text{-}moving}=58^o$ $\theta_{lower\text{-}stationary}=60^o$
Material properties	$\rho_{water}=998$ kg/m^3, $\mu_{water}=9.77x10^{-4}$ Pa.sec $\rho_{air}=1.2$ kg/m^3, $\mu_{air}=1.82x10^{-5}$ Pa.sec $\sigma=0.0725$ N/m
Upper plate velocity	$v_y=0.171t\sin(4.279t^2)$ m/sec
Volume of the liquid drop	1.5 μLt
Initial spacing between the plates	$540x10^{-6}$ m

Table B.1 Details of the axisymmetric liquid splitting simulations.

B.2. Simulation Results

A segmented uniform mesh is used in the simulations, as in the simulations described in Chapter 4. For a specified interface thickness and a fixed air mesh element size (Δh_{air}) of 70 μm, simulation results do not change, as liquid mesh element size (Δh_{liquid}) is reduced below about 20 μm (Table B.2). As ε is reduced (keeping $\Delta h_{liquid}=\varepsilon/2$ to resolve the interface), fraction of liquid transferred to the moving surface approaches to about 22% (Table B.3).

Test	Liquid mesh size	ε	Result
1	5 μm	30 μm	$t_{split}=0.49$ sec ,T.R.=0.234
2	10 μm	30 μm	$t_{split}=0.49$ sec ,T.R.=0.233
3	15 μm	30 μm	$t_{split}=0.49$ sec ,T.R.=0.234
4	10 μm	50 μm	$t_{split}=0.49$ sec ,T.R.=0.252
5	15 μm	50 μm	$t_{split}=0.49$ sec ,T.R.=0.251
6	20 μm	50 μm	$t_{split}=0.49$ sec ,T.R.=0.253
7	25 μm	50 μm	$t_{split}=0.49$ sec ,T.R.=0.255

Table B.2 Results of simulations with different Δh_{liquid}. Δh_{air} is 70 μm, $\Delta h_{liquid} \leq 0.5\varepsilon$ to ensure that the interface is well-resolved and χ is 1 m.s/kg in each simulation. In Tests 1-3, Δh_{liquid} is reduced below 15 μm, as ε is fixed at 30 μm. In Tests 4-7, Δh_{liquid} is reduced below 25 μm, as ε is fixed at 50 μm.

Test	Liquid mesh size	ε	Result
1	5 μm	10 μm	$t_{split}=0.49$ sec ,T.R.=0.225
2	10 μm	20 μm	$t_{split}=0.49$ sec ,T.R.=0.228
3	20 μm	40 μm	$t_{split}=0.49$ sec ,T.R.=0.246
4	25 μm	50 μm	$t_{split}=0.49$ sec ,T.R.=0.255

Table B.3 Simulation results for different values of ε. Δh_{air} is 70 μm, Δh_{liquid} is 0.5ε to ensure the interface is well-resolved, and χ is 1 m.s/kg in each simulation.

It is concluded that $\Delta h_{liquid}=10\mu m$, $\Delta h_{air}=70\mu m$, $\varepsilon=20\mu m$, $\chi=\gamma/\varepsilon^2=1$ m.s/kg are suitable for use in the liquid splitting simulations, since the results are independent of mesh element size and interface thickness for this combination of simulation parameters. In simulations having $\theta_{upper\text{-}moving}=90^o\text{-}110^o$ and $\theta_{bottom\text{-}stationary}=70^o$, fraction of liquid transferred to the upper plate is found to be below 1%.

C. Two-Dimensional Symmetric Liquid Splitting Simulations

Splitting of two-dimensional symmetric liquid bridges between separating flat plates is simulated using the phase-field method. The simulations are similar to those described in Chapter 4, but the contact lines are free to move on both the lower and upper plates. Simulation setting is described in Table C.1. A segmented uniform mesh is used in the simulations. Mesh element size in the liquid region (Δh_{liq}) is set to be smaller than the mesh element size in the air region (Δh_{air}) to resolve the interface. When the contact angle of the upper plate is reduced below 45°, unphysical contact line behavior is observed in the simulation results. In these cases, very fine mesh elements are used in the region along the upper wall that the contact lines move through. A mesh refinement study is performed to ensure that the mesh elements are sufficiently small. Simulation results are validated against the numerical solution presented in [1] (Table C.2). Sample simulation results are shown in Figure C.1.

Initial contact line width	4 μm
Initial distance between flat plates	8 μm
Width of the flat plates	20 μm
Volume of the liquid	32 μm^2 (initially liquid is a rectangle)
Velocity of the upper plate (u_w)	0.1 m/s (plate motion begins after the liquid reaches its equilibrium shape)
Material properties	ρ_{ink}=1000 kg/m^3, μ_{ink}=0.1 Pa.sec, ρ_{air}=1.16 kg/m^3, μ_{air}=1.81x10^{-5} Pa.sec σ=1 N/m
Contact angles	Both contact lines are free to move with θ_{bottom}=60° and θ_{top}=30°-60°
Dimensionless numbers characterizing liquid ink flow	Re=0.002 Ca=0.01 Bo=0 (gravitational effects neglected)

Table C.1 Details of the two-dimensional liquid splitting simulations.

Simulation cases	Transfer Ratio	
	Huang *et. al.* [1]	Phase-field
θ_{bottom}=60° θ_{top}=60°	0.5	0.5
θ_{bottom}=60° θ_{top}=45°	0.7	0.66
θ_{bottom}=60° θ_{top}=30°	0.8	0.75

Table C.2 Comparison of liquid transfer ratio values reported in [1] and obtained from the phase-field model. There is close match between the results (less than 7% difference) for each simulation case. Simulation parameters are ε=0.125 μm, χ=1 m.s/kg, Δh_{liq}=0.083 μm, Δh_{air}=0.536 μm. In the simulation with θ_{top}=30°, size of mesh elements in the region along the upper plate that the contact line moves through is 0.05 μm.

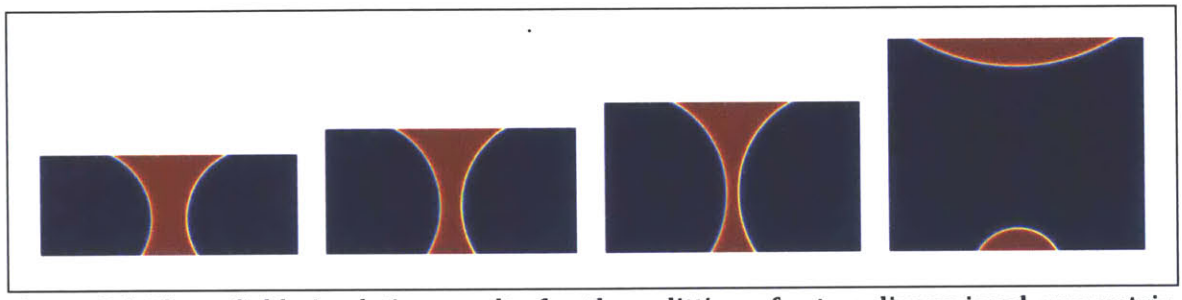

Figure C.1 Phase-field simulation results for the splitting of a two-dimensional symmetric liquid bridge. Details of the simulation are as described in Table C.1 with $\theta_{top}=30^o$, $\theta_{bottom}=60^o$, $\Delta h_{liq}=0.083$ μm, $\Delta h_{air}=0.536$ μm, $\Delta h_{contact\text{-}line}=0.05$ μm, $\varepsilon=0.125$ μm and $\chi=1$ m.s/kg. The first frame shows the liquid ink in its equilibrium state at the beginning of plate motion. Time interval between the first three frames is 20 μsec and the time interval between the last two frames is 50 μsec. Red indicates liquid and blue indicates air.

After the liquid splits, the drops on the upper and lower plates exchange mass through diffusion to minimize the total free energy of the system. As a result, the drop on the upper plate grows and the drop on the lower plate shrinks over time. Mass exchange between the drops slows down, when the mobility tuning parameter and the capillary width are reduced (Figure C.2).

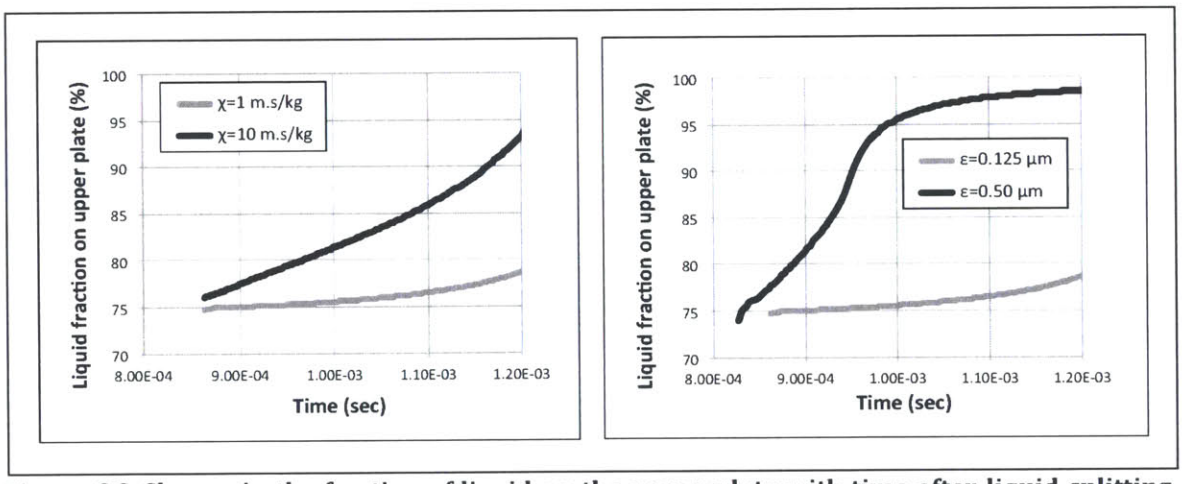

Figure C.2 Change in the fraction of liquid on the upper plate with time after liquid splitting due to mass exchange between the drops on the upper and lower plates by diffusion. a) $\varepsilon=0.125$ μm and χ is varied, b) $\chi=1$ m.s/kg and ε is varied. In the simulations, $\theta_{top}=30^o$, $\theta_{bottom}=60^o$, $\Delta h_{liq}=0.083$ μm, $\Delta h_{air}=0.536$ μm, $\Delta h_{contact\text{-}line}=0.05$ μm.

References

[1] W. -X. Huang *et. al.*, "Simulation of liquid transfer between separating walls for modeling micro-gravure-offset printing", International Journal of Heat and Fluid Flow, 2008.

D. Some Experimental Systems for Studying Splitting Liquid Bridges

In this section, some experimental systems that can be used to investigate splitting liquid bridges are analyzed.

D.1. Determination of the Velocity and the Acceleration of the Separating Surfaces

The liquid transport from the anilox roller to the plate cylinder can be approximated as the splitting of a liquid drop between two vertically separating flat plates in simplified laboratory experiments. The range for the plate separation velocity (v_{sep}) and acceleration (a_{sep}) that should be used in these experiments is calculated below for a liquid drop having dimensions around 5 μm.

For a cylinder rotating with constant angular velocity, tangential velocity and centripetal acceleration on the cylinder surface are given by

$$\boldsymbol{v_{roller}} = v_{roller} \cdot [cos(\omega_{roller} \cdot t)\boldsymbol{i} + sin(\omega_{roller} \cdot t)\boldsymbol{j}] \quad (1)$$

$$\boldsymbol{a_{roller}} = \frac{v_{roller}^2}{R_{roller}} \cdot [-sin(\omega_{roller} \cdot t)\boldsymbol{i} + cos(\omega_{roller} \cdot t)\boldsymbol{j}] \quad (2)$$

Assuming angle of rotation of the cylinder ($\theta_{roller} = \omega_{roller}.t = (v_{roller}/R_{roller}).t$) to be small, components of v^{roller} and a^{roller} in the **j** direction are

$$\boldsymbol{v_{roller}} = \frac{v_{roller}^2}{R_{roller}} \cdot t\,\boldsymbol{j} \quad (3)$$

$$\boldsymbol{a_{roller}} = \frac{v_{roller}^2}{R_{roller}}\boldsymbol{j} \quad (4)$$

Under the following assumptions,

- the anilox roller and the plate cylinder have equal diameter and speed,
- the fraction of liquid transferred from one plate to the other is the same, when the two plates move in opposite directions and when one plate is stationary and the other plate moves twice as fast (quasistatic process),
- the liquid splits with a small angle of rotation of the two rollers,

velocity ($\mathbf{v_{sep}}$) and acceleration ($\mathbf{a_{sep}}$) of separation of the flat plates that should be achieved in the experiments can be calculated as,

$$\boldsymbol{v_{sep}} = \frac{2 \cdot v_{roller}^2}{R_{roller}} \cdot t\,\boldsymbol{j} \quad (5)$$

$$\boldsymbol{a_{sep}} = \frac{2 \cdot v_{roller}^2}{R_{roller}}\boldsymbol{j} \quad (6)$$

For the approximate range of printing parameters given in Table D.1, speed and acceleration of separation of the flat plates can be calculated to be in the following range:

$$70 \cdot t < v_{sep}[\frac{m}{sec}] < 15{,}750 \cdot t \quad (7)$$

$$70 < a_{sep}[\frac{m}{sec^2}] < 15{,}750 \quad (8)$$

If the liquid bridge splits at a height of Δh and if a_{sep} is a constant, time required for the liquid to split (t_{split}), maximum plate separation velocity at the moment of liquid splitting ($v_{max,split}$) and time-averaged plate separation velocity until liquid splitting (v_{avg}) can be calculated as

$$t_{split} = \sqrt{\frac{2 \cdot \Delta h}{a_{sep}}} \quad (9)$$

$$v_{max,split} = \sqrt{2 \cdot \Delta h \cdot a_{sep}} \quad (10)$$

$$v_{avg} = \frac{\sqrt{2 \cdot \Delta h \cdot a_{sep}}}{2} \quad (11)$$

If the liquid bridge splits at a height of $\Delta h = 10\mu m$, then

$$0.03 \text{ msec} < t_{split,\,\Delta h=10\mu m} < 0.5 \text{ msec} \quad (12)$$

$$0.037 \text{ m/sec} < v_{max.,\,\Delta h=10\mu m} < 0.56 \text{ m/sec} \quad (13)$$

$$0.018 \text{ m/sec} < v_{avg.,\,\Delta h=10\mu m} < 0.25 \text{ m/sec} \quad (14)$$

Equation 12 indicates the range of experimental time scales, and equations 13-14 indicate the range of plate separation velocities that can be used in the liquid splitting experiments.

	Min	Max
V_{roller}	3 m/sec	10 m/sec
R_{roller}	0.0127 m	0.254 m

Table D.1 Approximate range of roller sizes, and speeds used in flexographic printing. V_{roller} range is for commercial printing from [1]. R_{roller} values are based on information received from Harper Corporation.

Static Rayleigh-Plateau limit states that a cylinder of static liquid with its height greater than its circumference ($H/R>2\pi$) is unstable. Assuming this holds for a stretching liquid bridge, a bridge with $r_{initial}=a$, $h_{initial}=2a$, $V_{initial}=2\pi a^3$ will break, when $r_{final}=0.68a$, $h_{final}=4.28a$, $V_{final}=2\pi a^3$ during the stretching process. This implies that the liquid will break, when its height reaches about 2 times its initial value. Hence, for experiments involving liquid drops with sizes around 5 μm, $\Delta h_{liquid} \approx 10$ μm is reasonable.

D.2. Use of a Rotating Beam to Study Splitting Liquid Bridges

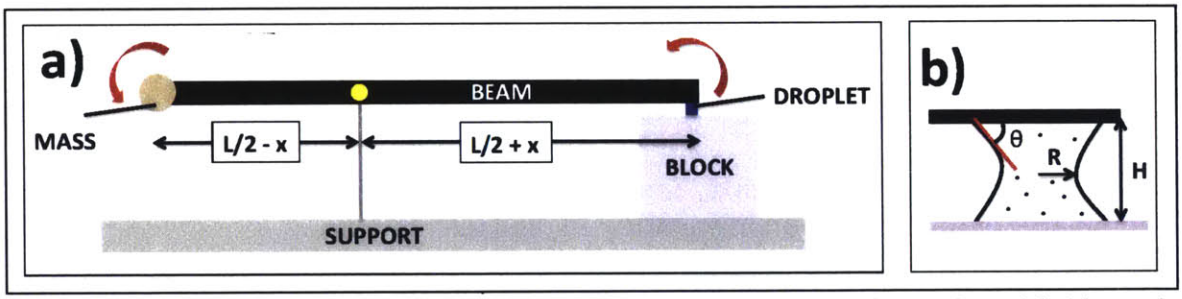

Figure D.1 Schematic of a rotating beam that can be used to study splitting liquid bridges. a) Components of the experimental setup (L indicates the beam length, and x indicates the distance between the beam center of mass and the beam axis of rotation). b) Close-up view of the liquid drop trapped between the block and the beam.

The rotating beam shown in Figure D.1 can be used for the liquid splitting experiments. Beam length (L), the distance between the beam center of mass and beam axis of rotation (x) and the mass of the object attached to the left end of the beam (M_{mass}) are the experimental parameters that should be determined to reach specific v_{sep} and a_{sep} values. These parameters can be calculated using Newton' s second law for rotation:

$$\sum\tau = I \cdot \propto \tag{15}$$

Here τ is the net torque, I is the mass moment of inertia and α is the angular acceleration. For the system shown in Figure D.1,

$$\sum\tau = I \cdot \propto = M_{mass} \cdot g \cdot \left(\frac{L}{2} - x\right) - F_{liquid} \cdot \left(\frac{L}{2} + x\right) - M_{beam} \cdot g \cdot x \tag{16}$$

$$I = \left(\frac{1}{12} \cdot M_{beam} \cdot L^2 + M_{beam} \cdot x^2\right) + M_{mass} \cdot \left(\frac{L}{2} - x\right)^2 + M_{liquid} \cdot \left(\frac{L}{2} + x\right)^2 \tag{17}$$

$$a_{sep} = \left(\frac{L}{2} + x\right) \cdot \propto \tag{18}$$

Laplace pressure difference between the air and the liquid on the right side of the beam can be calculated for a stationary capillary bridge (at the beginning of the experiments) as:

$$\Delta P = \gamma \left(\frac{1}{R} - \frac{\cos(\theta)}{H/2}\right) \tag{19}$$

Hence, the force (F_{liquid}) required to separate the block and the beam is:

$$F_{liquid} = \Delta P \cdot \pi R^2 = \gamma \left(\frac{1}{R} - \frac{\cos(\theta)}{H/2}\right) \cdot \pi R^2 \tag{20}$$

F_{liquid} would be attractive for $0^o<\theta<90^o$ and maximized for $\theta=90^o$.

Using equations (15-20) with the maximum value of F_{liquid} at the beginning of the experiment, acceleration of the right tip of the beam can be calculated as:

$$a_{sep} = \left(\frac{L}{2} + x\right) \cdot \frac{M_{mass} \cdot g \cdot \left(\frac{L}{2} - x\right) - F_{liquid,max} \cdot \left(\frac{L}{2} + x\right) - M_{beam} \cdot g \cdot x}{\left(\frac{1}{12} \cdot M_{beam} \cdot L^2 + M_{beam} \cdot x^2\right) + M_{mass} \cdot \left(\frac{L}{2} - x\right)^2 + M_{liquid} \cdot \left(\frac{L}{2} + x\right)^2} \quad (21)$$

Use of an object with finite size, instead of a point mass, would increase the denominator of the expression in equation 21, and decrease a_{sep}.

For negligible M_{beam} and F_{liquid}, acceleration of the right tip of the beam would be:

$$a_{sep} \approx g \cdot \frac{L + 2 \cdot x}{L - 2 \cdot x} \quad (22)$$

For rotation of the beam around its center of mass (x=0), equation (22) would reduce to:

$$a_{sep} \approx g \quad (23)$$

Equation (22) indicates that $a_{sep} > g$ for $x > 0$, and a_{sep} increases with increasing x and L. As $x \rightarrow L/2$, $a_{sep} \rightarrow \infty$ for negligible M_{beam} and F_{liquid}.

When equation (21) is plotted for experimentally feasible parameter values, the acceleration of the right tip of the beam is found to increase with x and M_{mass}. Furthermore, a_{sep} is calculated to be less than about 250 m/sec^2 under these conditions. This corresponds to a maximum value of about 0.03 m/sec for $v_{sep,avg}$. The low value of a_{sep} and the requirement of large M_{mass} to increase it are due to the finite mass of the beam.

D.3. Use of a Cantilever Beam to Study Splitting Liquid Bridges

A cantilever beam can be bent by applying a force to its free end to get its tip in contact with a liquid drop and then suddenly released leading to liquid splitting (Figure D.2). The displacement of a point on the cantilever beam as a function of time can be calculated by solving the linear Euler-Bernoulli equation as,

$$q(x,t) = \sum_{n=1}^{\infty} X_n(x)\, f_n(t) \quad (24)$$

In equation (24),

$$X_n(x) = \frac{1}{2}\left[\cos(k_n x) - \cosh(k_n x) - \left(\frac{\cos(k_n L) + \cosh(k_n L)}{\sin(k_n L) + \sinh(k_n L)}\right)(\sin(k_n x) - \sinh(k_n x))\right] \quad (25)$$

$$f_n(t) = A_n \cos(\omega_n t) \quad (26)$$

In equation (25),

$$\cos(kL)\cosh(kL) = -1 \tag{27}$$

$$k_{n=1,2,3\ldots}L = 1.87, 4.69, 7.85 \ldots \tag{28}$$

In equation (26),

$$\omega_n = k_n^2\sqrt{\frac{EI}{\rho A}} \tag{29}$$

$$A_n = \frac{2}{L}\int_0^L \phi(x)X_n(x)dx \tag{30}$$

$$\phi(x) = -\frac{PL^3}{6EI}\left\{3\left(\frac{x}{L}\right)^2 - \left(\frac{x}{L}\right)^3\right\} \tag{31}$$

Here x indicates the distance from the fixed end of the beam, P is the load applied to the tip of the beam to bend it, ρ is the beam density, E is the beam elastic modulus, L is the beam length, w is the width of the beam cross section, h is the height of the beam cross section, A is the beam cross-sectional area defined as w.h, I is the second moment of area defined as $wh^3/12$.

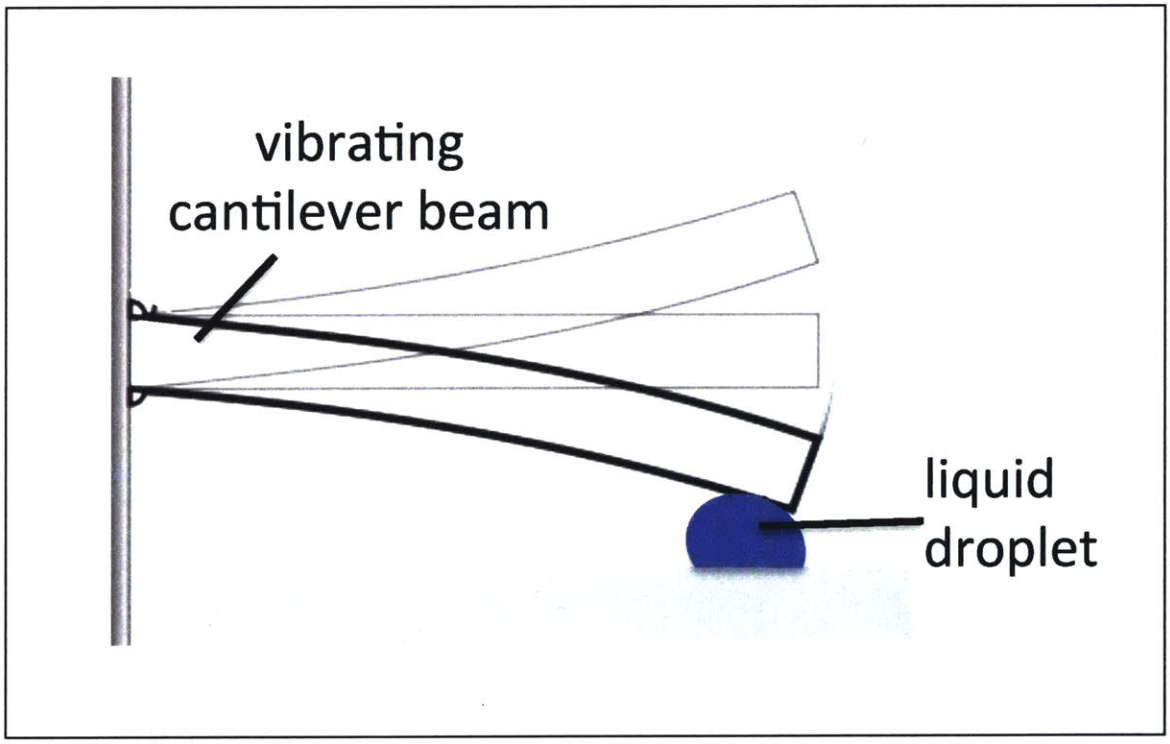

Figure D.2 Schematic of a vibrating cantilever beam that can be used to study splitting liquid bridges.

The displacement, velocity and acceleration of the tip of the beam can be calculated using the following equations.

$$q_{tip}(L,t) = \sum_{n=1}^{\infty} X_n(L)\, A_n cos(\omega_n t) \quad (32)$$

$$v_{tip}(L,t) = \sum_{n=1}^{\infty} -X_n(L)\, A_n \omega_n sin(\omega_n t) \quad (33)$$

$$a_{tip}(L,t) = \sum_{n=1}^{\infty} -X_n(L)\, A_n \omega_n^2 cos(\omega_n t) \quad (34)$$

References

[1] European Comission, "Final vision document in roll-to-roll printed electronics manufacturing equipment, production lines and systems", Deliverable Report.

E. Experiments on Splitting Liquid Bridges

E.1. Measurement of the Volume and Contact Angle of Sessile Liquid Drops

A drop with dimensions smaller than the capillary length ($l_{cap} = \sqrt{\gamma/\rho g}$) has a shape resembling that of a spherical cap. Capillary length for water is 2.67 mm. For a spherical cap,

$$V_{cap} = \frac{\pi}{6} h(3R_{base}^2 + h^2) \quad (1)$$

$$\tan(\theta/2) = \frac{h}{R_{base}} \quad (2)$$

Experiments are performed to measure the volume and contact angle of sessile liquid drops. ln the experiments, dyed liquid drops (2 vol.% black McCormick food dye in water) having 1.5µlt, 1µlt and 0.5µlt volumes are placed on PMMA-coated substrates (6 vol.% solution of 495k MW PMMA in anisole is spin coated on a glass slide at 2500 rpm and baked on a hot plate at 190°C for 5 min) using a micropipette. Images of the drops are captured using a Celestron handheld digital microscope. The captured images have around 50 pixels/mm. Next, the base radius and the height of the droplets are measured, and using equations (1) and (2), their volume and contact angle are calculated.

	Measured			Calculated	
Drop	Volume	Diameter	Height	Angle	Volume
1	1.5 µlt	2.116mm	0.730mm	69°	1.49 µlt
2	1.5 µlt	2.155mm	0.709mm	66°	1.48 µlt
3	1 µlt	1.888mm	0.609mm	66°	0.97 µlt
4	1 µlt	1.862mm	0.635mm	68°	0.99 µlt
5	0.5 µlt	1.429mm	0.505mm	70°	0.47 µlt
6	0.5 µlt	1.505mm	0.485mm	65°	0.49 µlt

Table E.1 Results of experiments. Contact angle and volume of dyed water drops are calculated from measured diameter and height using equations (1) and (2).

Results of experiments are summarized in Table E.1. Calculated volumes differ by less than 10% from the actual drop volumes. Since dimensions of the drops are smaller than the capillary length, spherical cap approximation is valid. Contact angles of the water drops measured using DropSnake plug-in of ImageJ software are 4° to 8° smaller than the contact angles calculated using equation (7). [1] indicates variability in contact angles measured using DropSnake plug-in depending on the measurement parameters used, and a difference in results compared to those obtained using other software for certain measurements.

E.2. Liquid Splitting Between a Roller and an Inclined Slide

Splitting of liquid bridges is studied experimentally using a rolling cylinder. In the experiments, a cylinder placed on a drop resting on an inclined glass slide is allowed to roll under the action of gravity (Figure E.1). During this process, the liquid drop splits and part of it is transferred to the cylinder surface. Fraction of liquid transferred to the cylinder surface is calculated from the captured image of the drop on the cylinder.

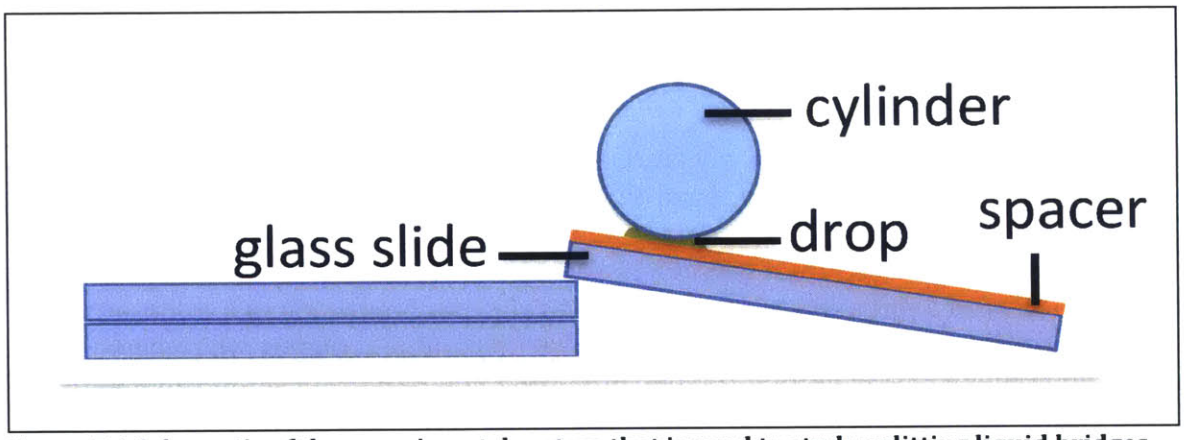

Figure E.1 Schematic of the experimental system that is used to study splitting liquid bridges.

The surface of the glass slide is coated with PMMA, and the surface of the cylinder is covered with a silicone rubber sheet having an adhesive back. Two layers of tape are used as the spacer between the cylinder and the glass slide. Volume and contact angle of the drops are calculated using spherical cap approximation, since drop dimensions are smaller than the capillary length in the experiments. Experiment details are summarized in Table E.2.

Liquid	2 vol.% black McCormick food dye in distilled water
θ_{liq} on PMMA-coated slide	65° - 70°
θ_{liq} on silicone rubber sheet	100°-110°
Initial drop volume	1.5µlt
Inclination angle of slide	1.5°
Radius of cylinder	2 cm
Spacer height	0.54 mm

Table E.2 Details of the liquid splitting experiments. Contact angle measurements are done using 1.5µlt drops.

Results of the experiments are summarized in Table E.3. The fraction of liquid transferred to the cylinder surface is less than 5%. Because the slide surface is more wettable than the cylinder surface, this result is as expected. Since the drop transferred to the cylinder surface is smaller and hence evaporates slower, fraction of liquid transferred to the cylinder is calculated by dividing the volume of the drop on the cylinder by 1.5µlt. Images of the drops captured before and after splitting are shown in Figure E.2 for a sample experiment.

Experiment no	Transfer ratio
Experiment 1	3%
Experiment 2	1%
Experiment 3	1%
Experiment 4	<1%

Table E.3 Results of liquid splitting experiments. Transfer ratio is calculated by dividing the volume of the liquid drop on the cylinder surface by 1.5 µlt. Results of the 4 experiments that yield the smallest transfer ratio values are reported.

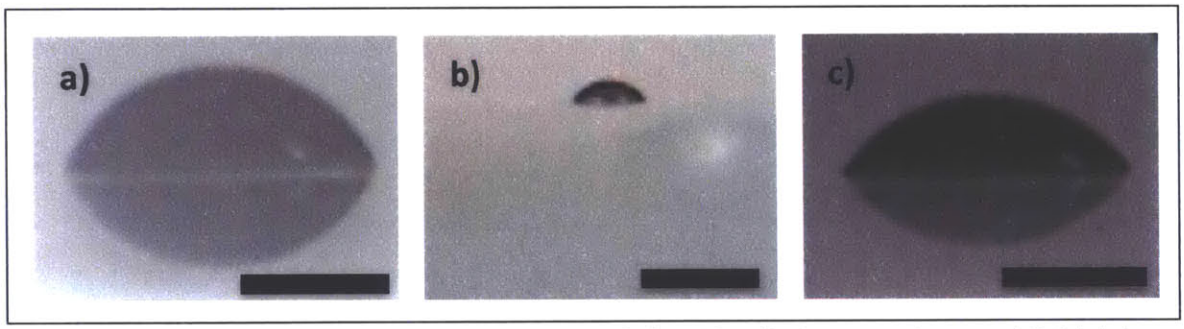

Figure E.2 Images of the drops captured in a sample liquid splitting experiment. a) Initial drop with 1.5µlt volume on the PMMA-coated glass slide. b) Drop transferred to the cylinder surface having 0.04µlt volume (about 3% of the drop is transferred to the cylinder surface). c) Drop remaining on the PMMA-coated glass slide after splitting with 1.1µlt volume (about 25% volume reduction). Length of the scale bar is 1 mm. Images a) and c) have around 45 pixels/mm and image b) has around 37 pixels/mm.

E.3. Liquid Splitting Between Manually Separated Slides

Splitting liquid bridges are investigated experimentally by splitting a liquid drop trapped between two slides manually and recording the splitting process with a camera. Experiment results are shown in Figure E.3. The liquid drop is observed to form a neck that gets thinner as it stretches in the experiments.

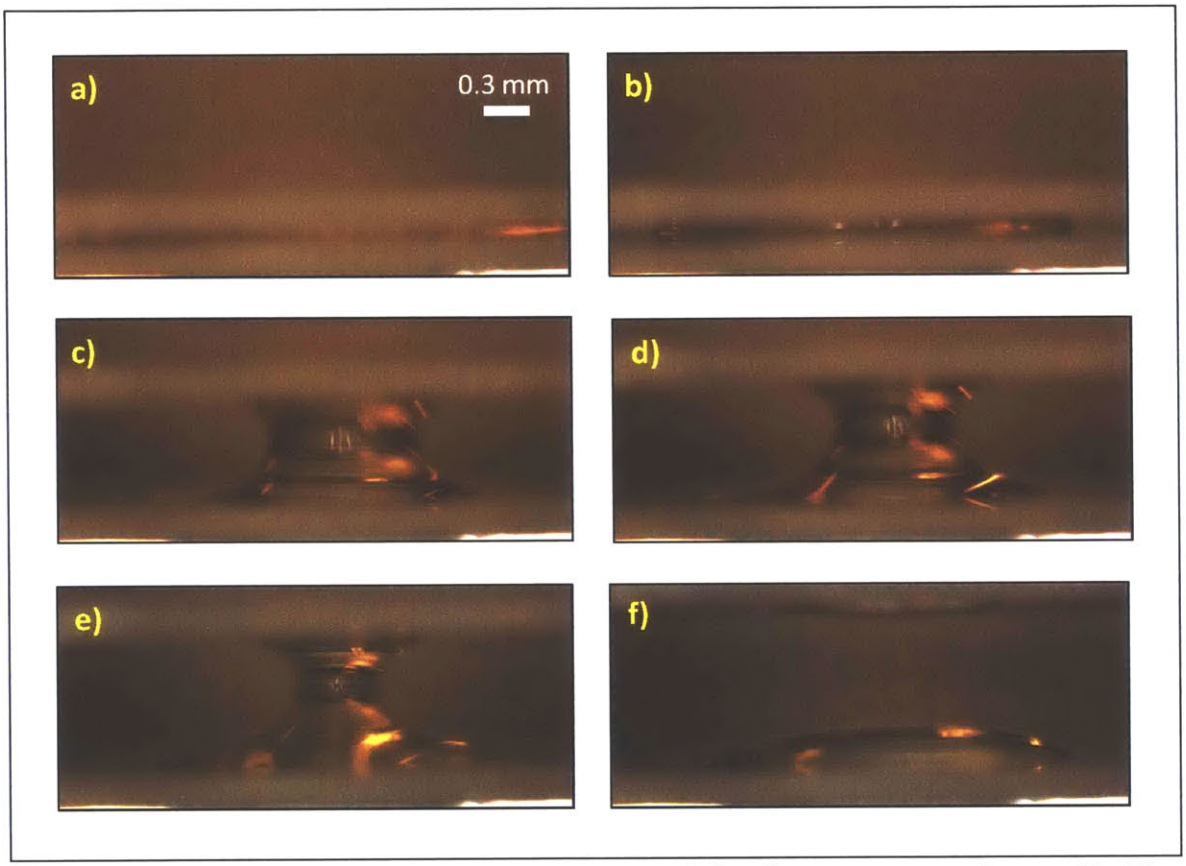

Figure E.3 The splitting of a liquid drop between two slides that are separated manually. The lower slide is stationary and the upper slide moves. a) The liquid drop is trapped between two slides that are separated by 0.4 mm using spacers attached to the lower slide. b) The upper slide is lifted slightly upwards to overcome the adhesive force the liquid applies to keep the two slides attached. In this frame, t=0 sec. c) The liquid stretches, as the upper plate moves. In this frame, t=0.490 sec. d) The liquid continues stretching. In this frame, t=0.531 sec. e) The liquid stretches further. In this frame, t=0.572 sec. f) The liquid splits forming two drops that are attached to the upper and lower slides. In this frame, t=0.735 sec. In the experiment, velocity of the upper slide is about 0.5 mm/sec and the volume of the liquid is 100 μLt. A sessile liquid drop makes a contact angle of about 44° with the slide surface.

References

[1] A. F. Stalder *et. al.*, "A snake-based approach to accurate determination of both contact points and contact angles", Colloids and Surfaces A, 2006.

F. Roller Blading

In this section, the elastohydrodynamic interaction of an elastic blade with a smooth roller, and the elastohydrodynamic interaction of an elastic blade with an engraved roller are explained.

F.1. Interaction of an Elastic Blade With a Smooth Roller Surface

Flexible-blade coating is an example of a coating process that involves the interaction of an elastic blade with a smooth roller [1]. In this coating process, a liquid film of controlled thickness is metered onto a moving, roller-supported substrate by means of a blade that is loaded against an over-supply of liquid applied upstream (Figure F.1a). The blade can be externally loaded in different ways, for instance, by clamping it to a working angle that is larger than its initial installation angle causing the blade to deform or by using an air bladder, a hose or a bar positioned against the blade to load and bend it as shown in Figure F.1b.

Typically the blade's upstream edge is clamped into a rigid holder so that the blade and the substrate form a converging wedge, where the liquid forces develop and deflect the elastic blade (Figure F.1). When the liquid is dragged towards the vertex of this wedge by the moving substrate, the hydrodynamic pressure rises and causes an adverse pressure gradient. This induces a pressure-driven flow component, which opposes the viscous-drag-driven flow component caused by the moving substrate. As a result of this opposing pressure-driven flow, most of the incoming fluid is rejected and only a fraction of it passes through the gap between the blade and substrate forming a coated layer.

An additional role of the hydrodynamic pressure in the coating process is to load and deform the blade elastically together with the viscous shear stresses acting on the blade. Elastic restoring forces within the blade that are induced by its elastic deformation, and the externally applied load on the blade balance the hydrodynamic pressure and viscous shear stresses.

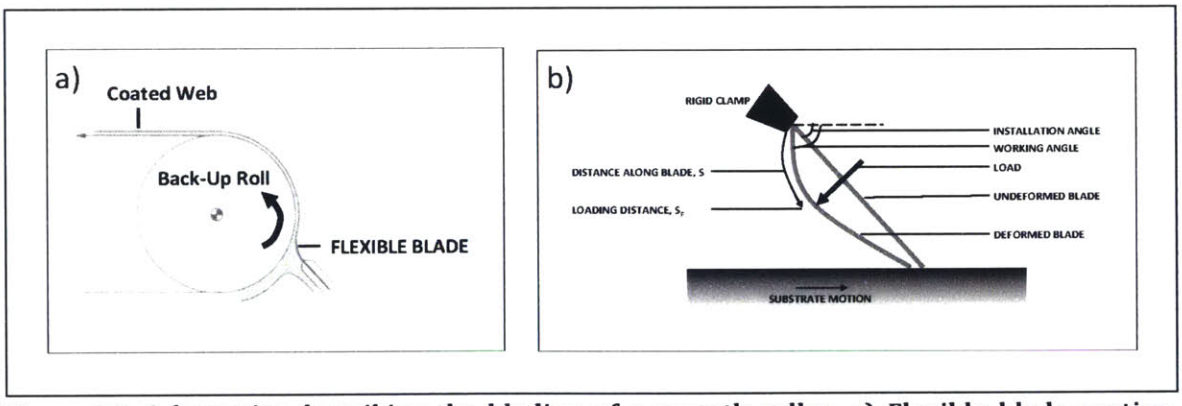

Figure F.1 Schematics describing the blading of a smooth roller. a) Flexible blade coating (adapted from [1]). b) A loaded blade on a smooth surface (adapted from [2]).

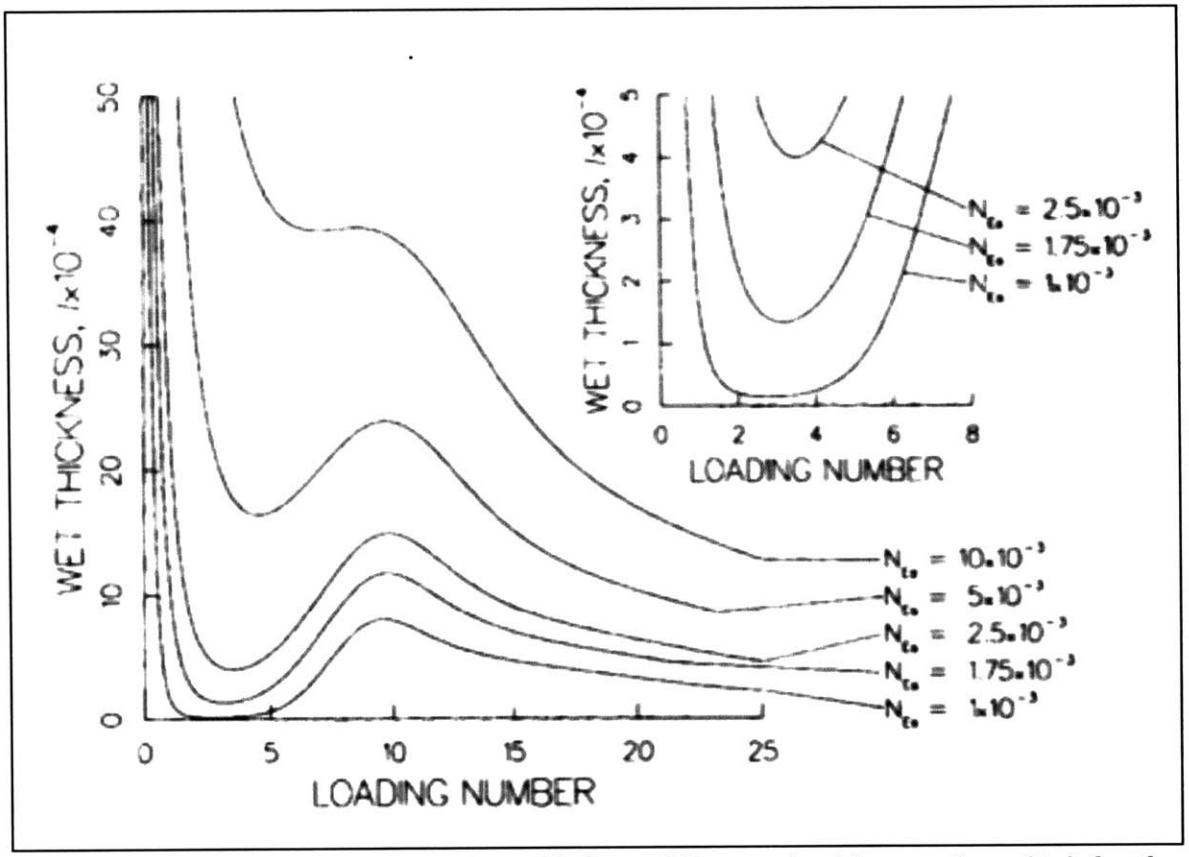

Figure F.2 Operating curves of an elastic blade at different elasticity numbers (N_{es}) for the doctoring of a smooth roller. The process parameters used to obtain the operating curves are described in [2]. The figure is taken from [2].

F.1.1. Operating Curve of an Elastic Blade for Doctoring of a Smooth Roller

The operating curve of a doctor blade shows the variation of the metered film thickness remaining on the roller with loading number (or working angle) and the elasticity number [2] (Figure F.2). It can be obtained from the solution of the equations that govern the lubrication-type flow in the passage formed by the blade and the substrate together with the equations that govern the elastic response of the blade under loading. The loading number and the elasticity number are defined as $F_N.L^2/D$ and $\mu.U.L^2/D$, respectively. Here, μ is the liquid viscosity, U is the substrate speed, L is the blade length, D is the blade bending stiffness and F_N is the normal loading force that is externally applied on the blade with a sharp-edged bar.

The operating curve indicates that with increasing loading number, the metered coating thickness on the smooth roller first falls abruptly to a minimum, rises again, reaches a maximum and then falls moderately. The lower the elasticity number (smaller viscous forces, higher blade stiffness, lower substrate speeds and shorter blades), the thinner is the coating and the more pronounced the extrema in the operating curves at any loading number. The effect of increasing the working angle on the operating curve is similar to the effect of increasing the loading number. The changes in metered film thickness with the variations in the coating parameters can

be explained based on the changes in blade behavior and the balance of the forces that influence the coating process.

F.2. Interaction of an Elastic Blade With an Engraved Roller Surface

In this section, the blading of a trihelical engraved roller is described based on the study by Kistler [3]. In this work, the grooves having different depths are represented by their internal tooth angle (groove depth decreases with increasing internal tooth angle). A stiffness parameter defined as $E.t^3/[12.(1-v^2).\mu.U.L^2]$ is used for expressing the results, where E is the blade elasticity, t is the blade thickness and v is the Poisson's ratio for the blade material. The deep-groove regime and the shallow-groove regime are identified as the two regimes that describe the blading process (Figure F.3a).

In the shallow groove regime of operation, the engraved roller has shallow grooves (high internal tooth angle) and/or the blade is highly-flexible (low stiffness parameter). This leads to a large clearance between the blade and the land area (area between two grooves on the roller surface) (Figure F.3a, Figure F.4a). Hence a significant amount of coating is left on the land area. The response of the system in terms of its operating curve is similar to that of a smooth roller (Figure F.3b).

In the deep groove regime of operation, the engraved roller has deep grooves (low internal tooth angle) and/or the blade is stiff (high stiffness parameter). This leads to a very small clearance between the blade and the land area (Figure F.3a, Figure F.4b). Hence, the flow is metered almost completely by the cell volume. The response of the system, in terms of its operating curve, is different than that of a smooth roller with the average film thickness metered by the blade no longer passing through a minimum and a maximum (Figure F.3b). As the blade tip moves closer the land surface, the average film thickness metered by the blade becomes less sensitive to the load and gets almost equal to cell volume per unit area. Toward higher loads, the cells are left partially filled.

Additional simulation results presented by Brethour indicate that air bubbles may be trapped in the grooves during their filling and blading [4]. For larger contact angles on the groove surfaces, the volume of the air trapped in the grooves is found to be larger.

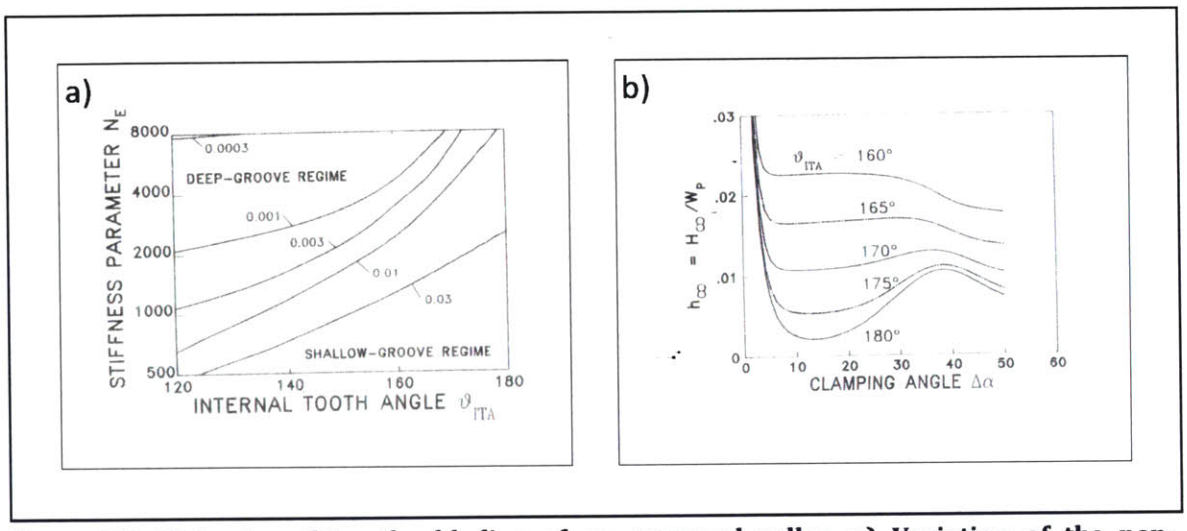

Figure F.3 Plots describing the blading of an engraved roller. a) Variation of the non-dimensional closest blade to land spacing (indicated by the values on the contours) with stiffness parameter and internal tooth angle. Deep-groove and shallow-groove regimes are indicated on the plot. b) Variation of the non-dimensional average film thickness metered by the blade (h_∞) with the clamping angle and the internal tooth angle (indicated by the values on the contours). The process parameters used to obtain the plots are described in [3]. The plots are taken from [3].

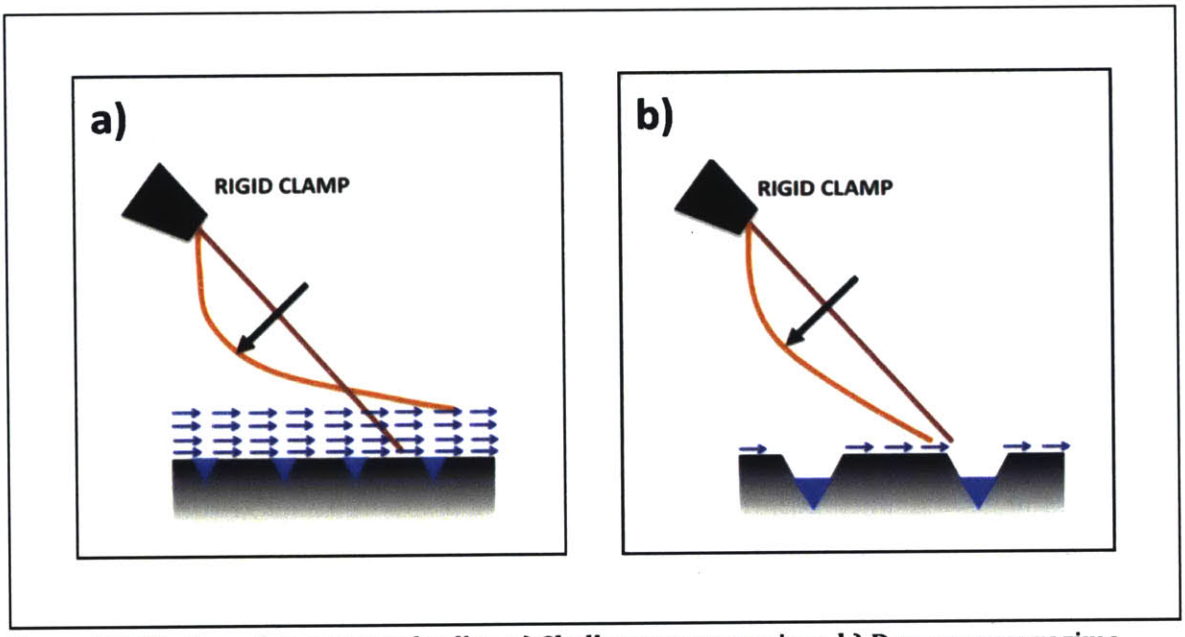

Figure F.4 Blading of an engraved roller. a) Shallow groove regime. b) Deep groove regime.

References

[1] F. R. Pranckh and D. J. Coyle, "Elastohydrodynamic Coating Systems", inside: Liquid Film Coating. Scientific Principles and Their Technological Implications. Springer, 1997.
[2] F. R. Pranckh and L. E. Scriven, "Elastohydrodynamics of Blade Coating", American Institute of Chemical Engineers Journal, 1990.
[3] S.F. Kistler, "Flexible Blade Doctoring in Gravure Coating", AIChE Meeting Paper, 1988.
[4] J. M. Brethour, "Filling and emptying of gravure cells – a CFD analysis", Contribution, Flow Science Inc.

G. Splitting of Liquid Films Between Roller Surfaces

In this section, the splitting of liquid films between roller surfaces is described. The splitting of a liquid film between a metering roll and an applicator roll in a reverse roll coater is the example of a liquid splitting process between two smooth roller surfaces (Figure G.1a). This process is described in Section G.1. The splitting of a liquid film between an engraved roll and a web (Figure G.1b) is described in Section G.2.

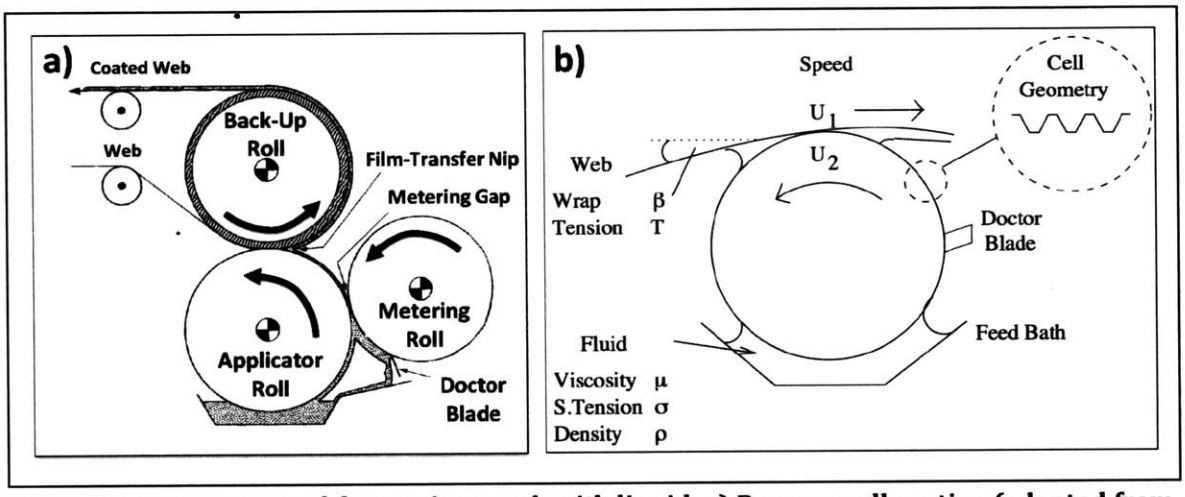

Figure G.1 Processes used for coating a web with liquid. a) Reverse roll coating (adapted from [1]). b) Gravure printing (adapted from [3]).

G.1. Splitting of a Liquid Film Between Two Smooth Roller Surfaces During Reverse Roll Coating

In a reverse roll coater, a thick liquid film is applied to a rigid applicator roll by dipping it in a liquid bath. Then, part of this liquid film is transferred to a rigid metering roll whose surface moves in the opposite direction as the applicator roll, in a region called the metering gap. The liquid within the metering gap is called the coating bead. Next, the metered liquid film on the applicator roll is transferred to the web (the substrate to be coated), which is squeezed between the applicator roll and the back-up roll (Figure G.1a and Figure G.2). The results of Coyle *et. al.* [1] on the splitting of a liquid film between the metering roll and the applicator roll in a reverse roll coater are summarized below.

- On the upstream side of the liquid bead, where the liquid film is transferred from the applicator roll to the metering roll, there is a large recirculation zone. Near the dynamic wetting line on the downstream side of the bead, a smaller recirculation region may exist (Figure G.2).

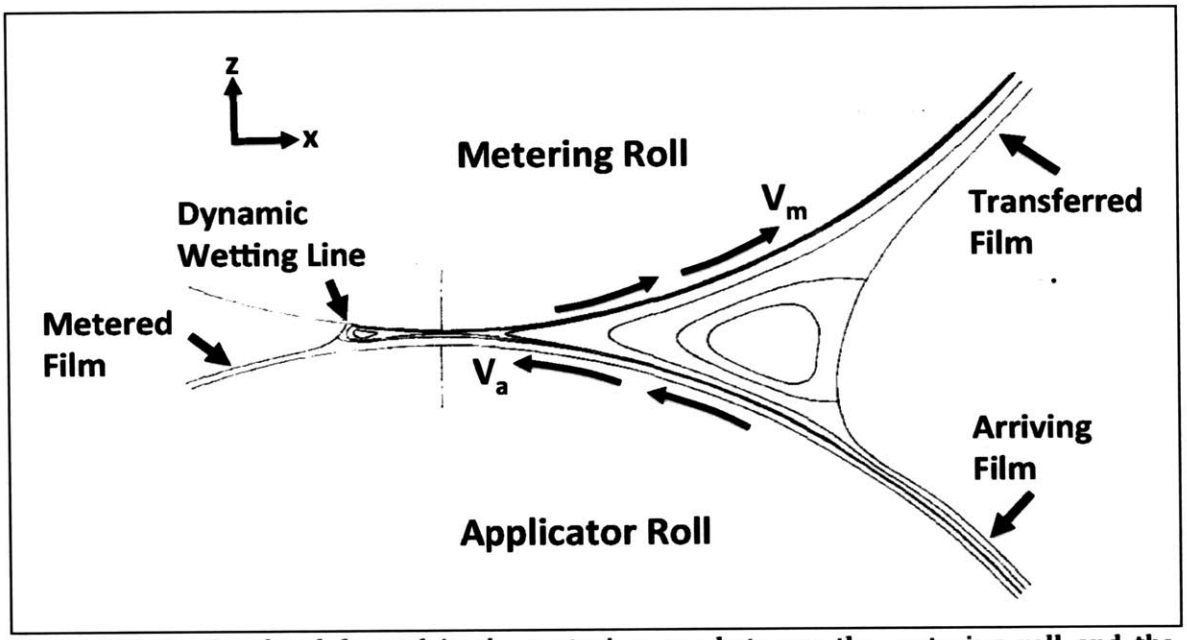

Figure G.2 Coating bead formed in the metering gap between the metering roll and the applicator roll (adapted from [1]).

- Increasing the speed ratio ($V_{metering}/V_{applicator}$) causes the dynamic wetting line to move towards the upstream side of the coating bead, shrinks the recirculations on the upstream side, and makes the coating bead smaller and tightly-curved (Figure G.3a).
- Increasing the capillary number has the same effect on the coating bead as increasing the speed ratio. In addition, increasing the capillary number causes the recirculations inside the coating bead to disappear (Figure G.3b).

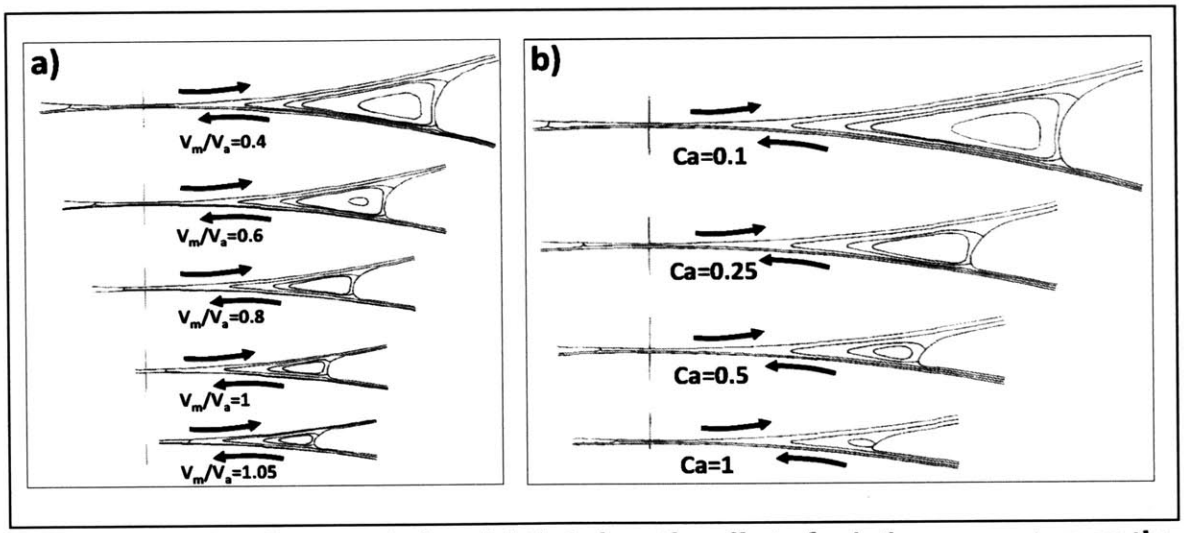

Figure G.3 Results of a numerical model that show the effect of printing parameters on the coating bead. a) Change in coating bead with speed ratio ($V_{metering}/V_{applicator}$). b) Change in coating bead with capillary number (adapted from [1]). Gravity is not considered in this model.

- Variation of the non-dimensional metered film thickness on the applicator roll (t) with the speed ratio and the capillary number is shown in Figure G.4. The non-dimensional metered film thickness decreases, goes through a minimum and then increases with increasing speed ratio. At higher Ca, the minimum appears at lower speed ratio and the variation in the film thickness is sharper. The metered film thickness remains close to the value predicted by a lubrication model at small speed ratios.

The thickness of the film transferred from the applicator roll to the web is found to be directly proportional to $[T\beta]^{-1}$, where T is the web tension and β is the wrap angle [1].

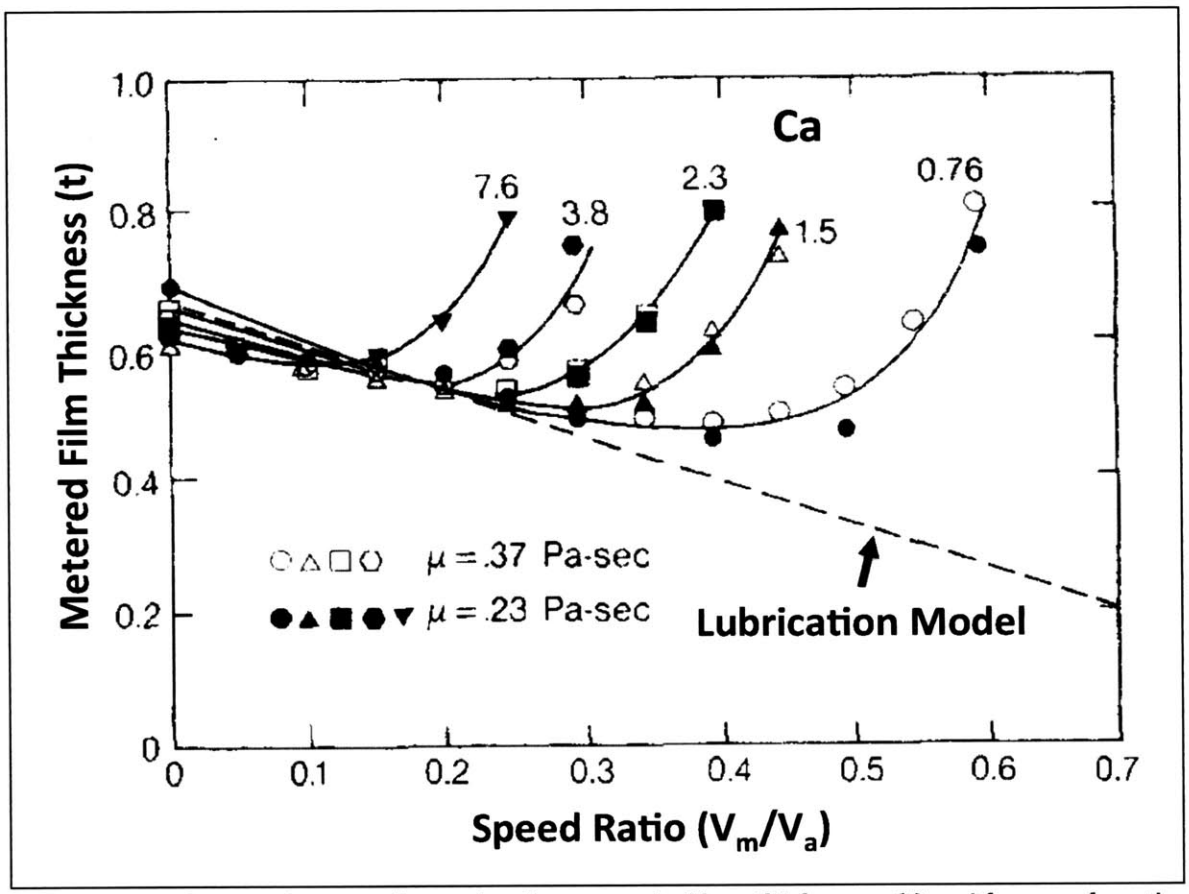

Figure G.4 Change in non-dimensional metered film thickness (t) with speed ratio ($V_{metering}/V_{applicator}$) and capillary number (adapted from [1]).

G.2. Splitting of a Liquid Film Between an Engraved Roller and a Substrate During Gravure Printing

The experimental work on liquid film transfer from an engraved roller to a substrate (Figure G.1b) presented in [3-5] is summarized below. The gravure printer examined is operated in reverse mode (the substrate and the engraved roller move in opposite directions) in [3, 5], and in forward mode (the substrate and the engraved roller move in the same direction) in [4].

The thickness of the liquid film transferred to the substrate (h_T) can be expressed as a function of the printing conditions, as shown in Equation (1).

$$h_T = f\left[U_r, U_s, \mu_{ink}, \sigma, \rho_{ink}, h_0, \theta_s, \frac{V_c}{A_c}, R, g\right] \quad (1)$$

Here, U_r is the roller velocity, U_s is the substrate velocity, μ_{ink} is the liquid viscosity, σ is surface tension coefficient of the liquid, ρ_{ink} is the liquid density, h_0 is the slot gap, θ_s is the substrate wrap angle, V_c is the volume of the cells per unit area of the roller, A_c is the area of cell opening per unit area of the roller, V_c/A_c represents the average depth of a cell, R is the roller radius and g is the gravitational acceleration. For a fixed roller radius, with the initial crude assumption of negligible surface tension and gravity effects, a reduced form of equation (1) can be written in terms of dimensionless parameters, as shown in Equation (2).

$$h_T \frac{A_c}{V_c} = f\left[\frac{\rho U_s}{\mu}\frac{V_c}{A_c}, \frac{U_s}{U_r}, h_0 \frac{A_c}{V_c}, \theta_s\right] \quad (2)$$

Here, $h_T \frac{A_c}{V_c}$ is the dimensionless film thickness transferred to the substrate (h), $\frac{\rho U_s}{\mu}\frac{V_c}{A_c}$ is the Reynolds number (Re), $h_0 \frac{A_c}{V_c}$ is the dimensionless slot gap and $\frac{U_s}{U_r}$ is the substrate to roller speed ratio (S). Assuming that blade functions as to remove all the excess liquid over the cells, the $h_0 \frac{A_c}{V_c}$ term can be removed from equation (2). Since experiment results indicate that the changes in wrap angle lead to insignificant changes in transferred film thickness [3, 5], the mechanism of film transfer can be assumed to be controlled by the drag of liquid from a small liquid pool, which is formed at the contact point of the web and the roll. Hence, the θ_s term can also be removed from equation (2) leading to:

$$h = h_T \frac{A_c}{V_c} = f\left[Re = \frac{\rho U_s}{\mu}\frac{V_c}{A_c}, S = \frac{U_s}{U_r}\right] \quad (3)$$

The dependence of the non-dimensional film thickness on the Reynolds number and the speed ratio, as indicated in equation (3), as well as on the cell geometry and the liquid properties is reported to be as follows.

- Benkreira and Patel [5] report that the dimensionless film thickness transferred the substrate increases with Re for Re<30, mildly decreases up to Re=75 and then reaches a constant value of 0.3 at higher Re for various printing conditions at a speed ratio of 1. The same variation is observed, as the speed ratio changes between 0.5 and 2 with the limiting Re values shifted. This means that only 30% of the descriptive cell size (V_c/A_c) is transferred as a film at high Re independent of the printing parameters. The fraction of cell volume emptied can reach values as high as 50%, as the speed ratio increases. In contrast to these observations, Kapur [3] reports that there is no clear relation between the non-dimensional film thickness and Re.
- Pulkrabek and Munter [4] indicate that pickout (Φ), defined $\Phi=(h_T/V_c)S$, remains constant at 0.59 under a range of coating conditions for a gravure printer operated in forward mode. This means that the film thickness transferred to the substrate will decrease with increasing speed ratio. In contrast, Kapur [3] observes that the film thickness transferred to the substrate increases with increasing speed ratio for a gravure printer operated in reverse mode. Specifically, Kapur finds that the film thickness transferred to the substrate increases linearly with speed ratio for speed ratio between 0 and ~1.5. At higher speed ratios, the film thickness becomes constant.
- Kapur [3] reports that for different engraving geometries, the thickness of the liquid film transferred to the substrate increases with speed ratio. A larger V_c leads to a higher thickness of the transferred liquid film and a higher pickout. However, despite having a smaller (or the same) V_c, a cell with larger aspect ratio (width/depth) can result in a larger pickout. These contradict with the findings of Benkreira and Patel [5], which indicate that V_c does not affect pickout. Kapur [3] reports that cell geometries having smoother surface profiles show less resistance to ink flow and lead to higher pickout.
- Kapur [3] indicates that increasing liquid viscosity, increasing speed ratio and decreasing surface tension improves cavity emptying, but there is no correlation between capillary number and the experimental data obtained. This contradicts with the study by Yin and Kumar [2] which indicate that the function between the coating film thickness and the capillary number is of the form $a.Ca^b$.
- The transferred film thickness is found to be independent of the tension and wrap angle, in contrast to the smooth roll results.

As described in detail in [6], the liquid film splitting is affected by several parameters such as the period of the contact between the rollers (which is a function of printing speed and the geometry of the printing components), contact pressure, and temperature of the roller surfaces. Different tools for designing printing systems have been have been developed such as formulae for calculating the thickness of the ink layer transferred from one roller to the next, simulation programs that predict the ink distribution in the inking systems, and experimental setups equipped with ink layer thickness sensors for investigating the influence of printing parameters on the ink transfer.

References

[1] D. J. Coyle *et. al.*, "The fluid dynamics of reverse roll coating", AIChE Journal, 1990.
[2] X. Yin and S. Kumar, "Flow visualization of the liquid emptying process in scaled-up gravure grooves and cells", Chemical Engineering Science, 2006.
[3] N. Kapur, "A parametric study of direct gravure coating", Chemical Engineering Science, 2003.
[4] W. W. Pulkrabek and J. D. Munter, "Knurl roll design for stable rotogravure coating", Chemical Engineering Science, 1983.
[5] H. Benkreira and R. Patel, "Direct gravure roll coating", Chemical Engineering Science, 1993.
[6] H. Kippahan, "Handbook of printing media", Springer, 2001.

H. Hardware and Software

- Microfluidics module of COMSOL software (version 4.4) is used with a Named Single User License for the modeling of liquids splitting between separating surfaces. Software bugs detected in the software are reported to COMSOL and got fixed, which enabled obtaining accurate simulation results consistent with the literature.
- Structural mechanics module and nonlinear structural materials module of COMSOL software (version 4.4) are used with a Named Single User License for the modeling of stamp deformation.
- It is recommended to run the simulations on the computer with 192GB RAM and 14 cores in the Hardt Laboratory, which is purchased for running simulations.
- It is observed that the simulations do not run on the Amazon elastic compute cloud using the templates provided by COMSOL.
- Training offered by COMSOL can speed up the learning curve.